Università degli Studi di Ferrara

DOTTORATO DI RICERCA IN

FISICA

CICLO XXIX

COORDINATORE Prof. Vincenzo Guidi

Innovative PVD technologies for depositing superconducting Nb films into TESLA-type 9-cell RF cavities for particle accelerators

Settore Scientifico Disciplinare FIS/03

Dottorando
Dott. Giorgio Keppel

(firma)

Tutore
Prof. Vincenzo Palmieri

(firma)

Anni 2014/2016

Contents

Abstract

Superconducting radiofrequency resonators have become standard components inside particle accelerators. This paper proposes the research and development of copper cavities internally coated with a niobium thin film, as an alternative to the niobium bulk cavities.

This R&D work is part of the ISIDE experiment, of the National Institute of Nuclear Physics, and has been carried out at the Legnaro laboratories. Specifically, at the Material Science and Technologies for Nuclear Physics Service of INFN, it has been built a new system for coating, via magnetron sputtering, a thin film of superconducting niobium inside the TESLA-type 9-cell copper resonators.

The work was divided into two main areas.

A first phase consisted on the design of a sputtering configuration for coating superconductive cavities based on the construction of a vacuum system using a 3D CAD software and FEM simulations in order to verify the final structure of the vacuum system. Parallel to this a phase for the construction of the induction heating apparatus was followed. Afterward, the assembly of the vacuum system was performed, with connected vacuum tests, and followed by the commissioning of the induction and pumping systems.

A second phase, however, focused on the study of coating configurations, particularly on the benefits and/or problems that each configuration can lead. This study ended with the design of four different coating configurations; which will be short-tested in order to check the most suitable for coating the 9-cell copper cavity with good uniformity and excellent superconducting properties. The most promising configuration is definitely the last taken into account, which involves the use of the inductor to heat the cavity during the process and the use of an innovative cylindrical magnetron with a rotating magnet pack inside that confine the plasma on the target surface. The target consists on a Niobium tube, and the study of the magnetic configuration and at the same time rotation of magnet pack permit to have a constant deposition rate along the whole cavity (high cathode erosion rate in the cavity cell regions and low cathode erosion rate along cavity cut-off).

Even if the work is still evolving and the deposition tests are just starting, what as been performed is definitely innovative and original; up to now, in literature, there are no reports of coating performed by coupling the induction heating with the magnetron sputtering. The development of a plant that allows coupling these two technologies is the main aim of this work.

Estratto

Le cavità superconduttive in radiofrequenza sono diventate componenti standard all'interno degli acceleratori di particelle. Questo elaborato propone lo studio e lo sviluppo di cavità in rame ricoperte internamente di un sottile film di niobio come alternativa alle cavità in niobio bulk.

Questo lavoro di R&D si inserisce all'interno del progetto ISIDE, dell'Istituto Nazionale di Fisica Nucleare, ed è svolto presso il Laboratori Nazionali di Legnaro. Nello specifico, presso il Servizio Scienza e Tecnologia dei Materiali per la Fisica Nucleare degli LNL, si è lavorato per costruire un nuovo sistema per depositare, tramite magnetron sputtering, un film sottile di niobio superconduttore all'interno delle cavità TESLA type a 9 celle in rame.

Il lavoro è stato suddiviso in due filoni principali.

Una prima parte di progettazione del sistema da vuoto che si è avvalsa dell'utilizzo di software CAD 3D e si simulazioni FEM per verificare la struttura finale del sistema da vuoto. In parallelo a questa fase di progettazione si è seguita la costruzione presso la ditta incaricata dell'impianto di riscaldamento ad induzione. Si è provveduto in seguito all'assemblaggio del sistema da vuoto, con annessi test, ed a seguire il commissioning dell'impianto ad induzione e dei sistemi di pompaggio.

Una seconda parte del lavoro, invece, si è focalizzata sullo studio delle configurazioni di deposizione soffermandosi particolarmente sui benefici e/o problematiche che ogni configurazione può portare. Questo studio ha portato al design di quattro differenti sorgenti da sputtering che verranno testate a breve per verificare quale sia la più adatta per ricoprire tramite coating con buona uniformità e con ottime proprietà superconduttive le cavità 9 celle in rame. La configurazione più promettente è sicuramente l'ultima analizzata che prevede l'utilizzo dell'induttore per riscaldare la cavità durante il processo e l'utilizzo di un innovativo magnetron cilindrico che ha al suo interno un *magnet pack* rotante che permette il confinamento del plasma sulla superficie del target. Il target consiste in un tubo in Niobio e lo studio del confinamento magnetico e allo stesso tempo la rotazione dei magneti permette di ottenere una velocità di deposizione costante lungo

tutta la cavità (velocità di erosione del catodo maggiori nella regione della cella della cavità velocità di erosione minori in concomitanza dei cut-off della cavità).

Anche se il lavoro è ancora in evoluzione ed i test di deposizione stanno iniziando in questo momento, il lavoro eseguito è sicuramente originale ed innovativo in quanto ad ora in letteratura non esistono riscontri di deposizioni eseguite accoppiando il riscaldamento ad induzione con il magnetron sputtering. Lo sviluppo di un impianto che permette di accoppiare queste due tecnologie è stato il principale scopo di questo lavoro.

List of Tables

List of Figures

Acronyms

The following is a list of the acronyms used in this thesis:

- AC = Alternating Current
- DC = Direct Current
- FEM = Finite Element Method
- LINAC = LINear Accelerator
- PFC = Polycold Fast Cycle
- PVC = PolyVinyl Chloride
- PVD = Physical Vapour Deposition
- QWR = Quart Wave Resonator
- RF = Radio Frequency
- RRR = Residual Resistivity Radio
- SC = Superconducting
- SEM = Scanning Electron Microscope
- SRF = Superconducting Radio Frequency
- SS = Stainless Steel
- UHV = Ultra High Vacuum

Chapter 1

Introduction

1.1 Scientific context and thesis purpose

New particle accelerators require new technology. The superconducting radio frequency cavities are the fundamental parts of the accelerator structure and a less than revolutionary ideas on Particle Acceleration physics, each new development of future accelerators facilities deal with innovation on superconducting cavity technology.

In the last 20 years, National Institute of Nuclear Physics (INFN), has been mainly working to the R&D on alternative manufacturing techniques for superconducting cavities. Now, if we analyse a standard TESLA-type elliptical 9-cell accelerating cavity, since each resonator weight is around 25 kg (without calculating the scrap material) and niobium has a cost of about 600 €/kg, it is easy to understand that, we need to develop a new manufacturing technology, othervise the Large Hadron Collider at CERN will be the last of the large accelerators. In detail, a bulk Niobium 9 cell cavity costs approximatively 90 k€, considering material, machining and chemical process, for a total of 1.44 G€. However, if we consider the same cavity but produced in OFHC copper with Niobium thin coating, an excess estimation of cost is 15 k€, approximatively a sixth of bulk Niobium cavity, for a total of 0.24 G€. It is easy to understand that if accelerator community want to build a facility like ILC, that has approximatively 16000 9-cell cavities, the use of thin film technology may allow a saving of 1.2 G€.

The R&D on coating technology applied to superconductive accelerating cavity is fundamental. We need a new low-cost manufacturing technology, with high reproducibility, and an easy transferability to industry. Indeed, this technology already exists: it was developed at CERN in the 80s for the production of the LEP accelerating cavities for electrons. 10 years later, at LNL INFN, this technique was validated and applied for the production of the cavities used on the heavy ions ALPI accelerator. It deals with niobium thin film onto copper deposited by sputtering. In fact, since the electromagnetic fields, confined into the cavity, dissipate within the first few hundred nanometres of the resonator cavity wall, it is sufficient to deposit a thin film of about 1-2 microns of niobium to have factors of merit Q of the order of 10^{10}. Thanks to the use of copper as the substrate for the niobium film, the superconducting thin film cavities, respect to bulk Niobium resonators, are:

- Infinitely cheaper,
- Much more thermally stable because of the high conductivity of copper,
- Much more mechanically stable thanks to high copper thickness that suppress the microphone vibration motions.

The purpose of this research is to develop, design, build and test an innovative deposition process in order to be able to deposit thin films of niobium onto copper accelerating cavities.

In order to achieve a goal with this research line the following systems were developed:

- The design and construction of a vacuum plant;
- The design and construction of an innovative source for magnetron sputtering that allows to coat an elliptical 9-cell cavities;
- The installation of a system for induction heating able to heat the 9-cell cavity in UHV conditions and able to sustain plasma at the same time.

To achieve these objectives, I made use of 3D software design, FEM simulation for both the mechanical, magnetic and electromagnetic. Steps were taken to commissioning and installing new plants and depositing the first thin film and measurements of the same.

If this work will succeed in demonstrating that sputtering technologies can be suitable for the mass production of SRF cavities, new accelerators nowadays too expensive will be possible.

Chapter 2

Particle Accelerators and Facilities

2.1 Particle accelerators

Accelerators were invented in the 1930s to provide energetic particles to investigate the structure of the atomic nucleus. Since then, they have been used to investigate many aspects of particle physics. Their job is to speed up and increase the energy of a beam of particles by generating electric fields that accelerate the particles, and magnetic fields that steer and focus them.

An accelerator comes either in the form of a ring (a circular accelerator), where a beam of particles travels repeatedly round a loop, or in a straight line (a linear accelerator), where the particle beam travels from one end to the other.

A particle accelerator consists of many systems that make the acceleration possible: a particle source, a vacuum chamber, a focusing system and many others. The device that immediately provides the acceleration by imparting energy to the charged particles is usually a microwave resonant cavity. Normal and superconducting materials are used to fabricate accelerating cavities. As over the last two decades the science and technology of RF superconductivity has evolved and matured [1], more and more modern accelerators began using superconducting (SC) accelerating structures, which have several attractive features as compared to normal conducting cavities. The most salient of those features are high accelerating field, E_{acc}, in continuous wave (CW) and long pulse operating modes and high quality factor Q_0, a universal figure of merit characterizing the ratio of the energy stored in the cavity to the energy lost in one RF period.

Generally, in order to accelerate the protons, an electric field strips hydrogen nuclei of their electrons, then the electric fields switch from positive to negative at a specific frequency, pulling charged particles forwards along the accelerator. To ensure the particles in closely spaced bunches, the frequency is controlled.

Radio frequency (RF) cavities and magnets are needed for accelerating beams. The RF cavities are metallic chambers spaced at intervals along the accelerator; they are shaped in order to resonate at determined frequencies, allowing radio waves that can interact with passing particle bunches. Each time the beam passes, the electric field is transferred to the particles. It is important that the particles do not collide with the molecules of gases, because the beam is in UHV inside a metal pipe. In addition, various types of magnets are used into an accelerator. Dipole magnets are used to bend the path of a beam or to focus it. Around the collision point particle detectors are placed in order to reveal the particles [2].

In 1964 Fairbank, Schwettman and Wilson at Standford Linear Accelerator Center (SLAC), start the acceleration of electrons with superconducting RF structures. In this experiment 80 keV electrons were accelerated by a lead-plated onto a 3 cell of copper, reaching an energy of 500 keV. From this test it was demonstrated that a multicell accelerating structure could be operated at high accelerating gradients (3 MeV/m) and Q's of 10^8. From this experiment it was also demonstrated that were no big difficulties with the cryogenics [3].

Nowadays, a great number of accelerators has been used in order to reach higher energies; the type of particles depends of each experiment [2].

RF superconductivity is the technology for particle accelerator fastest growing.

Worldwide a large number of accelerator facilities have been built based on SRF structures (Superconductivity Radio Frequency). The applications of these accelerators deal with physical and industrial applications including particle physics, nuclear physics, synchrotron radiation and free electron lasers.

The progress of scientific research requires new accelerator facilities, able to create higher energy beams to be built.

The evolution of superconducting accelerating structures for the acceleration of particles with $\beta \approx 1$ (these are light particles, electrons and positrons, or high-energy protons; $\beta = v/c$, where v is the speed of the particle and c is the speed of light) led to cavities with an elliptical cell shape. The length of the cavity gap is usually

$$L = \beta \frac{\lambda}{2} \qquad (2\text{-}1)$$

λ being the wavelength, for the so called π mode in multicell cavities.

Heavier particles, e.g., ions or low energy protons, have low values of β. SC cavities for these particles are of different designs: split-ring resonators, half-wave-long and quarter wave long coaxial resonators, spoke cavities. The transition between low velocity cavity shapes and elliptical cavities usually occurs at $\beta = 0.6 \dots 0.8$. This is because cavities with elliptical cells for small β become very big as lower frequencies are used and less stable mechanically (the accelerating gap shortens and cavity walls become more vertical).

2.2 Accelerator facilities

Several facilities are using or are planning to use superconductive cavities in order to produce high-energy beams.

In the following paragraphs, the most relevant projects are summarised.

2.2.1 X-FEL, ILC, FCC and other Project with β≈1 cavities

2.2.1.1 X-FEL: X-ray Free Electron Laser

One of the facilities that currently uses the highest number of superconducting resonant cavities radio frequency is definitely the European X-ray Free Electron Laser (X-FEL). The European XFEL is a research facility (Figure 2.1) now under construction in the Hamburg area, Germany. From 2017, it will generate extremely intense X-ray flashes. To generate the X-ray flashes, bunches of electrons will first be accelerated to high energies and then directed through special arrangements of magnets called undulators. In the process, the particles will emit radiation that is increasingly amplified until an extremely short and intense X-ray flash is finally created. These X-ray flashes will enable a large variety of very different experiments like:

- Decipher the 3D structure of biomolecules, cell constituents and whole viruses.
- Investigate 3D nanostructure for future technology applications like storage device, computer chips, magnetic, optical and biological sensors, etc.
- Filming chemical reaction; the duration of the flashes is less than 0.1 trillionth of a second and thanks to the short wavelengths, even atomic details become visible.
- Study of exciting states of magnetization.
- Thanks to the high intensity of the flashes, the particles are excited into new, previously unknown states.

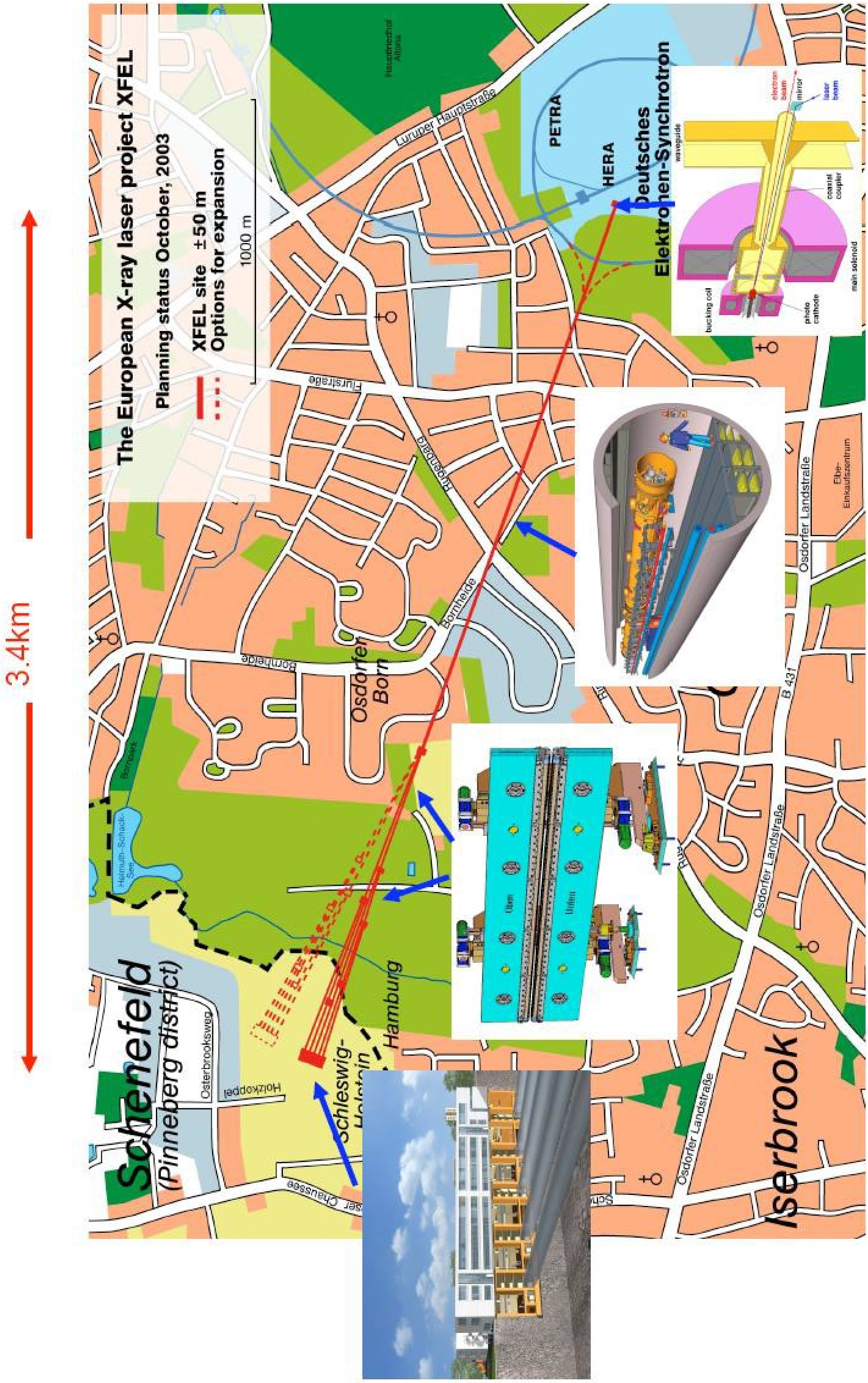

Figure 2.1: Sketch of the X-FEL site near DESY.

The first part of the facility is a 1.7-kilometre-long particle accelerator that brings bunches of electrons to high energies at nearly the speed of light. The heart of this accelerator is composed by an electron linear accelerator (linac) with a nominal design energy of 20 GeV, operating at an accelerating gradient of 23.6 MV/m and composed by 800, 9-cell, 1.3 GHz Niobium bulk accelerating cavities. It utilises the advanced superconducting radio frequency (RF) technology [4]: the acceleration of a large number of electron bunches per RF pulse (up to about 3000); small beam-induced wake fields and the possibility of applying intra-bunch train feedback to provide a stable and high quality beam; and a large operational flexibility regarding beam time structure and energy, including (as a possible future option) high duty cycle operation.

The XFEL is laid out as a multi-user facility. In its 1st stage, it will have 5 undulator beamlines, 3 of which are SASE-FELs [5] (two for the Å wavelength regime, one for softer X-rays), the other two for hard X-ray spontaneous radiation. Initially, 10 experimental stations are foreseen. The underground experimental hall has a floor space of 50×90 m^2 and more stations can be added later. The site allows to extend the user facility for more beam lines in a later stage [6].

The basic accelerator layout is sketched in Figure 2.2. The main linac uses 116-12m long accelerator modules with 8 superconducting cavities each, grouped in 29 RF stations. Twelve spare modules, i.e. three RF stations, are included in the design in order to guarantee the overall availability of the accelerator in case of failures [6].

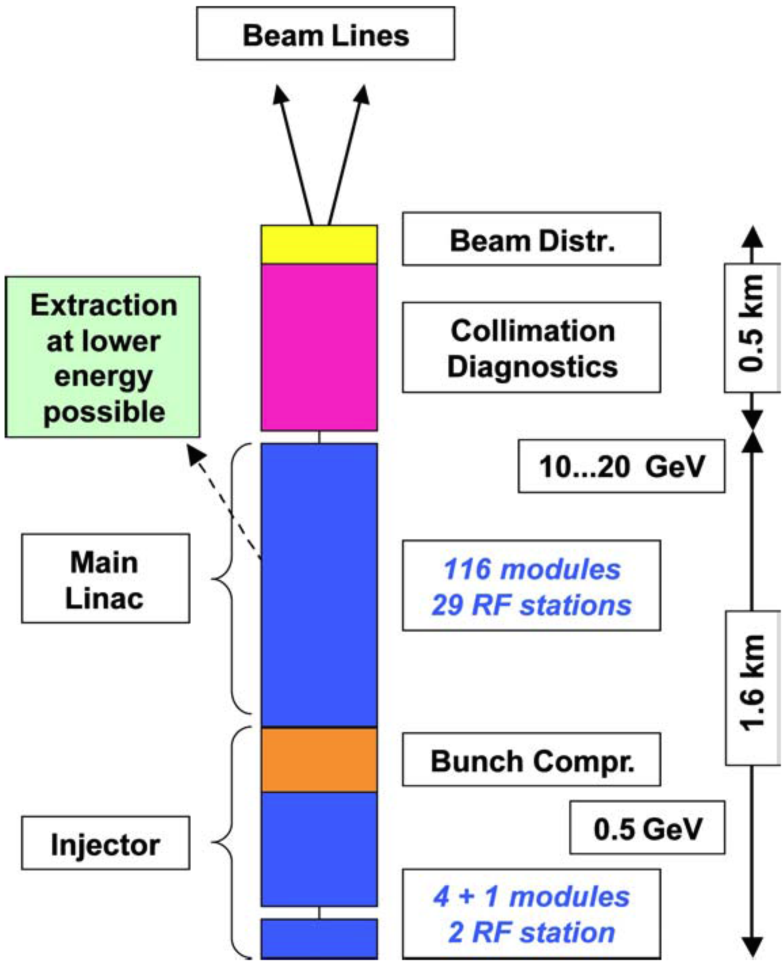

Figure 2.2: Basic layout of X-FEL accelerator [6].

2.2.1.2 ILC: International Linear Collider

Another important facility, at the moment under design, is the International Linear Collider (ILC). This facility is a 200-500 GeV centre-of-mass high-luminosity linear electron-positron collider, it consists in two linear accelerators that face each other, based on 1.3 GHz superconducting radio frequency accelerating technology (Figure 2.3). The use of the SRF technology was recommended by the International Technology Recommendation Panel (ITRP) in August 2004 [7]. Accelerator design involves the construction of two main linacs that will accelerate the electron and positron beams from their injected energy of 15 GeV to their final collision energy of between 100 GeV and 250 GeV, over a combined length of 22 km. The linacs utilise superconducting technology, consisting of approximately 16.000 1.3 GHz 9-cell niobium cavities operating at an average gradient of 31.5 MV/m in a 2K superfluid-helium bath, integrated into 1.700 12 m-long cryomodules [8].

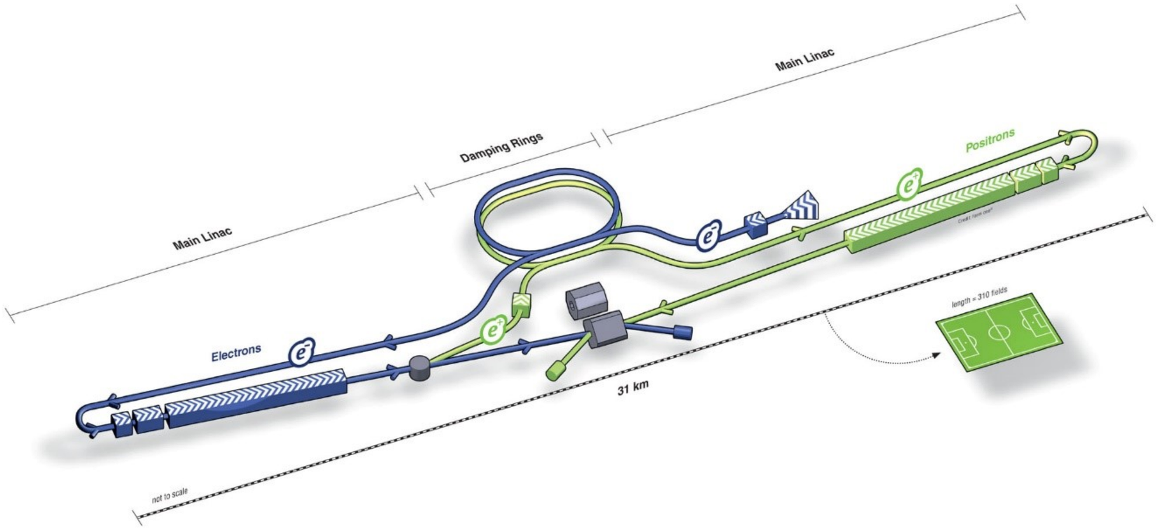

Figure 2.3: An overview graphic of the planned ILC based on the accelerator design of the Technical Design Report.

The TESLA elliptical cavity has been chosen for the ILC baseline design due to its maturity and the experience accumulated over the past decade and a half. In particular, approximately 800 TESLA cavities are already produced for the European XFEL. The ILC will give physicists a new cosmic doorway to explore energy regimes beyond the reach of today's accelerators. This electron-positron collider, the ILC, will complement the LHC (a proton-proton collider) that is now working at CERN.

2.2.1.3 FCC: Future Circular Collider

In parallel to this LINAC there is an intense R&D onto Future Circular Colliders (FCC) in order to explore different designs of circular colliders for the post-LHC era. The FCC study focuses on the design of a 100 TeV hadron collider (FCC-hh), to be accommodated in a new ∼100 km tunnel near Geneva. It also includes the design of a high-luminosity electron-positron collider (FCC-ee), which could be installed in the same tunnel as a potential intermediate step, and a lepton-hadron collider option (FCC-he) [9]. The Superconducting RF system of the FCC-ee shall serve for electron-positron collision at different beam energies ranging from 45.5 GeV to 175 GeV. Challenges for the SRF cavity design result from operating at four different voltages and currents. Using niobium coated cavities for FCC would allow an operation temperature of 4.5 K without losing thermal stability. Moreover, the requirement for relatively low RF frequency (400-800 MHz) will result in big accelerating structures with a cell diameter between 37.5 cm (800 MHz) and 75 cm (400 MHz). Building hundreds of structures of that size out of bulk niobium would result in excessive material cost. The niobium film technology comes with the benefit of saving a large amount of high purity raw niobium material. Nonetheless, the field limitation of the current Nb coatings make these cavities inefficient at fields required for FCC. Recent results on an energetically condensed Nb/Cu film, produced and tested in collaboration between Jefferson Lab and CERN, revealed a significantly better performance compared to the standard magnetron sputtering. Several laboratories worldwide have also moved beyond niobium in general, launching coating activities that use alternative materials for SRF applications. A15 materials such as Nb_3Sn and V_3Si, for example, have the potential to lower even more cryogenic losses in a cavity. Tests with Nb_3Sn fabricated by reactive evaporation, as done at Cornell, indicate that it could already outperform bulk niobium, though this largely depends on a high quality bulk niobium cavity as a substrate. Herein, researchers are seeing great potential from coating Nb_3Sn onto a copper cavity and subsequently profiting both from thermal stability and reduced material costs.

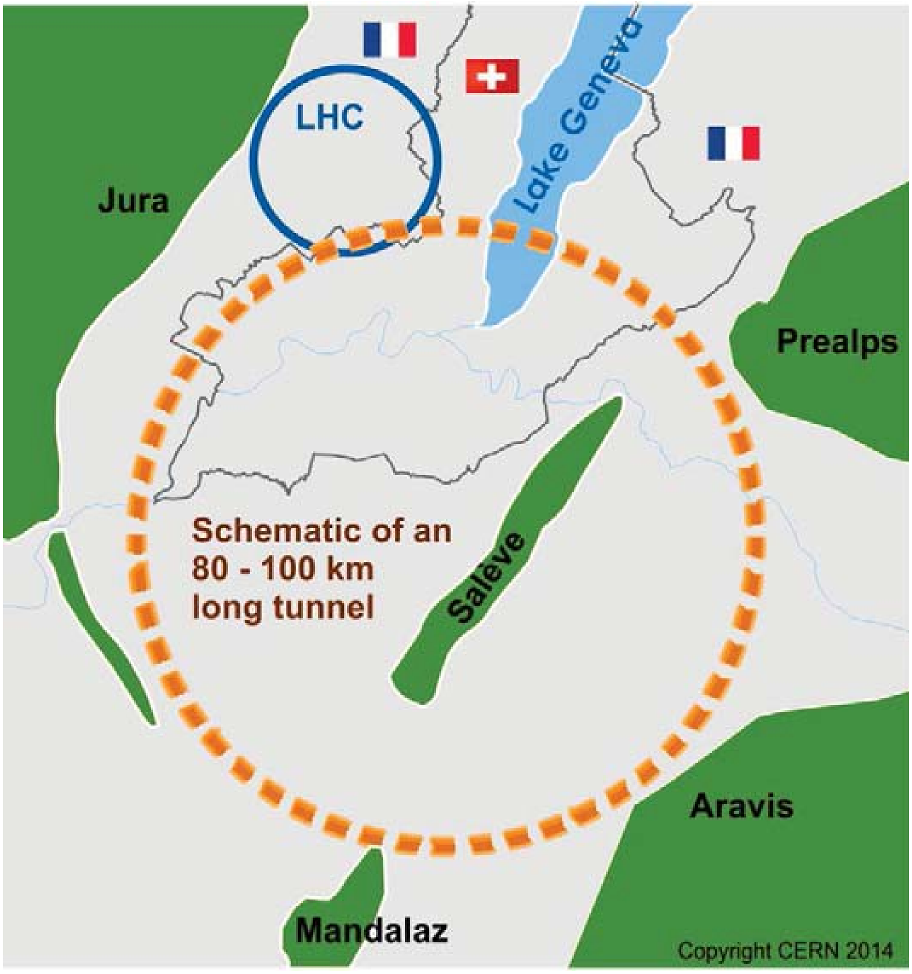

Figure 2.4: Schematic of a 100 km tunnel for a Future Circular Collider in the Lake Geneva basin.

Labs are also investigating new fabrication processes for seamless cavities. Researchers view electro-hydroforming, where the metal sheet is deformed by a shock-wave, as an especially promising candidate as first results have shown excellent mechanical properties. Also within the FCC framework, a collaboration between INFN Legnaro, STFC Daresbury and CERN is dedicated to the development of a process to fabricate 800 MHz seamless cavities by spinning. The team coats these cavities with a high quality film to test and thereafter further understand the relation between coating parameters and SRF performance.

2.2.2 Project with Low beta cavities: ALPI, ISOLDE

2.2.2.1 ALPI: “Acceleratore Lineare Per Ioni”

Dealing with low beta cavities, we can affirm that the first SC QWR was developed around 1970 to build an independent phased superconducting linac for heavy ions to boost the energy of Tandem beams [10]. Such cavities presented many advantages with respect to previously developed resonators: a very broad acceptance in velocity connected to the two-gap structure, an excellent mechanical stability which makes them insensitive to deformation and mechanical vibrations, a shape simple to build, treat and clean and the absence of joints in high current regions. The first SC QWRs were obtained by electroplating Pb on OFHC Cu substrates [11]. The resonator performance was limited to accelerating fields around 3 MV/m. However, such cavities have operated reliably in superconducting linac for heavy ions for many years. Higher accelerating fields were obtained in QWRs when Nb was used as a superconductor. In the first built resonators only the empty inner conductor, filled with liquid He, was prepared in full Nb being both the outer conductor and the shorting plate built in Nb explosively bonded on Cu [12] [13]. The first laboratory, aimed at applying to SC QWR production the Nb sputtered technology developed at CERN, was set up in Legnaro in 1987. The goal was to develop a method for replacing the Pb superconducting layer, conservatively foreseen for the ALPI cavities, with Nb [14].

The superconductive thin film technology was developed and used with great success in different facilities that are using low beta cavities like ALPI (which stands for “Acceleratore Lineare Per Ioni” in Italian) at Legnaro Laboratory and Isolde at CERN.

ALPI was entirely designed by LNL accelerator physicists and technologists and started operation in the mid-90's. It is a linear accelerator facility placed next to the Tandem XTU accelerator installed in Legnaro laboratory. The ALPI cavities, Figure 2.5, are assembled in groups of 4 into special cryostats. ALPI accelerating cavities are of the QWR type, having the shape of a coaxial cable section, short-circuited at one end (where the RF magnetic field is maximum), and open at the other (where the RF electric field is maximum).

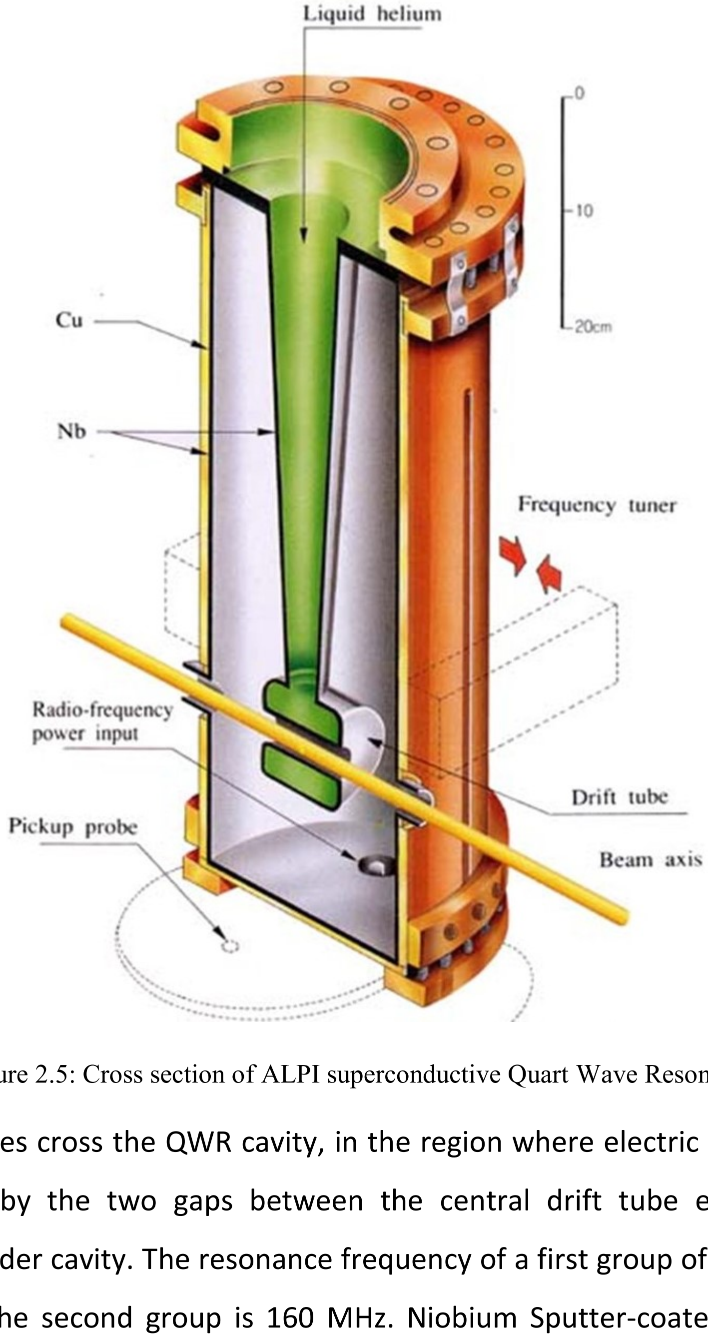

Figure 2.5: Cross section of ALPI superconductive Quart Wave Resonator.

Ion bunches cross the QWR cavity, in the region where electric field is higher and are accelerated by the two gaps between the central drift tube electrode and the surrounding cylinder cavity. The resonance frequency of a first group of ALPI cavities is 80 MHz, while for the second group is 160 MHz. Niobium Sputter-coated Copper Cavities provide an optimal solution for high performance resonators. Sputtering solution is an attractive alternative to bulk Niobium due to the improved thermal conductivity of a few microns of Niobium sputtered onto OFHC Copper and the significant reduction of material costs, even when heavy ion resonators are involved like in ALPI facility. Niobium sputtering in a Biased DC Diode configuration has been investigated for Legnaro OFHC Copper QWRs. Q-values of the order of 10^9 and accelerating fields over 6 MV/m at 7 Watt are routinely achievable. These results obtained by investigating a simplified model of QWR without beam-ports, have been replied without any problem when sputtering a real accelerating resonator complete of beam-ports and tuner.

The goal of the ALPI Project was to build a linac, consisting of 93 independently phased Nb coated superconducting resonators, which act as a booster for the 16 MV tandem accelerator (Figure 2.6).

Figure 2.6: (Left) Portion of the ALPI linac at LNL: highlighted are the cryostats. (Right) the interior of a cryostat, lodging 4 accelerating, high purity copper-based, cavities.

2.2.2.2 ISOLDE: Isotope Separator On Line DEvice

Due to the positive experience of ALPI accelerator other low beta facilities were developed around the world. A further example will be ISOLDE (Isotope Separator On-Line facility) upgrade at CERN. The ISOLDE facility is an ISOL-based radioactive beam facility at CERN. It is dedicated to the production and research of nuclei far from stability. The HIE-ISOLDE upgrade (HIE stands for High Intensity and Energy), intends to improve the experimental capabilities at ISOLDE over a wide front. Major project components include a new superconducting (SC) linear accelerator (LINAC) based on QWRs for the post-acceleration and the necessary 4.5 K cryogenic station for helium. For this facility, it has been necessary to design and build accelerating cavities with a very high voltage gradient of 6 MV/m and low heat dissipation below 10 W. The superconducting accelerator part dedicated to the increase of energy is based on a QWR geometry with twenty cavities cooled by helium and installed in four cryo-modules. Each cryo-module contains five cavities based on 101.28 MHz niobium-sputtered copper (Nb/Cu) QWR [15].

Figure 2.7: Photo of the elements inside the cryo-module vessel and thermal shield, the five cavities clearly visible [12].

Figure 2.8 shows a rendering of ISOLDE cryostat; Figure 2.7 shows a cryomodule with five assembled QWR cavities.

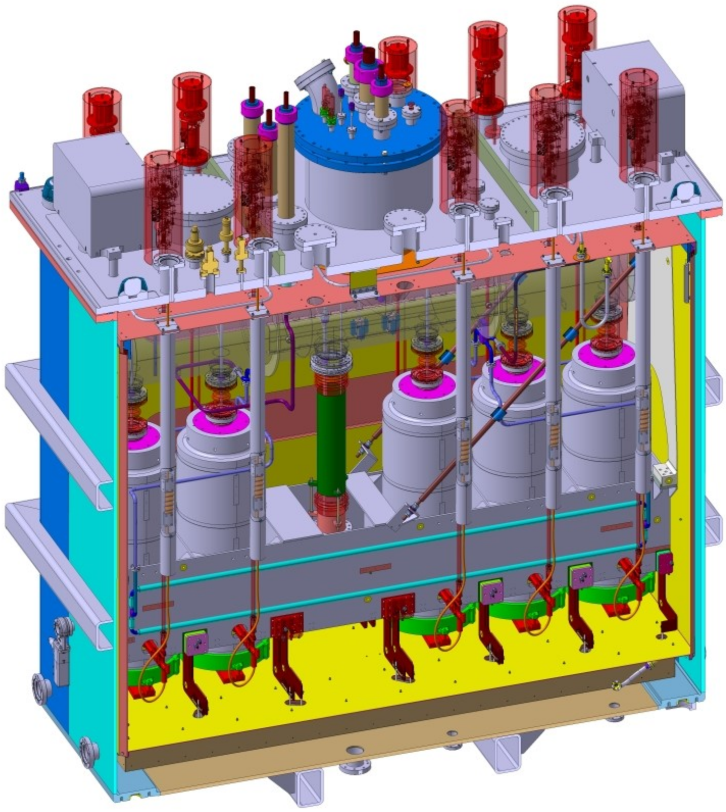

Figure 2.8: Rendering of SC-Linac of HI-ISOLDE Project [16].

2.2.3 Low and middle beta facilities under construction

Thanks to ALPI and HE-ISOLDE success different accelerating facilities with middle beta cavities are under construction or planned in middle future. All SC ion linacs at present are operating at 4K.

2.2.3.1 FRIB: Facility for Rare Isotope Beam

The Facility for Rare Isotope Beams (FRIB) at MSU and RAON in South Korea are the most ambitus project to accelerate Uranium to 200 MeV/u and deliver 400 kW beams to target. These facilities are planned to operate at 2 K. This is consistent with the recent studies finding that operation of TEM-class cavities is more economical at 2 K rather than at 4 K. The 200 MeV/u uranium linac requires approximately 800 MV accelerating voltage. This leads to a large number of accelerating cavities.

Regarding FRIB facility, the superconducting linac consists of 330 individual low β and middle β (β= 0.041, 0.085, 0.29, and 0.53 at 80.5 MHz and 322 MHz) bulk niobium cavities in 49 cryomodules [17].

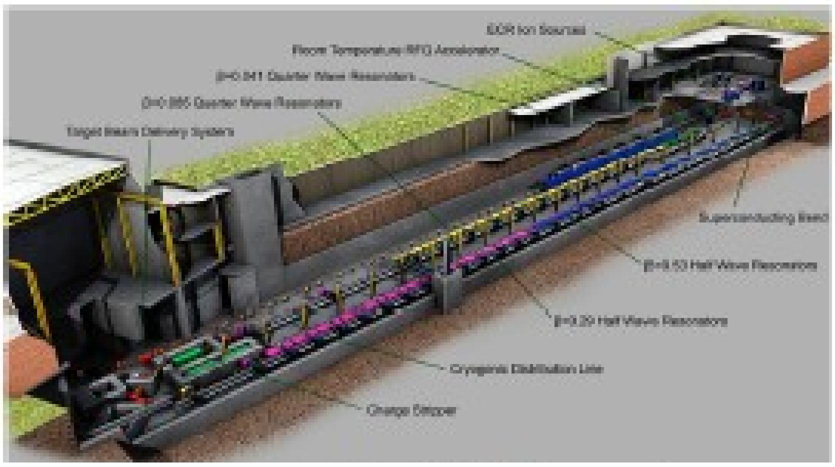

Figure 2.9: Layout of FRIB facility [17].

Cavity design is optimized for optimum performance and also for low production cost. This requirement guided the choice of the cavity geometries, materials and mechanical solutions, avoiding complicated shapes, minimizing the amount of electron beam welds, eliminating bellows, optimizing construction and surface treatment procedures. FRIB cavities will work with superfluid helium at 2 K. The increase in cavity Q more than compensates the energy required for the 2 K cryogenic system operation. This innovative choice in a low-medium β linac allows operation of cavities in stable pressure conditions with high safety margin on the maximum surface fields [18].

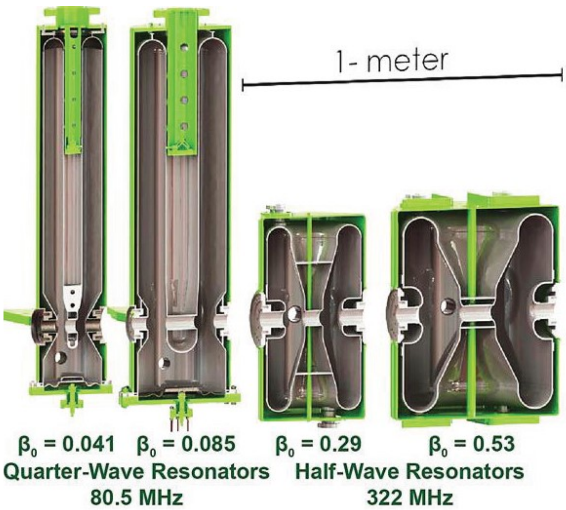

Figure 2.10: The FRIB driver linac requires four different cavity types as shown [17].

2.2.3.2 RAON

Following FRIB design and success, in South Korea another facility with similar performances is under design and construction: RISP stands for Rare Isotope Science Project. This facility will include RAON (that is a native Korean word meaning "Happy" or "Joyful") that will be the heavy ion accelerator [19].

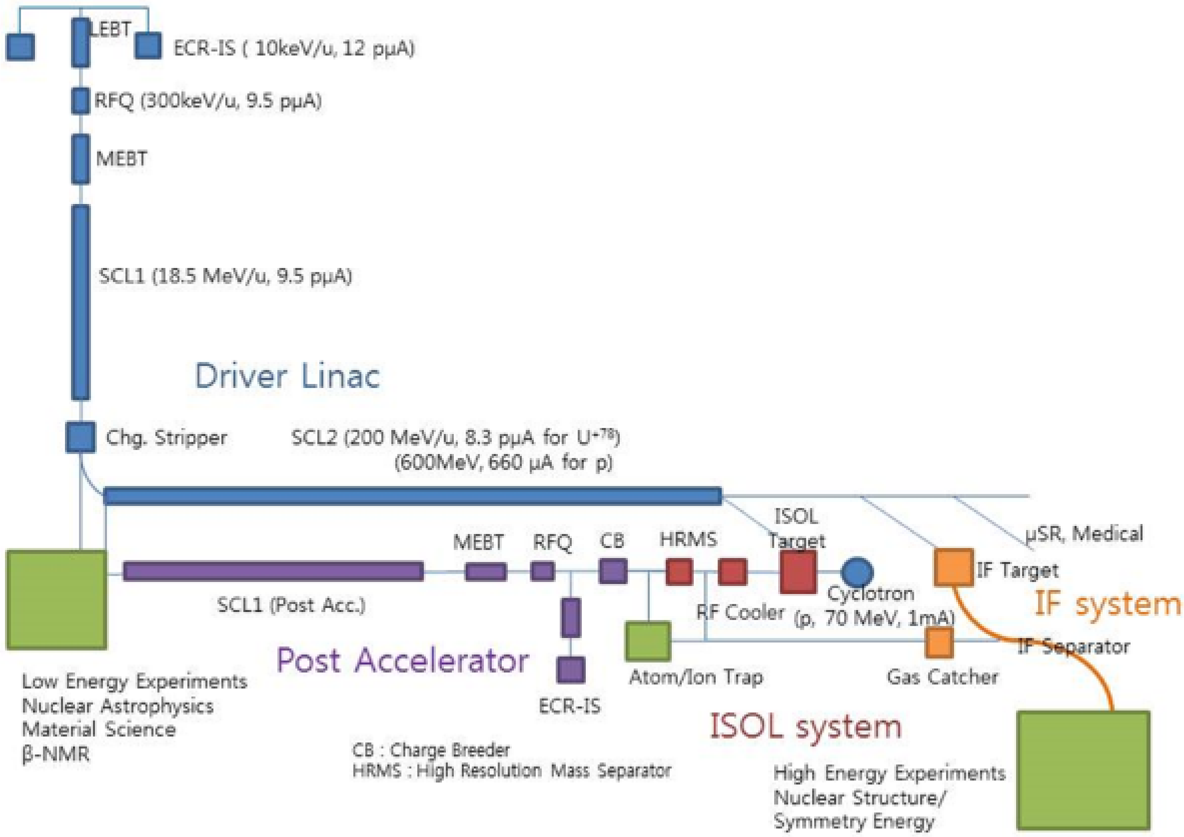

Figure 2.11: Layout of RISP accelerator [19].

To achieve high performances mentioned above, the superconductive RAON linac is designed to accelerate high intensity heavy ion beams. Large cavity apertures (40 and 50 mm) are chosen to reduce uncontrolled beam loss on the superconducting cavities because beam loss is a serious issue for superconducting accelerators. The superconducting linac, in this case, consists of 386 individual low β and middle β Niobium bulk (β=0.047, 0.12, 0.30, 0.53) [20] (Figure 2.12).

Figure 2.12: Rendering of superconductive cavities that will be used in RAON linac.

2.2.4 SC LINACs for ADS facilities

In parallel to these big facilities which have the purpose of producing radioactive ions beams of instable elements (FRIB and RISP) which are under construction, or big facilities already operating for production of high energetic hadron, electron or proton beams, there is a great effort and R&D on the study of new SC accelerator for Accelerator Driven System (ADS) applications. These facilities are right now under feasibility study. ADS are comprised of high power accelerators supplying a proton beam to a reactor vessel. The reactor vessel could contain nuclear fuels such as used Uranium or Thorium. The proton beam will be used to produce neutrons by spallation in the reactor vessel. If ILC will no longer be built, ADS accelerators will definitely be the future of SRF technology. Indeed, ADS in combination with thorium or other advanced nuclear fuels are very real options to be considered to provide electrical energy with a reduced CO_2 footprint. In addition new advanced nuclear system such as ADS have the energy density that allows a small enough facility size when we consider highly populated countries with little free land available. In addition this technology will allow new options in fuel recycling and end storage, largely reducing the issues that conventional nuclear facilities have when using Uranium. SRF accelerators could be used directly to destroy very long-lived isotopes with the proton beam using either fission or transmute them via neutrons into a martial with much shorter half-life [21].

2.2.4.1 MYRRHA: Multy-porpouse Hybrid Research Reactor for High-tech Applications

One facility, now under design, is MYRRHA (Multi-purpose hybrid research reactor for high-tech applications) that will be built in Belgium. It will be equipped with a superconductive linear accelerator delivering a Continuous Wave (CW) proton beam of up to 4 mA at an energy of 600 MeV. The design of MYRRHA assumes that from 17 MeV, a fully modular superconducting LINAC accelerates the proton beam up to the final energy, over a total length of about 240 m from the ion source. Such CW linac is composed by an array of independently-powered spoke and elliptical cavities with high energy acceptance and moderate energy gain per cavity – low number of cells and very conservative accelerating gradients (around 50 mT and 25 MV/m peak fields nominal operation point) – in order to increase as much as possible, the tuning flexibility and provide sufficient margins (about 20 to 30%) for the implementation of the fault-tolerance capability [22].

2.2.4.2 CIADS: Chinese Initiative Accelerator Driven System

In parallel to this project, another facility is under test and under construction in China at Lanzhou for the same purpose: CIADS (Chinese Initiative Accelerator Driven System). As the completion of the R&D of the key component, ADS further development needs a big project with much more investment. Meanwhile, the nuclear power development in China becomes much faster than ever before. In this situation, Chinese Academy of Sciences decided to put much more efforts on ADS next step development. A long-term road map was sketched out, as shown in (Figure 2.13) [23]. According to this plan, the future development is divided into three steps, as follows:

1) From 2011 to 2017 will be built an ADS test facility, called CIADS, which is the abbreviation of Chinese Initiative Accelerator Driven System. It is the first coupled system of a high intensity proton accelerator with subcritical reactor through a neutron target. The thermal power of the reactor is designed at 4 MW. It is driven by a 40 MeV proton linac consisting of an ECR proton source, a RFQ, room temperature CH cavities and a section of superconducting spoke cavity.
2) From 2017 to 2022, the same linac in the first step will be prolonged with more superconducting spoke cavities and medium-β superconducting ellipsoid

cavities to increase the proton beam energy to about 600 MeV. It is coupled with a new subcritical assembly of 80-100 MW thermal power through a spallation neutron target of liquid metal. This is a medium scale ADS facility.

3) From 2022 to 2032, a whole scale ADS demonstration facility will be built with thermal power of 1000 MW. More superconducting ellipsoid cavities will be added to the linac to raise beam energy up to 1.5 GeV.

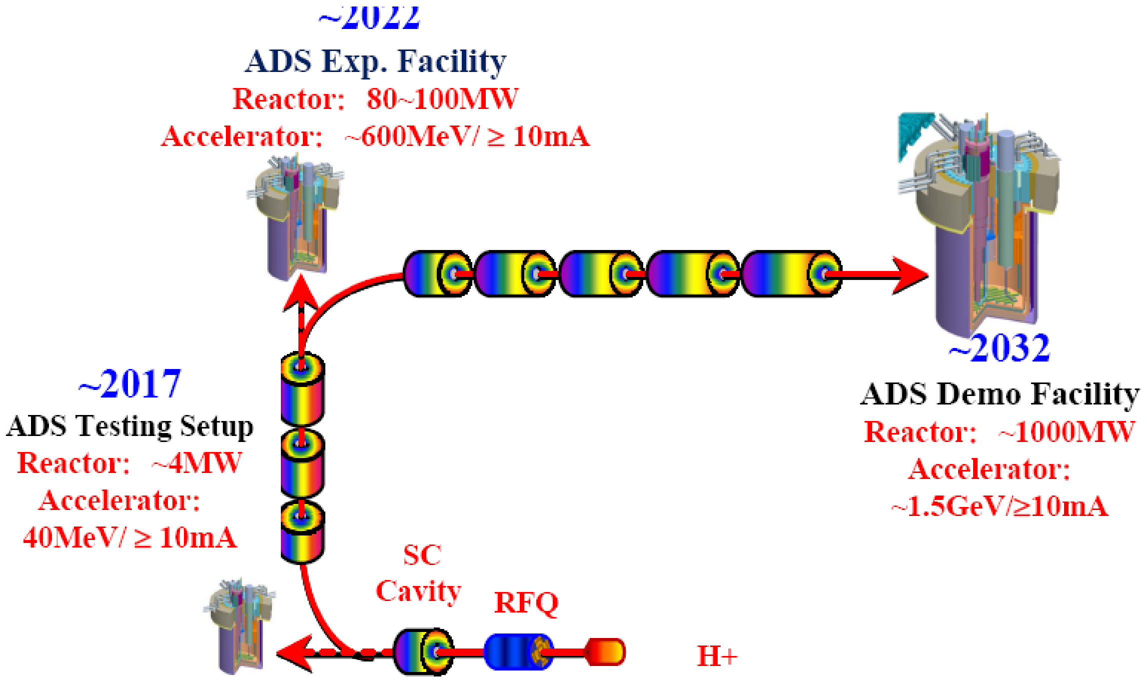

Figure 2.13: The road map of ADS development in China [23].

2.3 Summary of operational and future SC ion LINACs

The first CW SC ion accelerators have been built to boost the energy after DC accelerator such as pelletrons or tandems. Bollinger gives in a review of SC linacs [10]. In the past decades the scientific community has increasingly demanded accelerated CW stable and radioactive ion beams which ca be efficiently provided by SC ion linacs like the examples discussed in the above paragraphs. The existing facilities are being refurbished and upgraded to higher energies and beam intensities. Several new projects are under development or construction worldwide. Table 2-1 summarizes the main parameters of existing and planned SC ion linacs.

Table 2-1: Overview of existing and planned superconducting ion accelerators [24].

Laboratory	Cavity Type	Frequency (MHz)	Lowest q/A	Cavity β	N. of cavities
Argonne (after intensity upgrade)	QWR, split rings	48.5, 72.75, 97, 109.27	1/7	0.025, 0.038, 0.077, 0.105, 0.15	53
INFN – LNL	RFQ, QWR	80, 160	1/7	0.047, 0.11, 0.13	80
TRIUMF	QWR	106, 141	1/5	0.057, 0.071, 0.11	40
IUAC New Dely	QWR	97	1/7	0.051, 0.08	28
ReA3 (MSU)	QWR	80.5	1/4	0.041, 0.085	16
SARAF Ph II	HWR	176	1/2	0.08, 0.16	28
GANIL	QWR	88	1/3	0.07, 0.12	26
FRIB (MSU)	QWR, HWR	80.5, 322	1/7	0.041, 0.085, 0.29, 0.53	340
HIE ISOLDE	QWR	101.28	1/4.5	0.063, 0.103	32
RAON	QWR, HWR, SSR	81.25, 162.5, 325	1/7	0.047, 0.12, 0.3, 0.53	386

2.4 Summary of operational and projected SC proton LINACs

The first SC proton linac for high power beams that went into operation is the Spallation Neutron Source (SNS) H^- linac at ORNL [25]. SNS is a user facility built to provide 1.4 MW of beam power at an energy of 1,5 GeV.

Common to all project is the use of multi-cell elliptical cavities above a specific beam energy. Designers usually try to minimize the number of different cavity types in order to reduce the engineering effort and production cost. Differences between the projects can be observed for the low-energy end. Many project favor spoke cavities as transition between the very low energy NC front ends and the SC ellyptycal cavities, while others exclude spoke cavities to save on engineering effort or simply because spoke cavities have so far not been employed in operational linacs. Table 2-2 summarizes the main parameters of existing and planned SC ion linacs.

Table 2-2: Overview of existing and planned superconducting proton linacs [24].

Laboratory	Cavity Type	Frequency (MHz)	Cavity geometry β	Energy (GeV)	P beam (MW)
SNS	Elliptical	805	0.61, 0.81	1	1.4
Project X	HWR, spoke, elliptical	162.5, 325, 650, 1300	0.094, 0.19, 0.43 0.61, 0.9, 1	1, 3, 8	1, 3, 0.4
ESS	Spoke, elliptical	352, 707	0.5, 0.65, 0.86	2	5
Eurisol	HWR, spoke, elliptical	176, 352, 704	0.09, 0.15, 0.3 0.47, 0.65, 0.78	1-2	5
Myrrha	Spoke, elliptical	352, 704	0.35, 0.47, 0.65	0.6	2.4
HP-SPL	Elliptical	704	0.65, 1	5	4
LP-SPL	Elliptical	704	0.65, 1	4	0.14
India-ADS	Spoke, elliptical	325, 650	t.b.c., 0.61, t.b.c.	1	30
China-ADS	HWR, spoke, elliptical	162.5, 325, 650	0.12, 0.21, 0.4 0.63, 0.82	1.5	15

Chapter 3

Superconducting Accelerating Cavities

3.1 Accelerating cavities

A cavity resonator is a hollow space region such as a metal box, closed by a surface of conductive material that stores a certain amount of energy in the form of stationary oscillating electromagnetic waves. These structures are microwave resonators which generally derive from a "pillbox" shape (right circular cylinder), with connecting tubes to allow particle beams to pass through for acceleration (Figure 3.1).

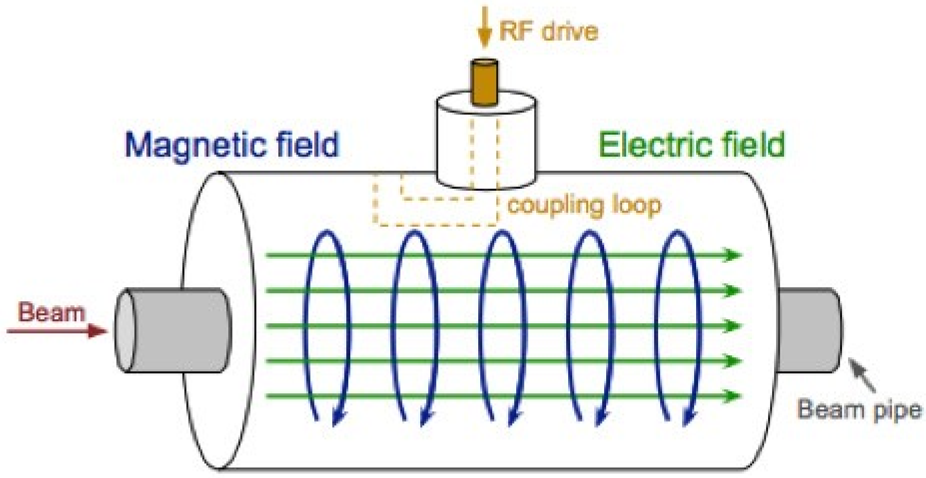

Figure 3.1: scheme of a pillbox cavity. Electric (in green) and magnetic (in blue) fields distribution is visible.

Figure 3.2 shows a typical cylindrically symmetric cavity. The fundamental or lowest RF frequency, mode (TM_{010}) of the cavity has fields as shown. The electric field is roughly parallel to the beam axis, and decays to zero radially upon approach to the cavity walls. Boundary conditions demand that the electric surface be normal to the metal surface. The peak surface electric field is located near the iris, or region where the beam tube joins the cavity. The magnetic field is azimuthal, with the highest magnetic field located near the cavity equator. The magnetic field is zero on the cavity axis.

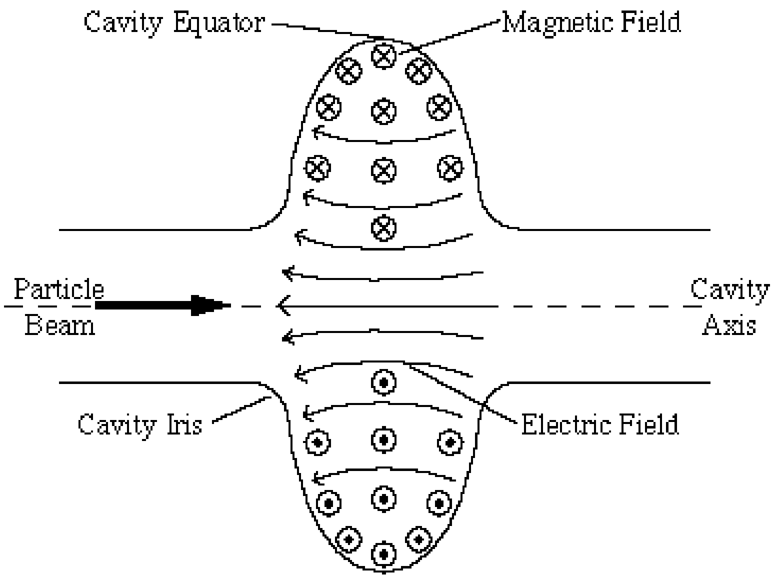

Figure 3.2: Scheme of accelerating elliptical cavity. It is visible also magnetic and electric field distribution inside the cavity.

Accelerating cavities are used to increase the energy of a charged particle beam; indeed, an RF cavity is the device through which power is coupled into the particle beam of an accelerator. Obviously, the energy gain per unit length is therefore an important parameter of such devices. This is conveniently derived from the accelerating voltage (V_c) to which a particle with charge *e* is subjected while traversing the cavity:

$$V_c = \left|\frac{1}{e} \times energy\ gain\ during\ transit\right| \tag{3-1}$$

For particles travelling with the velocity of light *c* on the symmetry axis in *z*–direction (ρ= 0) and an accelerating mode with eigenfrequency ω this gives:

$$V_{acc} = \left|\int_0^d E_z(z) e^{\frac{i\omega z}{c}} dz\right| \tag{3-2}$$

The accelerating field is:

$$E_c = \frac{V_c}{d} = \frac{V_c}{\beta\,\lambda/2} \tag{3-3}$$

Other important parameters for an accelerating structure are the surface resistance (R_s), the geometry factor (*G*), the dissipated power (P_d), the stored energy (*U*), the *Q* value and of course E_{pk} and H_{pk}, which denote the highest electric and magnetic field on the surface of the resonant structure; above this level the material becomes normal conducting [26].

In an ideal situation, one can keep feeding the power to the resonant cavity until the peak magnetic field reaches the critical RF magnetic field, a little higher than the thermodynamic critical magnetic field for niobium (a meta-stable superconducting state under superheated critical magnetic field). For a typical tesla-type cavity, the theoretical maximum accelerating gradient is about 55 MV/m [27]. At the moment the standard E_{acc}, achievable in the industrial production, is about 25-30 MV/m for working tesla-type accelerating cavities based on bulk niobium material.

In order to sustain the radiofrequency fields in the cavity, an alternating current is

flowing in the cavity walls. This current dissipates power in the wall as it experiences a surface resistance. One can look at the power which is dissipated in the cavity to

define the global surface resistance:

$$P_d = \frac{1}{2}\oint_A R_s H_s^2 dA = R_s \oint_A H_s^2 dA \tag{3-4}$$

Where H_s denotes the magnetic field amplitude.

The RF power dissipation in a cavity wall (P_c) is characterized by the quality factor Q_0, which tells us how many RF cycles (multiplied by 2π) are required to dissipate the energy U stored in the cavity:

$$Q_0 = \frac{\omega_0 U}{P_c} \tag{3-5}$$

Where:

$$U = \frac{1}{2}\mu_0 \oint_V H^2\, dV \tag{3-6}$$

R_{surf} is the integral surface resistance for the cavity. The surface resistance and the quality factor are related via the geometrical constant G which depends only on the geometry of a cavity and field distribution of the excited mode, but not on the resistivity of the material:

$$G = \frac{\omega_0 \mu_0 \oint_V H^2\, dV}{\oint_A H_s^2 dA} \tag{3-7}$$

The quality factor Q_0 given by eq. (3-5), using eq. (3-6) and (3-4) became:

$$Q_0 = \frac{\omega_0 \mu_0 \oint_V H^2 \, dV}{R_s \oint_A H_s^2 dA} = \frac{G}{R_S} \tag{3-8}$$

The RF magnetic field *H(r)* for the excited eigenmode with angular frequency $\omega_0 = 2\pi f_0$ is integrated over the cavity volume *V* and surface *A*. The surface resistivity R_s quantifies the RF power and depends only on the frequency and intrinsic material properties. It is a function of the RF magnetic field and may therefore vary along the cavity wall. It must be averaged over the cavity surface. The geometry factor *G* is determined only by the shape of the cavity, and hence is useful for comparing cavities with different shapes. The quality factor can also be defined as:

$$Q_0 = \frac{f}{\Delta f} \tag{3-9}$$

where f is the resonance frequency and Δf the full width at half height of the resonance curve in an unloaded cavity.

For the typical elliptical shape of superconducting cavities $G = 270\ \Omega$. For a mono-cell TESLA niobium cavity the quality factor is typically $Q_0 = 1.2 \cdot 10^{10}$ at $T = 2\ K$ corresponding to a surface resistance of $R_s = 10\ n\Omega$. One can see that the efficiency with which a particle beam can be accelerated in a radiofrequency cavity depends on the surface resistance. The smaller the resistance i.e. the lower the power dissipated in the cavity walls, the higher the radiofrequency power available for the particle beam. This is the fundamental advantage of superconducting cavities as their surface resistance is much lower and outweighs the power needed to cool the cavities to liquid helium temperatures.

3.2 Classification of structures

There are three major classes of superconducting accelerating structures: high-, medium-, and low-β. Figure 3.3 shows some practical geometries for each type depending on the velocity of the particles, spanning the full velocity range of particles [24].

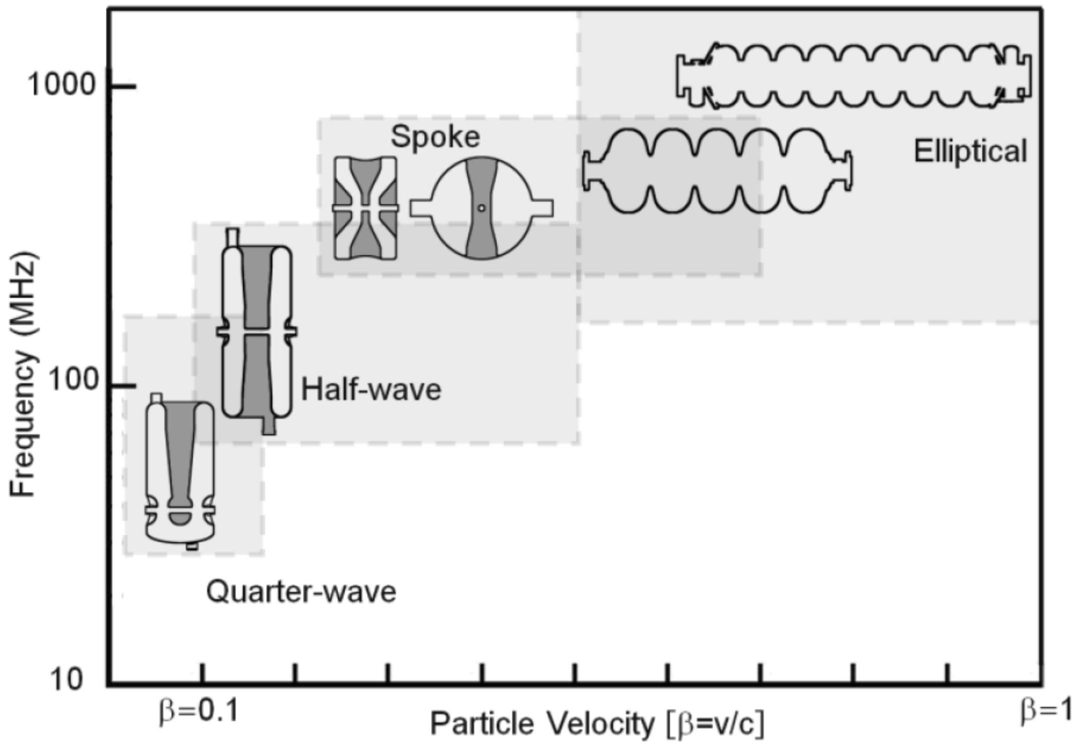

Figure 3.3: Superconducting cavities spanning the full range of β [24].

The high-β structure, based on the TM_{010} resonant cavity, is for acceleration of electrons, positrons, or high-energy protons with $\beta \approx 1$. The cavity gap length is usually $\beta\lambda/2$, where λ is the wavelength corresponding to the frequency choice for the accelerating structure. Medium-velocity structures with β between 0.2 and 0.7 are used for protons with energies lower than 1 GeV as well as for ions. At the higher-β end, these resonators are 'foreshortened' speed-of-light structures with longitudinal dimensions scaled by β. Near $\beta = 0.5$ spoke resonators with single or multi-gaps become popular. Spoke resonators operate in a TEM mode. Elliptical shape cells for β < 0.5 become mechanically unstable as the accelerating gap shortens and cavity walls become nearly vertical. The choice of a low RF, favoured for ion and proton applications, also makes the elliptical cells very large, aggravating the structural weakness.

3.3 High-β cavities

A typical high-β accelerating structure consists of a chain of coupled cells operating in the TM010 mode, where the phase of the instantaneous electric field in adjacent cells is shifted by π to preserve acceleration as a charged particle traverses each cell in half an RF period. Figure 3.4 shows a nine-cell accelerating structure developed by TESLA collaboration, the beam enters and exits the structure via the beam tubes.

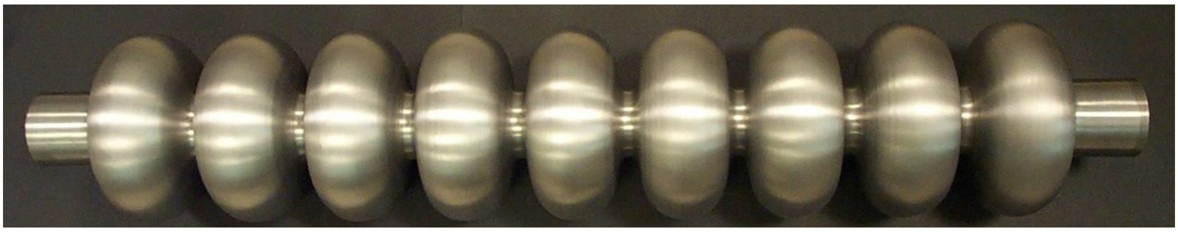

Figure 3.4: Photograph of a nine-cell accelerating structure bulk Nb.

Most $\beta = 1$ structures are now based on the elliptical cavity. The elliptical cell shape [28] emerged from the more rounded 'spherical' shape [29], which was first developed to eliminate multipacting. The tilt of the elliptical cell also increases the stiffness against mechanical deformations and provides a better geometry for acid draining and water rinsing.

3.4 Low-velocity structures

3.4.1 Elliptical Medium-β cavities

With the growing interest in accelerators for spallation sources, as for example the Spallation Neutron Source SNS at Oak Ridge National Laboratory, elliptical resonators have been extended to high energy ($\sim$1 GeV) proton acceleration using medium-β superconducting cavities ($0.6 < \beta < 0.9$). Medium-β cavities are also important for high current proton linacs for injectors at Fermilab and CERN, and in the future for energy production via accelerator driven reactors, material irradiation, and nuclear waste transmutation. The design of a medium-β structure involves several tradeoffs. The choice of a low frequency increases the voltage gain per cell, the beam energy acceptance, and the beam quality, at the same time decreasing RF losses and beam losses. But a low RF increases structure size and microphonics level, making RF control more challenging. The larger the number of cells, the higher the voltage gain per structure, but the narrower the velocity acceptance, and the larger the number of cavity designs needed to optimize the voltage gain with changing particle velocity. In the medium velocity range, structures must efficiently accelerate particles whose velocities change along the accelerator.

Efficient acceleration for $0.5 < \beta < 0.9$ is achieved in a straightforward manner by axially compressing the dimensions of the standard elliptical resonator geometry while maintaining a constant frequency, as shown in Figure 3.5 [30].

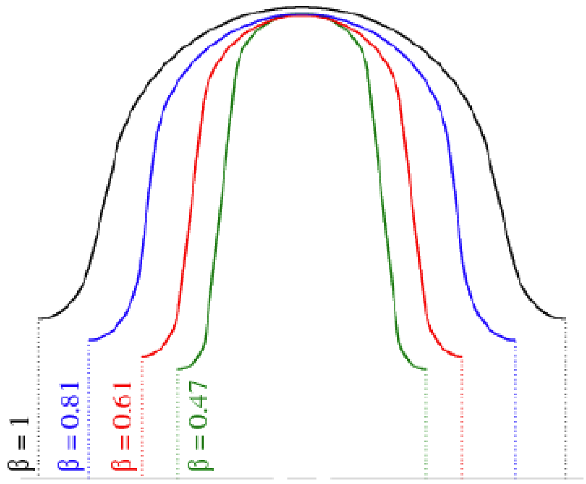

Figure 3.5: A progression of compressed elliptical cavity shapes at the same RF frequency but for decreasing β values [30].

3.4.2 Medium-β spoke resonators

An alternative path to medium-velocity structures with β near 0.5 is via multi-gap spoke resonators (Figure 3.6)

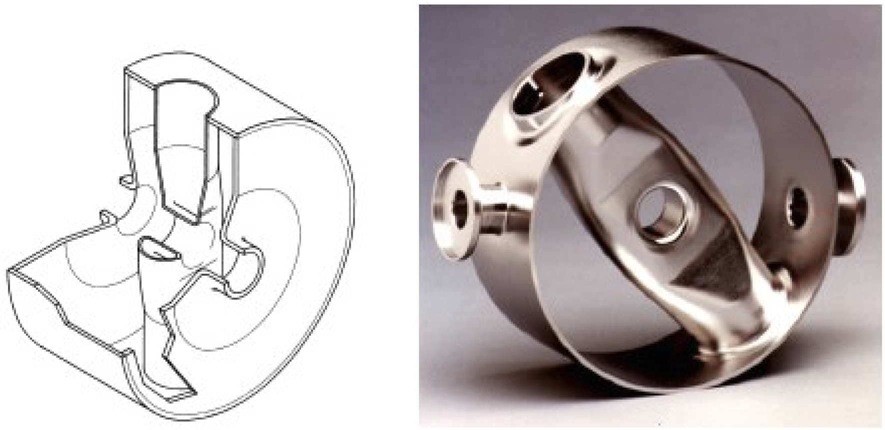

Figure 3.6: 3D sketch and photograph of the first spoke resonator with $\beta = 0.28$, 800 MHz [31].

The spoke elements are made elliptical in cross-section to minimize the peak surface fields. The major axis of the ellipse is normal to the beam axis in the centre of each spoke to minimize the surface electric field and maximize the beam aperture. A typical beam aperture is 4 cm at 345 MHz. In the region of the spokes near the outer cylindrical diameter, the major axis is parallel to the beam axis in order to minimize the peak surface magnetic field.

The range of spoke resonator applications continues to be extended into the medium-β regime. In principle there is no clear-cut transition energy from spoke resonators to elliptical ones. Typically TM cavities have an inside diameter of about 0.9λ. Spoke structures have outer diameters below 0.5λ. Thus, a spoke cavity can be much smaller than an elliptical cavity at the same frequency, or the spoke structure can be made at half the frequency for roughly the same dimensions as the elliptical structure. Choosing a lower frequency allows the option of 4.2 K operation, thus saving capital and operating costs associated with refrigeration [32].

3.4.3 Medium-β Quart Wave Resonators

Low-β resonators have been in use for heavy-ion boosters for more than three decades. The short independently phased cavities provide flexibility in operation and beam delivery. Applications continue to expand towards both the lower-β as well as the medium-β range, as with spoke resonators discussed in section 3.4.2. Low-velocity structures must accelerate a variety of ions with different velocity profiles. Different cavity geometries with many gaps, suitable for different beam energies, beam currents, and mass/charge ratios have been developed.

The Quarter-Wave Resonator (QWR) derives from transmission-line-like elements and belongs to the TEM resonator class. Figure 2.5 and Figure 3.7 show QWR cavities. This structure can be correlated to a coaxial line, $\lambda/4$ in length shorted at one end to form a resonator with maximum electric field at $\lambda/4$, where the accelerating gaps are located [33]. The length of the structure is proportional to $\beta\lambda$, so low frequencies, typically 100–200 MHz, must be used. The low frequency implies a large resonator. The typical structure height is about 1 m. The inner conductor, which is made of niobium, is hollow and filled with liquid helium. Operation at 4.2 K is usually possible due to the low RF.

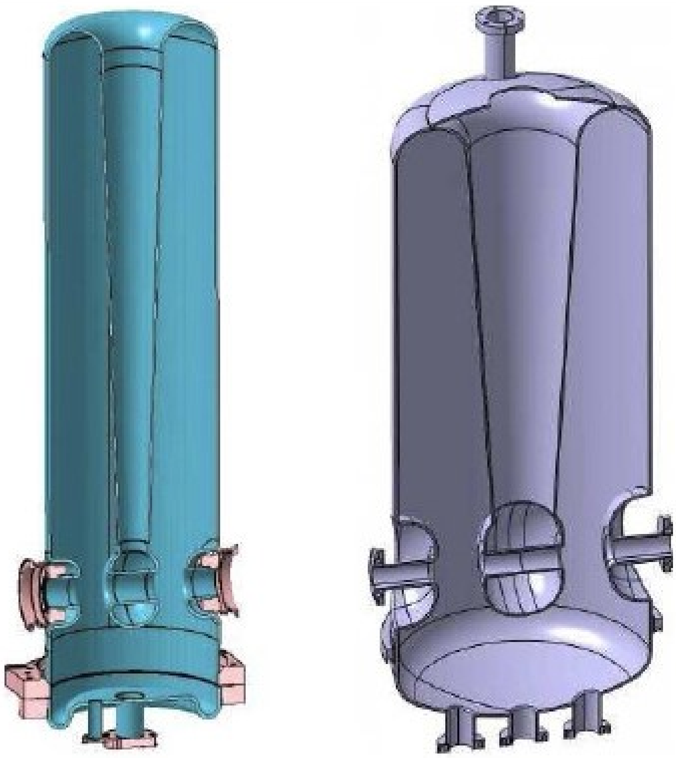

Figure 3.7: Two QWRs for SPIRAL-II with different β values (0.07 and 0.12) [34].

The larger the number of gaps in a QWR, the larger the energy gain, but the narrower the velocity acceptance.

Being a non-symmetric structure, the QWR has non-symmetrical electromagnetic fields in the beam region; this produces undesirable beam steering through electric and magnetic dipole field components. Compensation can be obtained by gap shaping: the magnetic deflection can be cancelled by enhancement of the electric deflection [35].

3.4.4 Half-wave resonators

A half-wavelength (λ/2) transmission line, with a short at both ends, has maximum voltage in the middle and behaves as a half-wave resonator (HWR). A HWR is equivalent to two quarter waves facing each other providing the same accelerating voltage as a QWR but with almost twice the power dissipation. Figure 3.8 shows an example. The symmetry of the structure cancels steering and opens the use of HWRs at β from 0.1 to 0.5, above the range customary for QWRs. HWRs also show improved mechanical vibration properties over QWRs.

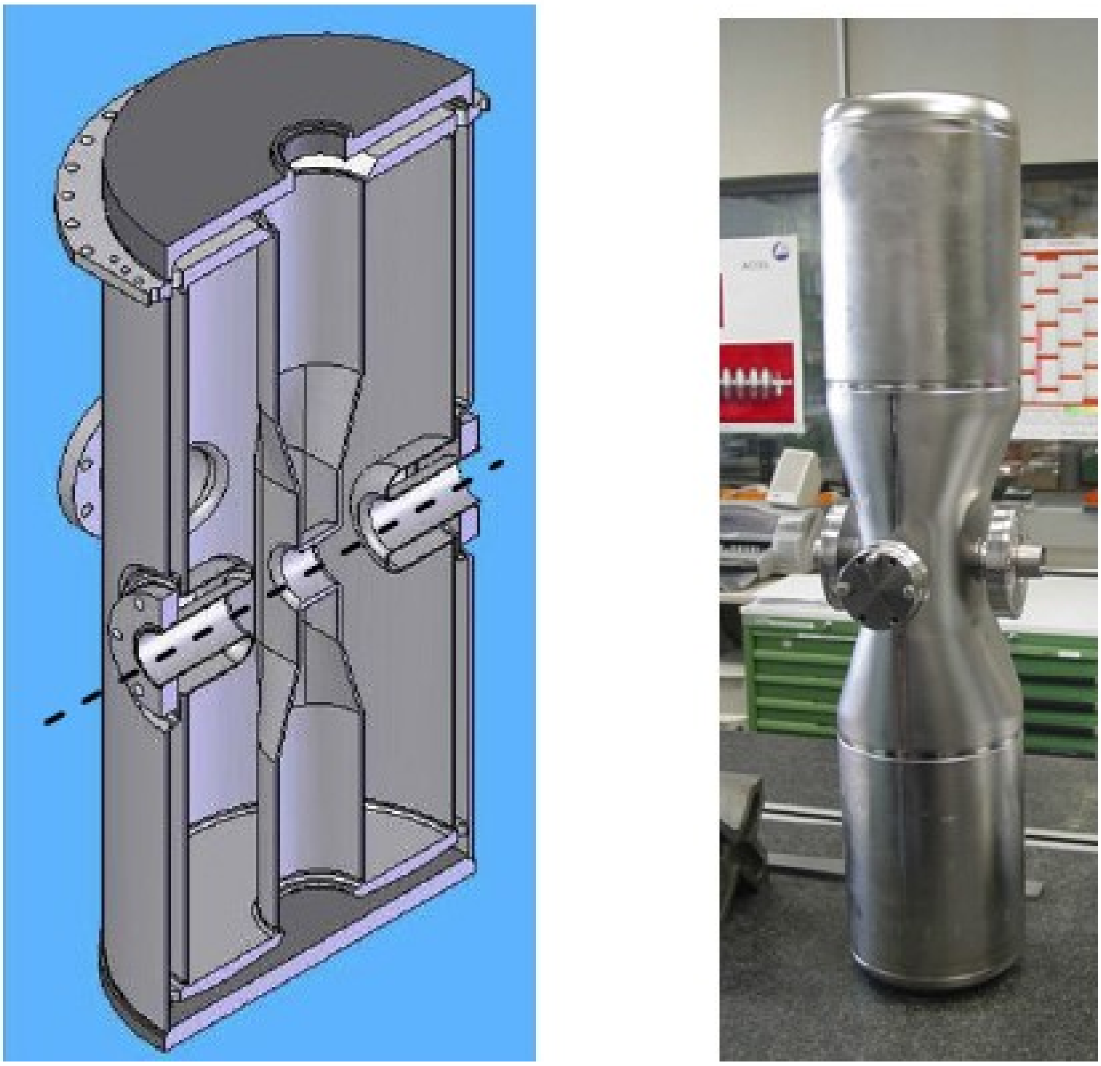

Figure 3.8: Example of a HWR cavity

The peak surface electric field occurs at the centre of the loading element. A surface to accelerating field ratio of 3.3 can be obtained by suitable sizing and shaping of the cross-section, independent of β.

3.5 Niobium properties

Niobium is the 41^{st} element of the periodic table and it is a transition metal of V group and fifth period. Niobium is widely used in metallurgy, jewellery, for nuclear power stations and in the space sciences. Recent research has focused on superconductive properties of niobium and niobium alloys. In the family of superconducting elements, it has the highest critical temperature.

Table 3-1: List of the niobium properties.

Characteristic	Value
Atomic number	41
Atomic mass	92.91 [g/mol]
Melting point	2468 °C
Boiling point	4927 °C
Atomic volume	$1{,}8\cdot10^{-29}$ [m^3]
Vapour pressure @ 2000 K	$2.6\cdot10^{-8}$ [mbar]
Density @ 20°C	8.56 [$gr\cdot cm^{-3}$]
Lattice Structure	b.c.c.
Space group	Im3m
Lattice constant	3.030 [Å]
Hardness @ 20 °C cold-worked	110-180 [HV10]
Hardness @ 20 °C recrystallized	60-110 [HV10]
Young's modulus @ 20 °C	104 [GPa]
Poisson's ratio	0.35
Coefficient of thermal expansion @ 20 °C	$7{,}1\cdot10^{-6}$ [m/(m·K)]
Thermal conductivity @ 20 °C	52 [$W\cdot m^{-1}\cdot K^{-1}$]
Electrical conductivity @ 20 °C	$7\cdot10^{6}$ [$\Omega^{-1}m^{-1}$]
Specific electrical resistance @ 20 °C	0.14 [($\Omega\cdot mm^2$)/m]
Critical temperature	9.26 [K]
Debye Temperature	275 [K]
Specific Heat @ 20°C	0.27 [$kJ\cdot kg^{-1}K^{-1}$]

The Nb is a lustrous, grey, ductile, paramagnetic metal, although it has an atypical configuration in its outermost electron shells compared to the other elements on its group. Its crystal system is based on body centered cubic (BCC) and it is considered a refractory metal due to its very high melting point. In the family of superconducting element, it has the highest critical temperature and its properties are collected on Table 3-1 [36].

3.6 Problem in bulk Nb cavities operation

3.6.1 Quench in bulk Niobium due to low thermal conductivity

The performance of a superconducting cavity is limited by a quench or breakdown of superconductivity. The thermal breakdown (quench) is a heating that originates in a submillimeter-size regions of high RF losses, called defects. If the temperature of a good superconductor outside the defect exceeds the superconducting transition temperature (T_c), the RF losses increase considerably, as a growing region becomes normal conducting, leading to a rapid loss of stored energy called “quench”. An obvious approach to avoid quench is to prepare the niobium material with great care to keep it free from defects [37].

One method of insurance against thermal breakdown is to raise the thermal conductivity of niobium by raising the Residual Resistivity Ratio. With high thermal conductivity metal, any large defect can tolerate more power before driving the neighboring superconductor into the normal state. Normal material quality control and treatment procedures should avoid such large defects. However, with 10000 cavities there is the possibility of encountering a few [37].

3.6.2 Multipacting

Multipacting is a resonant process where an electron emitted from the surface of a cavity, for example by a cosmic ray, is accelerated by the RF field. When the particle impacts the surface again it produces secondary electrons. The secondaries are accelerated as well and produce further secondary electrons. A resonant process starts, where the number of impacting electrons increases exponentially. When these secondary electrons happen to hit the same area, the absorbed rf energy heats the surface, thus creating a local hot spot.

This, not only limits the accelerating gradient, but it also creates more RF surface loss, even leading to a possible thermal quench. By adjusting the resonant cavity shape, the multipacting can be reduced but it cannot be totally eliminated.

Therefore, in elliptical cavities one-point-multipacting is not an issue anymore. Two points multipacting may still occur but it is rather rare. This scenario is more common in other RF components such as coaxial lines, couplers, heavy ion cavities or parallel plate geometries [1].

3.6.3 Field emission

Another important phenomenon limiting the E_{acc} from reaching its maximum, is the field emission. When the surface electrical field is strong enough for that small area, the electrons will start to tunnel out of the metal surface to form a steady current. The field emission current rapidly increases as the field is increased. Like the multipacting phenomenon, it absorbs a great amount of rf power, depositing the heat wherever the electrons hit. Part of the heating is strong enough to cause the resonant cavity to lose the superconducting state.

3.6.4 Problem of cost

Last but not least, is the problem of Niobium price. In 2014 superconductive Niobium with RRR>300 cost more than 500 €/kg. If in future the idea of building ILC takes hold, the problem of Nb cost will be critical. An accelerator like ILC with more than 15K cavities, that weighs about 23.5 kg each, without thinking of the scrap material, will be impossible to be built if other cheaper cavities production technique will be developed.

3.7 Bulk Niobium for accelerating cavities

Niobium as a pure element has the highest critical temperature (9,26 K in its bulk form) and also the highest thermodynamic critical field ($1.6 \cdot 10^5\ A/m$). The mechanical properties of Niobium are good enough to machine the cavities that require a precise handling. In superconductive resonator it is mandatory to have high values of Quality factor (Q), as high as possible. In order to have a Q value of 10^{10} at 1.8 K, the surface resistance should be at 4.2 K around 900 nΩ and few nΩ at 1.7 K for the TESLA type cavities; there is a strong dependence of the surface resistance with the temperature. The residual surface resistance of Niobium sheets can be from few nΩ to several hundreds of nΩ and it is related to the surface preparation and purity.

However, a high quality niobium must be used due to the presence of high accelerating fields that can decrease the thermal conductivity and break the superconducting state. For this reason, it is useful to develop purification techniques and electropolishing methods that minimize the presence of defects on the surface [38].

3.7.1 Bulk Niobium accelerating cavities

The traditional fabrication procedure of elliptical SRF cavities consists of deep drawing and electron beam welding (EB) of the half cells. This procedure is well established and has about 30 year of industrial fabrication experience. It is well known that RRR degradation in welding areas of conventional cavities can be critical for the cavity performance [39]. In the last few years improvement of the material quality control, preparation for EB welding and the welding parameters allowed to reach accelerating gradients close to the theoretical limit by applying advanced cavity treatment techniques such as electropolishing (EP) in combination with baking [40]. The disadvantage of this method is that welding at the equator and iris of cells is very critical for rf performance, because they will be exposed to high magnetic or electric fields.

Nevertheless not only the progressive achievement of higher accelerating fields, but also the drastic reduction in resonator production time and costs (K€ per MV/m) is compulsorily for the feasibility of more and more powerful accelerators. This is the motivation under the research toward simpler and cheaper fabrication techniques as, for instance, seamless cavities.

Therefore, a fabrication method, which will avoid the welding, is very complementary for two aspects:

1) the seamless cavity does not have the risk of equator weld contamination;
2) a lower cost of fabrication can be expected.

The development of the seamless technique mostly for the TESLA shape cavity was mainly pursued in the last years at INFN by V. Palmieri (spinning) [41], [42] and at DESY (hydroforming) [43] by W. Singer.

3.7.2 Spinning

Plastic deformation of metals by spinning is a powerful technique, in fact it has been shown that seamless resonators can be cold formed starting either from circular at blanks or from tubes without need of any intermediate annealing. In the optics of a low cost resonator mass production, a strong effort on fabrication times reduction (around 4 hours per resonator) has been spent in the last two years at INFN. However, much shorter fabrication times are possible and are under study at the moment. Several years of development were necessary to build the TESLA shape multicell cavities, with a ratio of equator diameter to iris diameter of about three.

The spinning fabrication technique and performance of the spun cavities is described in details in reference [41]. A bulk niobium 1.3 GHz 9-cell cavity was produced [42].

Cavities after spinning must be internally tumbled or mechanically grinded, then chemical and electro polished.

Low temperature radiofrequency tests have proofed that the seamless approach and in particular spinning is a solution worthwhile to pursue. Q-values over 10^{10} and accelerating fields over 40 MV/m were reproduced on all the last spun prototypes fabricated at LNL of the INFN. Multi-cell cavities either in Niobium or Copper can be formed both directly from circular blanks and from tubes.

Spinning of seamless Niobium or Copper nine-cell cavities is not a problem for LNL Laboratory. Figure 3.4 shows one seamless 9-cell Nb cavity.

3.7.3 Hydroforming

The hydroforming is performed by expanding a seamless tube with internal water pressure while simultaneously swaging it axially. Prior to the expansion the tube is necked at the iris area and at the ends. Tube radii and axial displacements are computer controlled during the forming process in accordance with results of finite element method simulations for necking and expansion using the experimentally obtained strain-stress relationship of tube material. The combination of tube necking in the iris area and subsequent tube expansion in the equator area permitted to achieve a more or less homogeneous distribution of the stress around the tube and therefore the forming without damage. This procedure eliminates the intermediate annealing during hydroforming of single-cell as well as multicell cavities [39].

3.8 Niobium/Copper Clad Cavities

The spinning and hydroforming techniques can be applied also to seamless bimetallic tubes [44]. This option opens new opportunities for cost savings and performance improvements. The material combination of clad, thin niobium (0.5 to 1 mm thickness) on 2–3 mm thick copper saves material costs for the expensive niobium and increases the thermal stability of the cavity against quench, due to the high thermal conductivity of copper and by applying this technique to spinning and hydroforming in cavity fabrication can eliminate electron beam welding. It keeps the niobium bulk property.

Additionally, cladding permits to retain almost all treatment procedures applied to bulk Nb such as BCP, EP, annealing at 800 °C, in situ baking at 120 °C, HPR and CBP.

INFN-LNL successfully fabricated three Nb/Cu clad cavities. The cavity wall thickness was 0.5 mm with niobium and 2 mm with copper. The clad cavities were electropolished and cold tested in KEK. One of them achieved 25 MV/m in accelerating field gradient (E_{acc}) without any steep Q-dropping [45].

3.9 Nb/Cu accelerating cavities

Superconducting cavities produced by the magnetron sputtering technology have been successfully used at CERN, and are also employed in several other present or future accelerator facilities, such as ALPI (INFN, Legnaro, Italy) or SOLEIL (St-Aubin, Gif-sur-Yvette, France) for acceleration.

The advantages are higher thermal stability from the high thermal conductivity of the oxygen-free, copper substrate, and, undoubtedly, the reduced material cost. There is also a fortuitous order of magnitude lower sensitivity of the Nb layer's resistance to external DC magnetic fields, reducing the magnetic shielding requirements for cryomodules which house the Nb–Cu cavities. The simple explanation of the insensitivity of Nb on Cu films to dc magnetic field penetration is that the Nb films have a low electron mean free path and high H_{c2}. The best films are obtained by cylindrical magnetron sputtering onto a copper cavity substrate. Other coating techniques are under investigation such as: DC post magnetron, biased DC magnetron deposition, vacuum arc coating, ECR, HIPIMS, etc. Great care has to be taken to produce a smooth and clean surface without pores and inclusions. Electropolishing and chemical polishing techniques have been developed to produce copper surfaces of roughness less than 20 nm. This is particularly important since the overlaying Nb grain size is of the order of 100 nm.

3.9.1 Nb/Cu working cavities with high-β: LEP2 and LHC @ CERN

A successful example is certainly LEP at CERN in Genève. The superconducting rf system of LEP consisted of 288 four-cell standing wave cavities which operated at 352 MHz and had an active length of 1.7 m. The first 16 cavities were constructed of solid Nb and had a nominal accelerating gradient of 5 MV/m. All the other cavities were made of Cu with a thin film of Nb sputtered on the cavity walls. The nominal gradient for the latter cavities was 6 MV/m. The Cu substrate gives a high mechanical stability and makes the cavities virtually quench-free due to its high thermal conductivity. The cavities were mounted in groups of four in one cryostat, called a module. They were immersed in a liquid He bath at 4.5 K [46].

The niobium/copper (Nb/Cu) sputter technology, successfully used on a large scale for LEP2, has been applied to the LHC and reduced-β superconducting cavities.

For the LHC RF system the SC cavities were chosen, not only because of their high accelerating field leading to a small contribution to the machine impedance, but also because of their high stored energy which minimizes the effects of periodic transient beam loading associated with the high beam intensity (0.5 A). There will be eight single-cell cavities per beam, each delivering 2 MV (5.3 MV/m) at 400 MHz [47].

3.9.2 Nb/Cu working cavities with low-β: ALPI and ISOLDE

ALPI is the Legnaro super-conducting linac for heavy ions, in operation since 1994 [48]. Originally, the sputtered medium β cavities installed in ALPI were Pb plated and only later, they were renewed by substituting the original metal coating with a Nb layer deposited by DC bias sputtering.

Since the very beginning of the ALPI project two R&D programmes were launched, one on the sputtering of Cu bases with Nb and the other on the realization of full Nb cavities [49]. These programmes, which proceeded in parallel, brought ALPI to the outstanding result of an accelerating field of $\approx 6\ MV/m$ in 1993.

Given the success of the R&D, it was decided, in the second phase of ALPI, to build the higher β section with the Nb on copper technique. By means of new design details, along with a careful and long setup of the delicate sputtering procedure, the first results were confirmed and exceeded in a number of tests, showing an average accelerating field off-line $E_a \sim 6 \div 8\, MV/m$ at P_d=7 W (with $Q_0 \sim 6 \div 7 \cdot 10^8$ at the high field values). The technology has been applied to on-line resonators.

Figure 3.9: High β Quarter Wave Nb/Cu sputtered Resonator reaching 7 MV/m installed in ALPI accelerator at LNL.

At the moment 52 quarter wave Nb/Cu resonators (Figure 3.9) are mounted and working at LNL.

Following LNL success, also HIE-ISOLDE was designed taking into account Niobium/Copper technologies. The HIE-ISOLDE superconducting linac is based on quarter wave resonators (QWRs), made by niobium sputtering on copper. The operating frequency at 4.5 K is 101.28 MHz and the required performance for the high beta cavity is 6 MV/m accelerating field for 10 W maximum power dissipation. The ISOLDE specifications call for an average surface resistance of 65 nΩ at 6 MV/m accelerating field, corresponding to the performance achieved in the best ALPI cavities.

3.9.3 Future opportunities for Nb/Cu sputtered cavities

A large number of laboratories around the world are continuing the development with 1.5-GHz single-cell and multi-cells cavities in an effort to evaluate Nb–Cu technology at higher frequencies (>1 GHz) desired for future large-scale applications such as ILC.

There are clearly defined sets of accelerator machine parameters where films show a clear advantage compared to bulk niobium, in particular for low frequencies or for operation at 4.2 K. However, Niobium films still have not achieved their possible ultimate performance, contrary to what has been obtained with niobium sheet cavities, and this hinders at present their use for electron linacs although their cost is far inferior. Several novel developments in coating technology are however under study which, on the grounds of the present understanding, may produce an important leap forward.

3.10 Copper properties

Copper was the first metal to be melted from its mineral, c. 5000 BC, the first metal to be cast into a shape in a mould, c. 4000 BC, and the first metal to be purposefully alloyed with another metal, tin, to create bronze, c. 3500 BC [50].

Copper is the 29th element of the periodic table and it is a soft, malleable, and ductile metal with very high thermal and electrical conductivity. Copper is used as a conductor of heat and electricity, as a building material, and as a constituent of various metal alloys, such as sterling silver used in jewellery, cupronickel used to make marine hardware and coins, and constantan used in strain gauges and thermocouples for temperature measurement.

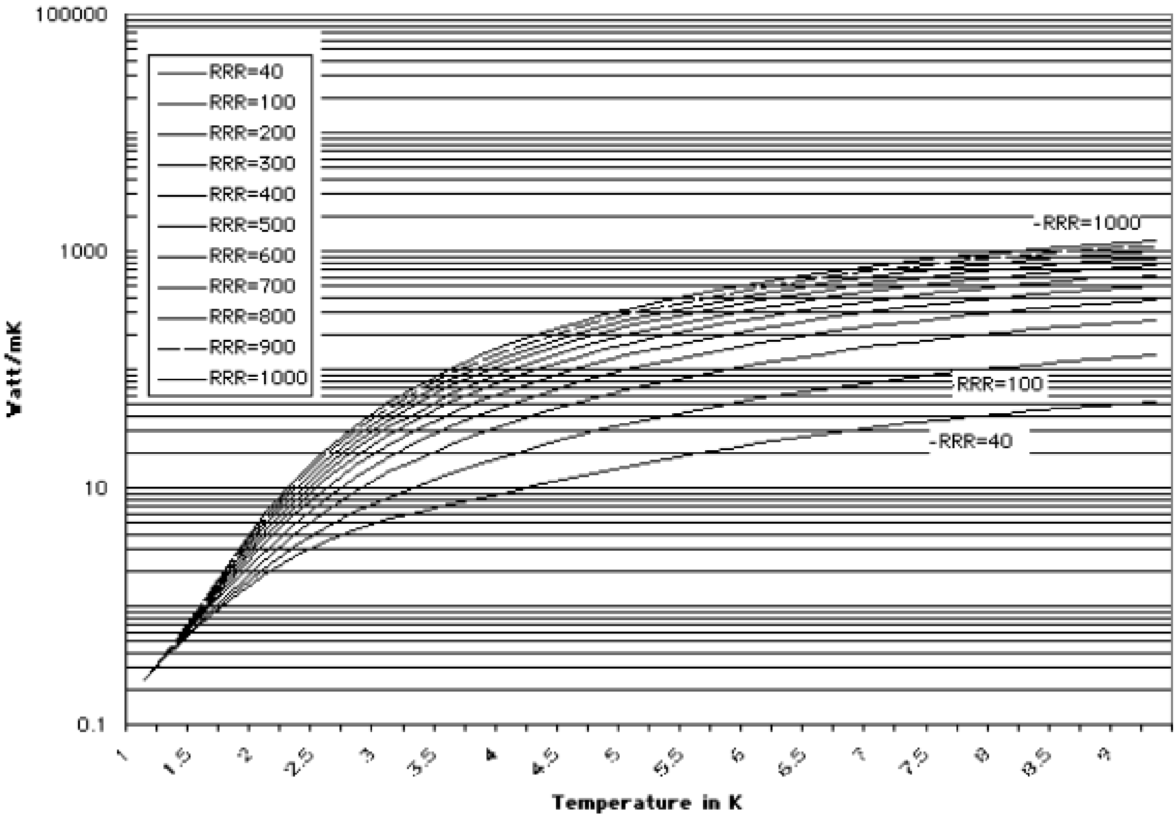

Figure 3.10: Calculated thermal conductivity of Nb as RRR (and purity) increase [27].

A strong motivation for using thin films of Nb onto copper cavities is to provide increased stability against thermal breakdown of superconductivity. The thermal conductivity of copper at 4.2 K is between 300 and 2000 $Wm^{-1}K^{-1}$, depending on the purity and annealing conditions, as compared to the thermal conductivity of 300 RRR of niobium, which is 75 $Wm^{-1}K^{-1}$ at 4.2 K (Figure 3.10) [27]. The cost saving of niobium material is another potential advantage.

Table 3-2: List of the Copper OFHC properties.

Characteristic	Value
Atomic number	29
Atomic mass	63.546 [g/mol]
Melting point	1085 °C
Boiling point	2562 °C
Atomic volume	$1{,}82 \cdot 10^{-29}$ [m^3]
Vapour pressure @ 1000 K	$1 \cdot 10^{-8}$ [mbar]
Density @ 20°C	8.9 [$gr \cdot cm^3$]
Lattice Structure	f.c.c.
Space group	Fm3m
Lattice constant	3.614 [Å]
Hardness @ 20 °C cold-worked	80-115 [HV10]
Hardness @ 20 °C recrystallized	45-80 [HV10]
Young's modulus @ 20 °C	117 [GPa]
Poisson's ratio	0.31
Coefficient of thermal expansion @ 20 °C	$16.6 \cdot 10^{-6}$ [$m/(m \cdot K)$]
Thermal conductivity @ 20 °C	401 [$W \cdot m^{-1} \cdot K^{-1}$]
Electrical conductivity @ 20 °C	$6 \cdot 10^{7}$ [$\Omega^{-1} \cdot m^{-1}$]
Specific electrical resistance @ 20 °C	0.0167 [$(\Omega \cdot mm^2) \cdot m^{-1}$]
Debye Temperature	315 [K]
Specific Heat @ 20°C	0.39 [$kJ \cdot kg^{-1} K^{-1}$)]

Chapter 4

Fundamentals of Superconductivity

4.1 Superconductivity

In 1911, the physicist H.K. Onnes, of Leiden Laboratory in the Netherlands, was measuring the resistivity of metals at low temperatures. He discovered that the resistance of mercury completely disappeared when the temperature dropped to that of liquid helium (4.2 K). This phenomenon became known as superconductivity. In 1933, German scientists W. Meissner and R. Ochsenfeld found that the magnetic flux completely disappeared from the interior of materials with zero resistance when cooled to 4.2 K in the magnetic field. This zero magnetic field inside a material became known as perfect diamagnetism and is now called the Meissner effect. By now a large number of elements and compounds (mainly alloys and ceramics) have been found showing this behaviour. A superconductor has several main macroscopic characteristics, such as zero resistance, the Meissner effect, the Josephson effect, the isotope effect, anomalous specific heat capacity and abnormal infrared electromagnetic absorption.

For superconducting cavities niobium shows the most interesting properties.

The temperature at which the resistance is close to zero is called critical temperature Tc and it is different in each material with superconductive properties. The highest critical temperature between pure metals is shown by niobium, $T_C = 9.25\ K$; and the lowest has been found by tungsten, $T_C = 0.0154\ K$.

4.1.1 Zero-Resistance

The zero resistance characteristic of the superconductor refers to the phenomenon that resistance abruptly disappears at a certain temperature. It is able to transport direct current (DC) without resistance in the superconducting state. If a closed loop is formed by a superconductor in which a current is induced, the induced "persistent current" will show no obvious signs of decay for several years. The upper limit of resistivity measured by the "persistent current" experiment is less than $10^{-27} \Omega \cdot m$, while a good conventional conductor, such as copper, has a resistivity of $10^{-10}\Omega \cdot m$ at 4.2 K, which is more than 17 orders of magnitude than that of the superconductor. The typically experimental dependence of resistance on temperature in a superconductor is shown in Figure 4.1, in which the resistivity of the superconductor suddenly falls to zero when the temperature reduces to a certain value below the critical temperature Tc.

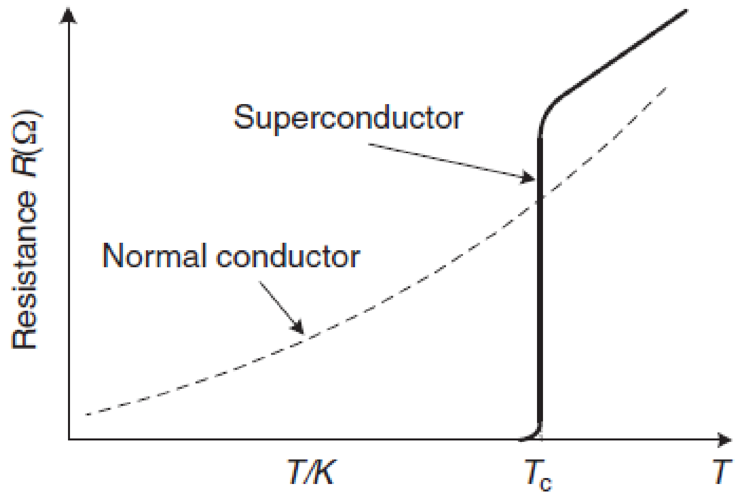

Figure 4.1: Resistance versus temperature curve of superconductors and normal conductors.

4.1.2 Meissner Effect

When the superconductor is subjected to a magnetic field, in a non-superconducting state, the magnetic field can penetrate the superconductor and so the inner magnetic field is not zero in its normal state.

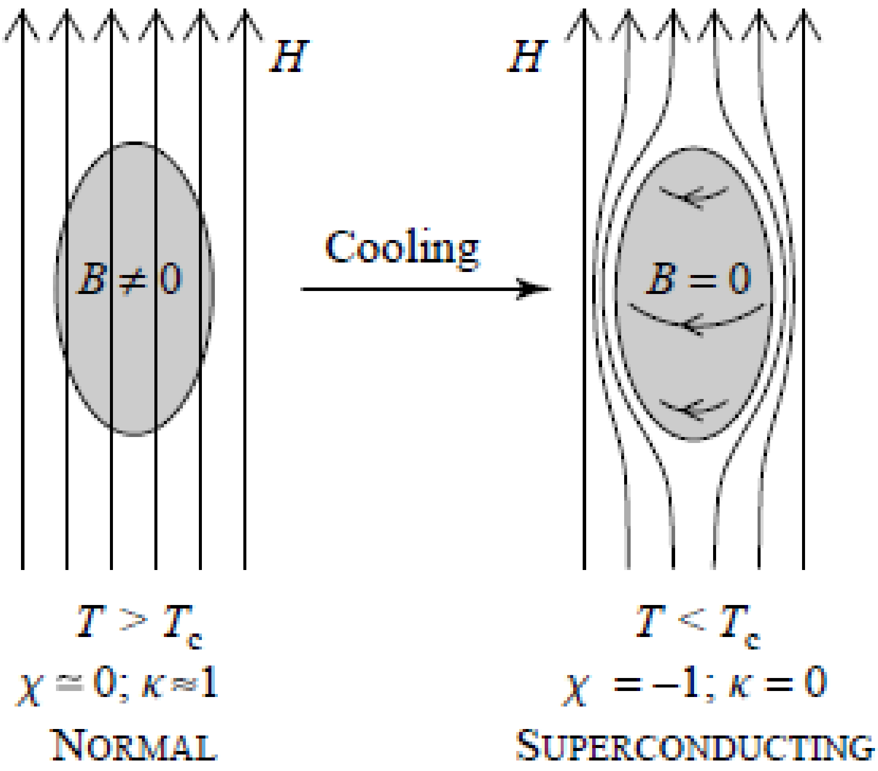

Figure 4.2: Meissner effect and levitation of superconductor: (left) normal state; (right) Meissner state.

However, when the superconductor is in a superconducting state, the magnetic flux within is completely excluded from the superconductor, and the inner magnetic field is zero, that is, the superconductor is completely diamagnetic (Figure 4.2). This phenomenon is called the Meissner effect.

Superconductors lose their superconductivity when the magnetic field strength exceeds a certain value in the external magnetic field. The magnetic field strength that causes a superconductor to lose its superconductivity is called the critical field strength and is denoted by H_c. When the temperature is less than critical temperature T_c, H_c is a function of temperature and continuously increases with temperature decrease following the formula:

$$H_c(T) = H_c(0)\left[1 - \left(\frac{T}{T_C}\right)^2\right] \quad (4\text{-}1)$$

For a practical superconductor, there are usually two critical fields, namely the upper critical field H_{c2} and the lower critical field H_{c1}. When the field H is less than H_{c1}, the superconductor is in the Meissner state; however, when the field H is larger than H_{c2}, the superconductor is in the normal state; while the field H is between H_{c1} and H_{c2}, the superconductor is in the mixed state.

4.1.3 Type I superconductor

Type I superconductors, also known as Pippard superconductors, have only one critical magnetic field B_c.

If the temperature is below the critical temperature ($T < T_C$) and external magnetic field $B < B_C$, the superconductor is in the Meissner state, namely it shows perfect diamagnetism and the magnetic field inside is zero, and magnetization M is equal to magnetic field strength H and both N and H are opposite in direction, that is, $M = -H$. As the external magnetic field increases and reaches the critical magnetic field $B_C = \mu_0 H_C$, the superconductor immediately turns into the normal state from the superconducting state (Figure 4.3).

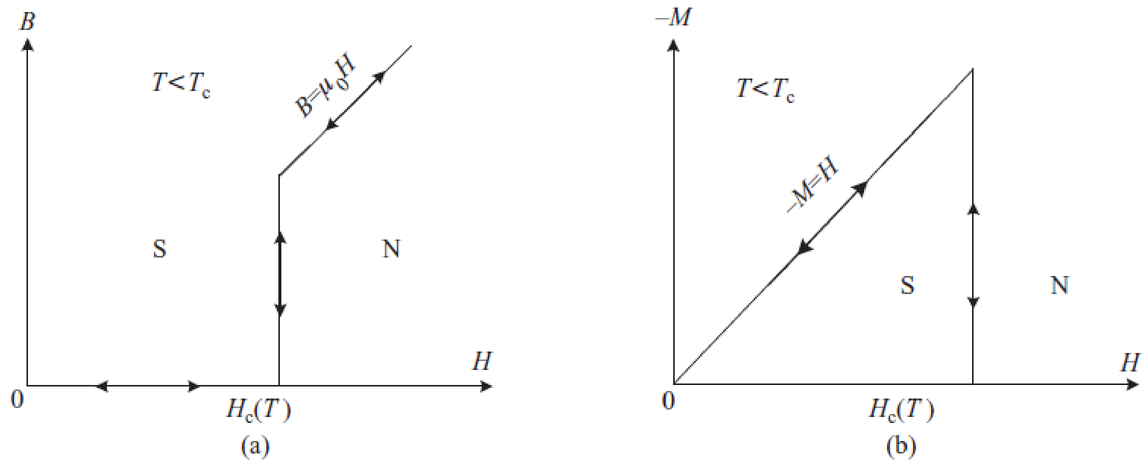

Figure 4.3: Magnetic field (a) and magnetization (b) of Type I superconductor [51].

4.1.4 Type II superconductor

Unlike the Type I superconductor, the Type II superconductor has two critical magnetic fields, which are separately defined as the lower critical magnetic field $B_{C1} = \mu_0 H_{C1}$ and the upper critical magnetic field $B_{C2} = \mu_0 H_{C2}$, when subjected to temperature T below the critical temperature T_c. Similarly, both of them are also dependent on temperature. When the external magnetic field B satisfies $B < B_{C1}$, the superconductor stays in the Meissner state (S1) and then has full diamagnetism with a zero magnetic field throughout (Figure 4.4).

When the external magnetic field B is in the range of $B_{C1} < B < B_{C2}$, the superconducting state and normal state coexist, which is known as a mixed state (S2), and the flux lines can go through the normal region inside the superconductor, which is known as the flux vortex area.

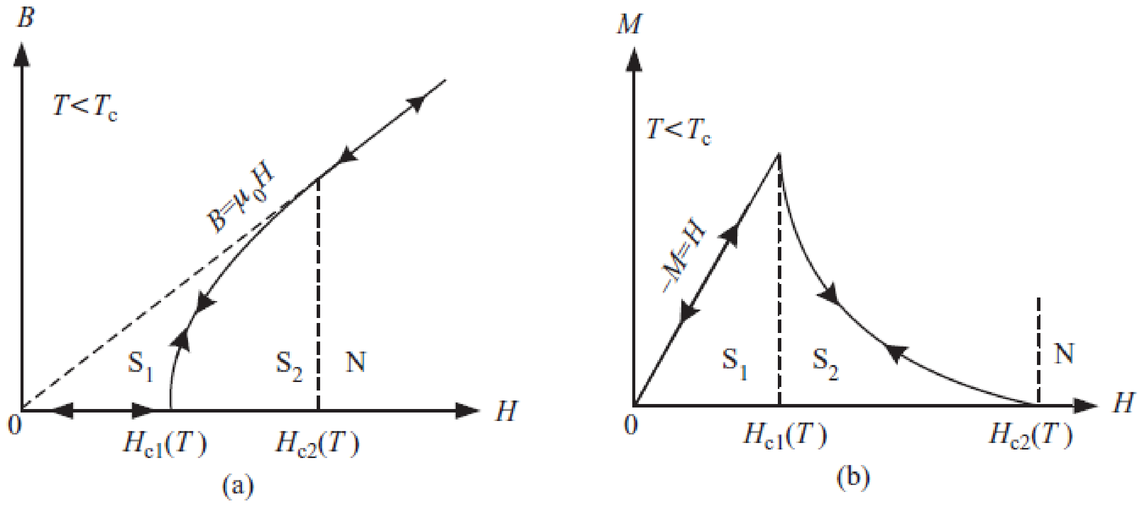

Figure 4.4: Magnetic field (a) and magnetization (b) of ideal Type II superconductors at temperature T [51].

4.1.5 Coherence Length

For classical superconductors like lead or tin, a very successful microscopic theory was developed by Bardeen, Cooper and Schrieffer, which is called BCS theory [52]. Based on the BCS theory, superconductivity results from formation of Cooper pairs, which act as carriers without resistance. However, the binding energy between two electrons of Cooper pairs is weak, but the correlation distance of two electrons ξ is long. ξ is called the coherent length and can reach up to 10^{-4} cm, which is more than 10^4 times that of the lattice size. It is given by:

$$\xi = \frac{\hbar v_F}{\Delta} \tag{4-2}$$

v_F denotes the velocity of the electrons near the Fermi level and 2Δ is the energy necessary to break up a Cooper pair. Typical values for the coherence length in niobium are around 39 nm.

4.1.6 London Penetration depth

Respect type I superconductor, the magnetic field is not completely expelled, but penetrates inside the material over a small distance, otherwise the shielding current density would be infinitely large. The distance called "London penetration depth" is given by the characteristic length of the exponential decay of the magnetic field inside the superconductor:

$$H(x) = H(0)e^{-\frac{x}{\lambda_L}} \tag{4-3}$$

And its value is:

$$\lambda_L = \sqrt{\frac{m}{\mu_0 n_s q^2}} \tag{4-4}$$

where m is carriers mass, q carriers charge and n_s the number of superconducting charge carriers per unit volume. The magnetic field does not stop abruptly at the superconductor surface but penetrates into the material with exponential attenuation.

Here, it is appropriate to remark that in the BCS theory not single electrons but pairs

of electrons are the carriers of the supercurrent. Their mass is $m = 2m_e$, their charge $-2e$, their density $n_c = n_s/2$. Obviously, the penetration depth remains unchanged when going from single electrons to Cooper pairs.

A typical value for the penetration depth in niobium is 32 nm at T=0K.

The theory did not allow for impurities in the material nor for a temperature dependence of the penetration depth. The scientists Gorter and Casimir introduced the two-fluid model where a coexistence of a normal and superconducting fluid of charge carriers is postulated.

$$n_c = n_s + n_n \tag{4-5}$$

They suggested also a temperature dependence of the superconducting charge carriers.

$$n_s(T) = n_s(0)\left(1 - \left(\frac{T}{T_c}\right)^4\right) \tag{4-6}$$

Combining equations (4-4) and (4-6), the London penetration depth became:

$$\lambda_L(T) = \lambda_0 \left(1 - \left(\frac{T}{T_c}\right)^4\right)^{-\frac{1}{2}} \quad (4\text{-}7)$$

According to the Ginzburg–Landau theory, superconductors can be classified into two categories based on the ratio of penetration depth λ to coherence length ξ. By defining the Ginzburg–Landau parameter κ as:

$$\kappa = \frac{\lambda_L}{\xi_0} \quad (4\text{-}8)$$

κ is a parameter that allows to identify the two types of superconductors:

- $\kappa < \frac{1}{\sqrt{2}}$ superconductors have positive interface energy and are called Type I superconductors;
- $\kappa > \frac{1}{\sqrt{2}}$ superconductors have negative interface energy and are called Type II superconductors.

Niobium has $\kappa \approx 1$ and is a weak type-II superconductor.

The role of impurities was studied by Pippard [53], the study was based on the evidence that the penetration depth depends on the mean free path of the electrons in the material. The dependence of ξ on the mean free path is the following:

$$\frac{1}{\xi} = \frac{1}{\xi_0} + \frac{1}{\ell} \quad (4\text{-}9)$$

Pippard introduced an effective penetration depth:

$$\lambda_{eff} = \lambda_L + \left(\frac{\xi}{\xi_0}\right)^{\frac{1}{2}} \quad (4\text{-}10)$$

Here again ξ_0 is the characteristic coherence length of the superconductor. This relation reflects that the superconducting penetration depth increases with a reduction of the mean free path [54]. For pure ("clean") superconductor ($\ell \to \infty$) one has $\xi = \xi_0$. In the limit of very impure ("dirty") superconductors where $\ell \ll \xi_0$, the relation becomes instead:

$$\xi = \ell \quad (4\text{-}11)$$

The mean free path in the niobium is strongly influenced by interstitial impurities like oxygen, nitrogen and carbon.

4.2 Microwave skin effect in normal metals

If a RF electromagnetic field is oscillating inside the cavity, only the electrons of a thin layer called skin depth on the resonator walls, are interacting with the radiofrequency field and the loss are confined in such a layer [55].

There is an analogy between the shielding mechanism of a microwave field in a normal conductor and the shielding of a static magnetic field in a superconductor. If a microwave of frequency is incident on a metal surface, the field decays over a distance (skin depth).

If a microwave of frequency ω is incident on a metal surface, the field decays over a characteristic distance, the skin depth δ. For the case where the frequency is much lower than plasma frequency ($\omega \ll \omega_{plasma}$) and the mean free path of the electrons ℓ is smaller than the skin depth (δ):

$$\delta = \sqrt{\frac{2}{\sigma \mu_0 \omega}} \tag{4-12}$$

where σ is the conductivity of the metal. The surface resistance can be calculated:

$$R_{surf} = \frac{1}{\sigma \delta} = \frac{\rho}{\delta} \tag{4-13}$$

4.3 Anomalous Skin Effect (ASE)

At sufficiently low temperatures and high frequencies, the mean free path of the electrons in a good conductor becomes greater than the classically predicted skin depth, and the classical skin effect equations break down.

Observing Eq. (4-13), the resistance decrease at cryogenic temperatures because σ increase when $T \rightarrow 0$.

Respect pure metals, at low temperatures ℓ may be larger than δ which leads to the anomalous skin effect; in this case the electrons can be scattered not only by phonons but by impurities in the lattice. The surface resistance in the extreme anomalous limit $\ell \rightarrow \infty$, valid for very good conductors such as copper at low temperatures, is given by the following equation:

$$R_{surf} = \left[\sqrt{3}\left(\frac{\mu_0}{4\pi}\right)^2\right]^{\frac{1}{3}} \omega^{\frac{2}{3}}(\rho\ell)^{\frac{1}{3}} \tag{4-14}$$

The product $\rho\ell$ is a material constant and it is $6.8 \times 10^{16}\ \Omega m^{-2}$ for copper. If one were to operate a 1.5 GHz copper cavity at cryogenic temperatures such as, for example, 4.2 K, rather than 300 K, the surface resistance would decrease by a factor of ≈ 0.14, which is not sufficient to justify the cost of a refrigerator.

4.4 Surface Resistance in RF @ low temperature

Unlike the DC case, superconductors in RF fields do not have zero resistance at finite temperatures. This is because a time-dependent magnetic field within the penetration depth generates an electric field (Faraday's law) that acts on normal electrons, as they are not shielded from it by the superconducting electrons (which form 'Cooper pairs' of mass twice that of a single electron) due to their inertia. The normalconducting electrons start to flow and dissipate power. This gives rise to a resistance which depends on the number of normalconducting electrons and the frequency of the alternating current.

An analytical approximation of the BCS surface resistance valid in the local limit, for $T < T_C/2$ and $\omega < \Delta/\hbar$, is given by [24]:

$$R_{BCS} \approx \frac{\mu_0^2 \omega^2 \lambda^3 \sigma_1 \Delta}{\mathrm{k}_B \mathrm{T}} ln\left(\frac{2.246\mathrm{k}_B\mathrm{T}}{\hbar\omega}\right) exp\left(-\frac{\Delta}{\mathrm{k}_B\mathrm{T}}\right) \tag{4-15}$$

considering the case of niobium (λ=40 nm, σ^1=3.3×10^8 S·m^{-1}, Δ/k_BT_c=1.85, T_c=9.25 K) at 2.0 K and 1.5 GHz, we obtain $R_{BCS}\approx$20 nΩ.

The ratio of R_{BCS} for Nb at 2.0 K divided by R_{surf} for Cu at 300 K is $\approx 2 \cdot 10^{-6}$. Even when the Carnot efficiency $\eta_C = 0.67\%$, due 2.0 K operation and the technical efficiency of a cryoplant, $\eta_T \approx 20\%$, are included, the reduction in power consumption by using superconducting cavities instead of normal-conducting ones is still quite significant (≈10^3 reduction factor).

The dependence of the penetration depth on the mean free path can be approximated as

$$\lambda \approx \lambda_L \sqrt{1 + \frac{\xi_0}{\ell}} \tag{4-16}$$

and the dependence of R_{BCS} on material purity becomes

$$R_{BCS} \propto \left(1+\frac{\xi_0}{\ell}\right)^{\frac{3}{2}} \ell \tag{4-17}$$

Equation (4-17) shows that $R_{BCS} \propto \ell$ increases with increasing mean free path if $\ell \gg \xi_0$ (the so-called 'clean limit'), and that $R_{BCS} \propto \ell^{-1/2}$ increases with decreasing mean free path if $\ell \ll \xi_0$ (the so-called 'dirty limit'). Therefore $R_{BCS}(\ell)$ has a minimum at $\ell = \xi_0/2$.

4.5 The residual resistance

According to the BCS theory, the surface resistance should fall exponentially with temperature as $e^{-\triangle/k_B T}$. However, measurements at $T < 0.2T_C$ generally show that the surface resistance reaches a residual value. In fact the total surface resistance contains also a temperature independent part, which is called residual resistance R_{res} (4-18). The residual resistance is usually dominated by lattice imperfections, chemical impurities, adsorbed gases and trapped magnetic field. Improvements in the surface preparation of bulk Nb cavities over the past 40 years have reduced the typical residual resistance value from ≈100 nΩ to ≈1−10 nΩ. R_{res} becomes the dominant term in the surface resistance at low frequency (<750 MHz) and low temperatures (<2.1 K), where R_{BCS} becomes exponentially small. There are several possibilities contributing to the residual resistance.

Among those there are:

- losses due to trapped magnetic field,
- losses due to normal-conducting precipitates near the surface,
- grain boundary losses,
- metal/oxide interface losses,
- losses due to normal-conducting electrons in subgap states.

Surface resistance of super conductor is composed of two terms as given below:

$$R_{Surf} = R_{BCS}(T) + R_{res} \tag{4-18}$$

It is experimentally observed that below a certain temperature, surface resistance is higher than the BCS prediction. The additional temperature independent term R_{res} is called as residual surface resistance. The term residual indicates that the causes of losses are often not so clear, because both physical phenomena and accidental mechanism like dust, chemical residuals or surface defects on the cavity walls contribute to the residual [55]. A measurement of the temperature dependence of the low-field surface resistance of bulk Nb at 1.3 GHz is shown in Figure 4.5.

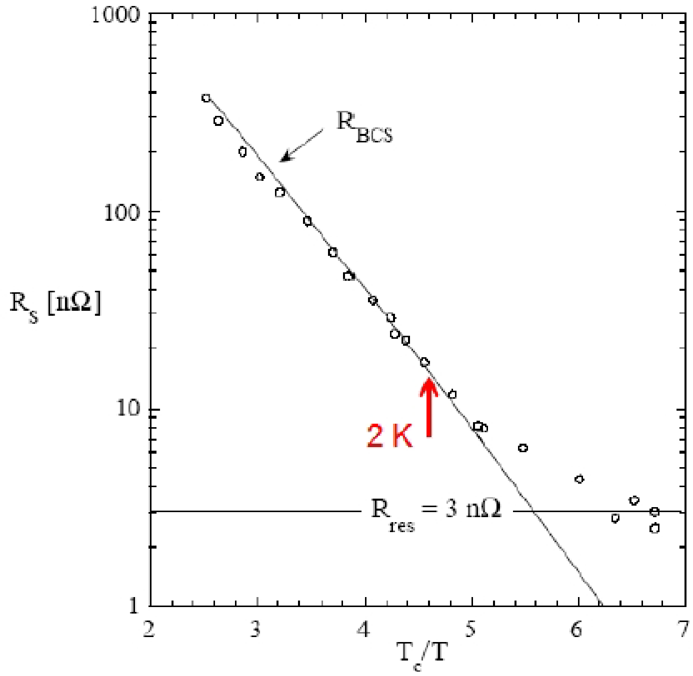

Figure 4.5: The surface resistance of a 9-cell TESLA cavity plotted as a function of T_C/T. The residual resistance of 3 nΩ corresponds to a quality factor of $Q_0 = 10^{11}$. [56]

A well-known contribution to R_{res} is due to trapped DC magnetic field, due to the incomplete Meissner effect in technical materials. Any DC magnetic field at the cavity location can be trapped in the form of fluxoids pinned by defects in the material, as the cavity is cooled below T_c. The losses from fluxons can be calculated:

$$R_{Res,mag} = \frac{H_{ext}}{H_c}\sqrt{\frac{\mu_0 \rho_n \omega}{2g}} \tag{4-19}$$

where H_c is the thermodynamic critical field and g is a parameter related to the anisotropy of the superconductor. In the case of a 1.5 GHz Nb cavity the residual resistance due to the Earth's magnetic field (≈ 0.5 Oe) could be as high as ≈ 600 nΩ, about 30 times higher than R_{BCS} at 2.0 K.

Another well-known contribution to the residual resistance in Nb cavities is due to the precipitation of normal-conducting niobium hydride islands near the surface.

This residual loss (commonly referred to as the "Q-disease") is a subtle effect that depends on the quantity of dissolved H, the rate of cool down to helium temperatures, and the amount of other interstitial impurities or atomic size defects present in the niobium. If the bulk H concentration is greater than $\approx 5\times10^{-4}$ wt.% and if the cool-down rate is <1 $K\cdot min^{-1}$ in the temperature range 75–150 K. This problem can be mitigated by degassing the cavity in an UHV furnace at 600–800 °C for 2–6 h.

4.6 T_c & RRR

4.6.1 T_c

The superconductor shows superconductivity when its temperature is below a certain value, that is, the temperature at which the superconductor transfers to a superconducting state from a normal state. This temperature is called the critical temperature and is denoted by T_c. In general, the superconducting transition usually occurs in a temperature range near T_c, which is called the temperature transition width represented by ΔT_c. In metal or alloy superconductors with high purity, a single crystal and stress free, ΔT_c is smaller than 10^{-3} K.

4.6.2 Residual Resistivity Ratio (RRR)

The Residual Resistivity Ratio (RRR), or also triple-R, is considered a common indicator of purity of the superconductor. The RRR is defined, in fact, in the case of Niobium, as the ratio of the electrical resistivity at two temperatures: 300 K and 4.2 K, see eq. (4-20). The value of RRR indicates, as said before, the purity and the low-temperature thermal conductivity of a material, and is often used as a material specification for superconductors.

$$RRR = \frac{\rho_{300K}}{\rho_{4.2K}} \tag{4-20}$$

High-purity niobium has higher RRR values; the theoretical limit is 35000 and is determined by scattering of electrons by lattice vibration. The standard RRR on Niobium used for cavity production is greater then 300.

4.7 RF superconductor for cavities production

The advantages of superconducting cavities over normal conducting cavities are well known. These advantages can be exploited in many different ways since they permit continuous operation of the accelerator, improve the energetic conversion to the beam, relax the constraints on cavity design and minimize the cavity impedance seen by the beam.

The ideal material for superconducting cavities should exhibit a high critical temperature, a high critical field, and, above all, a low surface resistance. Unfortunately, these requirements can be conflicting and a compromise has to be found. Today, most superconducting cavities for accelerators are made of niobium.

As can be seen from Eq. (4-15), R_{BCS} depends strongly on the superconductor penetration depth and critical temperature. It is thus crucial to:

1) Maximize superconductive transition temperature T_C;
2) minimize the penetration depth, λ;
3) have a large coherence length, ξ.

If we take into account point two (small penetration depth) and three (large coherence length) together, we get the description of a type I superconductor. These are universally known as low T_c superconductors, and this is clearly in contradiction with point one.

The BCS theory, equation (4-2), gives a relationship between the coherence length and the critical temperature. The inverse relationship between the coherence length and the critical temperature indicates that the contradiction between point one and three is very deep indeed. Therefore, the ideal superconductor for RF applications does not exist, and subsequent choices clearly result from a compromise.

4.7.1 Lead

Lead, as an archetype of a type I superconductor, has been used for low frequency cavities, and has yielded a very low residual surface resistance. It is cheap, and easily available in a pure form. Unfortunately, at frequencies higher than a few hundred MHz, the BCS surface resistance becomes prohibitive, due to the low critical temperature of this material. Moreover, it has poor mechanical characteristics and easily oxidizes, with a subsequent degradation of the properties of the superconducting surface. For these reasons, lead tends to be progressively replaced by niobium, and is now confined to low frequency applications.

Type II superconductors can have a large T_c and a reasonably small penetration depth, so that their BCS surface resistance can be small, even at rather high cryogenic temperature. But their coherence length is small, so type II superconductors tend to display rather high residual surface resistance.

4.7.2 Niobium

In view of the above criteria, Nb appears as a serious candidate for superconducting cavities. It has the highest T_c of all pure metals. Being a soft type II superconductor, it occupies a position of compromise between the four requirements mentioned above.

Niobium homogeneity and purity are important issues for RF applications because it determines the thermal stability of the cavity. It was quickly realized that a frequent gradient limitation in superconducting cavities is due to thermal instabilities triggered by microscopic hot spots, for example normal conducting inclusions. For a good thermal stability, a niobium cavity must thus be made from a material with high thermal conductivity.

4.7.3 Niobium thin film

Superconducting cavities internally coated with a thin superconducting film can also be produced. For a complete screening of the RF field by the superconductor, a minimum thickness of 10 times the penetration depth l should be deposited. This corresponds to a thickness ranging between 0.5 and 2 µm and can be achieved by many deposition techniques. Considerable advantages can be expected from such “thin film” cavities:

- a cheap substrate can be used, with a subsequent cavity cost saving;
- a good heat conductor can be chosen for the substrate, giving a good cavity thermal stability;
- materials unavailable in bulk form can be deposited in thin films, with potentially interesting superconducting properties.

These criteria can be met by using copper as the substrate. A number of superconducting materials have been investigated for RF applications. So far, the most successful is niobium, sputter-deposited on a copper substrate deposited DC sputtering.

Nb/Cu cavities provide an appreciable cost saving in supply material. In addition, the RRR of the deposited material is around 30, close to the optimum value which minimizes the BCS contribution to the surface resistance.

4.8 Other potential materials: Nb_3Sn and nitrides

Many superconductors suitable for RF cavity production are investigated in different laboratories around the world. Table 4-1 summarizes the principal candidates.

Table 4-1: Characteristics of various superconductors.

MATERIAL	T_c (K)	λ (NM)	ξ (NM)
Lead	7.2	39	83-92
Niobium	9.2	32-44	30-60
$Nb_{0.6}Ti_{0.4}$	9.8	250-320	4
NbN	15-17	200-350	3-5
Nb_3Sn	18	110-170	3-6
YBCO	94	140	0.2-1.5

4.8.1 Nb_3Sn

Thin films of Nb_3Sn have had more success (accelerating gradients as high as 15 MV/m, cavity Q-value higher than 10^{10} at low fields) [57], but the fabrication method (start from a pure niobium cavity, evaporate tin on its surface, and heat up until Nb3Sn is formed to a few mm thickness) is probably expensive and does not lend itself to an easy industrialization. It might be interesting, however, in cases where cost is not a very important criterion, or to upgrade the performance of existing cavities.

4.8.2 Nb(Ti)N

Deposition of niobium-nitride films could produce cavities with the high critical temperature and lower BCS contribution to the surface resistance; it will permit cavity operation at temperatures higher than 2 K (the goal will be 4.2 K). So far, full success cannot be claimed. However, encouraging results have been obtained on samples, with low surface resistance at low field levels (400 mW at 4 GHz), and a BCS contribution much lower than for niobium (three times less at 4.2 K). Nitride accelerating cavities with competitive characteristics have not been produced yet [58].

Chapter 5

Q-Slope in Nb/Cu Cavities

5.1 Q-Slope in bulk cavities

The Q-drop is a precipitous decrease in cavity quality factor Q (or increase in surface resistance) when exceeding ≈20-30 MV/m average accelerating gradient. The cause of this sudden increase in surface resistance is yet unknown. Absence of electron emission or X-rays implies that field emission is not a major factor in these losses. Temperature array maps of the cavity reveal a global heating as well as local heating spikes all over the equator region (where the magnetic field is highest) in the Q-drop regime.

Some years ago, the Q drop was considered as a typical feature of BCP cavities since the KEK group could show that the electro-polishing process did not give significant problems. The same was shown later in the study of electro-polished cavities, which had also shown Q-drop at DESY, a fact that created confusion as to the claimed superiority of electro-polishing. Later, it was understood that a moderate temperature baking was part of the Japanese electro-polishing procedure. It has to be noted, however, that the baking effect is generally more pronounced in electro-polished cavities, i.e. often a small residual Q-drop remains in the chemically polished (BCP) cavities after baking. But it is necessary to note that Q-drop is not at all unusual. This problem can have many different origins and explanations.

For a bulk cavity, as shown in Figure 5.1 it is necessary to consider three different Q-slopes in the Q_0 vs E_{acc} curve: at low (LF), medium (MF) and high fields (HF).

5.1.1 Low Field Q-slopes

When raising the rf magnetic field from zero, the Q value rises, reaching a maximum near 15–20 mT. The Q rises by about 40% and the maximum is presumably the traditional BCS value. An interesting series of experiments suggests that the low-field Q-slope originates from the metal–oxide layer. On the other hand, V. Palmieri [59] demonstrates that the low field increase of the Q-factor can be mathematically described by the presence of an overlayer made of a poor superconductor originated from the metal–oxide layer.

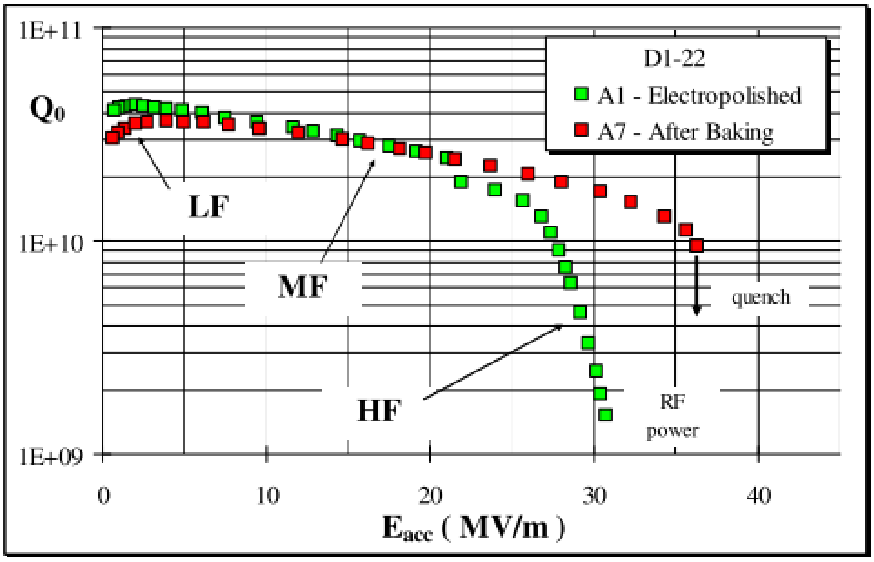

Figure 5.1: Low, medium and high field Q-slopes.

5.1.2 Medium Field Q-slopes

The medium-field Q-slope can be quite strong dropping the Q by a factor of 2–3 from 2 to 25 MV/m, and another factor of 2 out to 40 MV/m. The simplest explanation for the medium-field Q-slope is based on a thermal feedback model with pure BCS resistance. Respect to the Q_0 vs E_{acc} evolution in the medium field range, a linear and a quadratic increases of the surface resistance $R_S \propto 1/Q_0$ on the peak surface magnetic field $B \propto E_{acc}$ have theoretically been established. The linear dependence is linked to hysteresis losses due to Josephson fluxons in weak links (oxidation of grain boundaries). As regards to the quadratic dependence, it is produced by a surface heating due to the thermal impedances of Nb and Nb-He interface.

5.1.3 High Field Q-slopes

An obstacle towards achieving reproducibly high accelerating gradients is represented by anomalous losses, when the peak surface magnetic field is above about 90 mT. Those losses can cause a sharp degradation of the cavity quality factor in the high field region, effect known as “Q drop”, a precipitous decrease in the cavity quality factor when exceeding 20-30 MV/m.

While low field and medium field models successfully explain the Q slope, the cause of this sudden increase in surface resistance at high fields is yet unknown. Several mechanisms have been suggested as possible explanations of this effect, but they cannot explain some of the established experimental facts. Mainly six models trying to explain the Q drop mechanism, somehow in agreement with some experimental fact and in disagreement with others [37].

5.2 Q-Slope in thin film cavities

As discussed in paragraph 4.7.3 at page 60. Nb/Cu cavities are a good candidate for future colliders. The main disadvantage of thin film cavities is the continuous decrease of the quality factor Q_0 versus accelerating field E_{acc}. Figure 5.2 shows a typical Q_0 versus E_{acc} for niobium thin films onto copper cavities. Due to this Q-drop, the highest value experimentally achieved for the accelerating field is 25 MV/m.

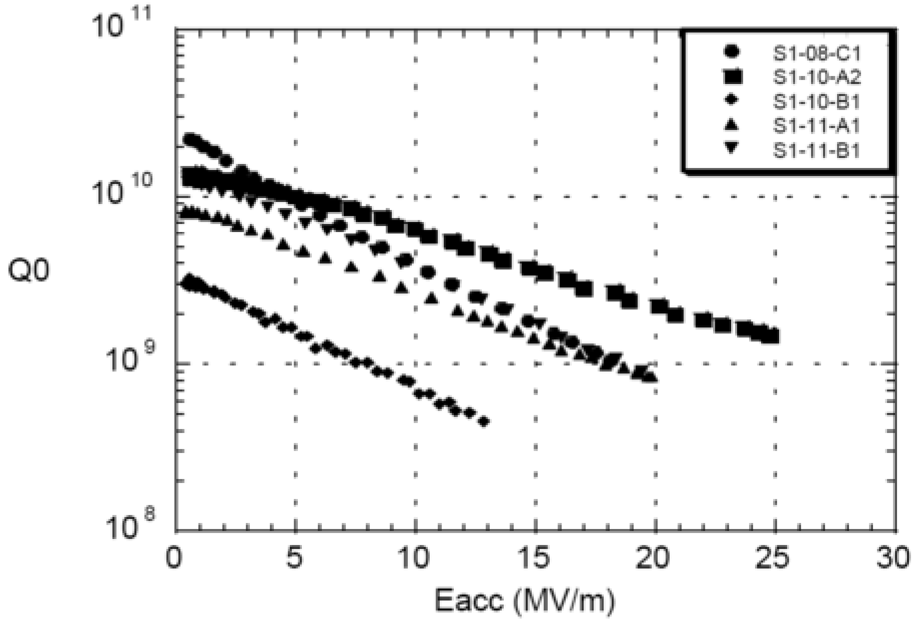

Figure 5.2: Example of typical Q vs E_{acc} @ 1,7 K of 1,5GHz Nb/Cu cavities [60].

However it is possible to get very good performance by the using of the niobium film technology.

Q-slopes also exist in the bulk case, but their origins are probably different. In Figure 5.3, Q_0 vs. E_{acc} curve of the Nb bulk cavity (green data) can be compared to blue data of the thin film cavity. We can notice a softer Q-slope for the bulk cavity at medium accelerating fields and a steeper one above 25 MV/m (high-field Q-slope).

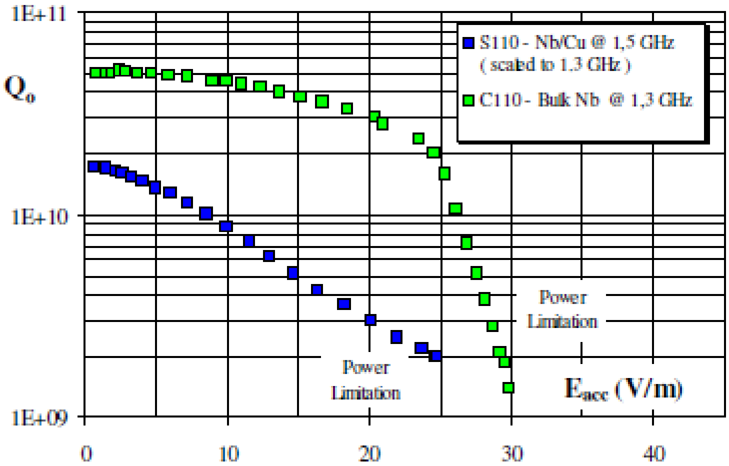

Figure 5.3: Comparison of Q-drops between thin film (blue) and bulk cavities (green).

However, for the niobium bulk cavity, the high field Q-slope can be removed by baking at 120 °C for 2 days and its performances after will be limited by quench (superconducting breakdown).

Probably, a lot of factors will influence the Q-slop in Nb/Cu cavity. In the following paragraph the most evident ones will be summarized.

5.2.1 RRR Niobium thin film

The typical RRR of Niobium thin films is 10–20. The Nb/Cu cavities are also not affected by Q-disease, since no bulk chemistry is necessary, which eliminates the path to H contamination. As discussed in paragraph 4.6.2, RRR is directly connected to thin film purity and the presence of impurities is one of the first candidates that cause Q-slope. A material with a low RRR, for instance, shows higher resistance at low field, stronger Q-slope and earlier onset of Q-drop. The lower the RRR, the stronger the above features. However, there are exceptions to this rule. One example for this was observed in 9.56 GHz cavity that reached a 150 mT peak magnetic field with very little Q-drop, made from a material of RRR≈50. Cavities made from deep drawn polycrystalline sheet material, which have not undergone the initial 100 micron etching to remove the “damage layer”, also show strong Q-slope and early onset of Q-drop [61].

5.2.2 Weak link on grain boundary

Since grain boundaries are “weak” areas in a niobium surface that can easily be contaminated by segregated impurities and form “weak links”, they are a prime candidate for causing a degradation of the performance of the material. The strong Q-slope observed in sputtered Nb on Cu cavities is now believed to be in part the result of 100 times smaller grain-size as compared to bulk Niobium cavities, possibly because of the effect of grain-boundaries on the RF surface resistance. Models used for the description of high-Tc superconductors in which the grain-boundaries are described as weak links, were adapted to the case of RF fields. Such a model was adapted to the case of Niobium by H. Safa and B. Bonin [62]. The most important input parameter in this case is the grain boundary critical current density together with the weak-link lattice parameter.

According to the Granular Superconductor Theory, losses should be linked with the nature of the Niobium coating itself, due to the penetration of Josephson fluxons in weak links: oxidized sputtered islands in this case.

5.2.3 Vortex hotspots on RF surface resistance

Trapped vortices can be produced by any external magnetic field $H > H_{c1}(T)$ upon cooling a superconductor through T_c. Since $H_{c1}(T)$ increases as T decreases, the subsequent cooldown to lower temperatures at which $H \ll H_{c1}(T)$ makes thermodynamically unstable vortices, forcing them to escape through the sample surface. In doing so, a fraction of vortices can get trapped by the materials defects such as non-superconducting precipitates, networks of dislocations or grain boundaries, giving rise to pinned vortex [63].

5.2.4 Energy gap dependence from current

The surface resistance in the superconducting state should be independent of magnetic field. In reality this happens very seldom and the increase of surface resistance versus field could be explained if the energy gap depended on applied magnetic field.

The dependence with the magnetic field of the energy gap Δ(H) could explain the thin film Q-drop, through the low value of the ℓ/ξ_0 key parameter, that is the ratio between the electron mean free path and the coherent length of Cooper pair [59].

5.2.5 Nb/Cu interface and peeling problem

Q-slope could also be related to enhanced thermal boundary resistance $R_{Nb/Cu}$ at the Nb/Cu interface, due to poor thermal contact between film and substrate. A sputtered Nb/Cu thin film cavity can be described as a set of three subsystems:

1) the superconducting niobium film;
2) the copper substrate;
3) the niobium–copper interface.

The Nb/Cu system is considered a classical example for non-miscible systems (Figure 5.4).

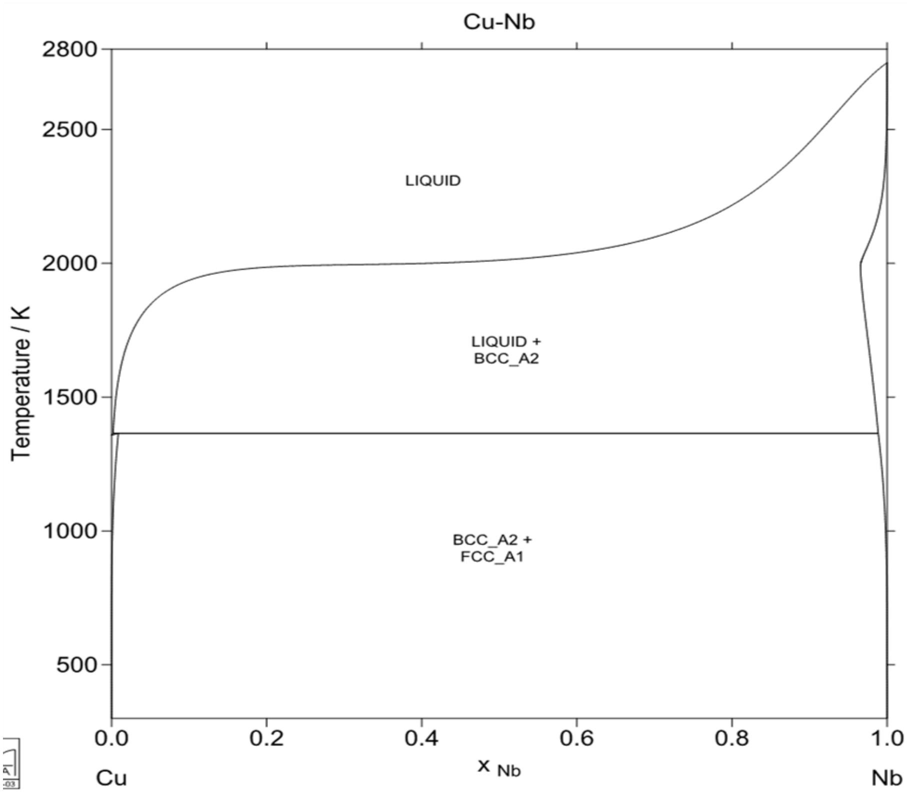

Figure 5.4: The Cu/Nb phase diagram.

In some cases, the Nb film can peel off immediately after the sputtering; in some other cases the Nb film can partially peel off even after many years, due to stress release inside the film. Finally, it is clear that any defect on the Cu substrate is strongly amplified by the film growth and that the adhesion between Nb and Cu, even in the absence of surface defects, is certainly influenced by lattice parameter matching at the crystalline level [64].

The increase of the thermal resistance at the superconductor-substrate interface could also be put forward as an explanation [65].

5.3 Thin film cavities improvement

So far, the ‘Q-slope’ problem has strongly limited the application of niobium thin film sputtered copper cavities in high field accelerators. In the previous paragraphs, have been discussed the probable causes of this degradation. If we want to use thin films technology for future collider, it will be important to minimize q-slope degradation in thin film cavities in order to improve performance. This can be achieved adopting different strategies.

5.3.1 Thin under-layer coating

One possible solution in order to improve Nb/Cu adhesion and to reduce thermal resistance between these two materials, could be the growing, between copper and niobium, a buffer layer of a metal miscible to both materials, for example aluminium, tin, silver or palladium [64]. The under-layer of Palladium gave good preliminary results, on the other hand, Silver did not work and other materials like Tin and Aluminium need to be tested.

5.3.2 High temperature sputtering: induction heating

Increasing the substrate temperature will both decrease the void volume and the mean surface roughness of the nucleating film, by increasing the spacing between void tracks [66].

A high temperature vacuum annealing of the film after the sputtering could also play a role in the recovery of the film morphology and microstructure, especially at the interface, if the temperature is higher than 1073 K.

Chapter 6

Inductive Heating

6.1 Induction heating for 9-cell cavities

As discussed in the previous chapters, the production of Niobium thin films, high *Q* and high filed accelerating cavities is a very complex challenge. The requirements of new colliders are very high energy and high intensity of the beams, so if the accelerator community wants to follow the road for the developments of big facilities like ILC, the R&D on Nb coated Cu cavities is fundamental.

As discussed in Chapter 5, the Q-slope problem of coated cavities has to be solved. Different theories try to explain this physical phenomenon but for sure, the coating at high temperature, annealing of cavities and different heating treatments seems to be a solution for the q-slope problem.

In the past different heating treatments have been developed and used in cavities processing, like IR heating, resistive heating, etc.

One of the most promising is definitely the induction heating. This technique is a non-contact heating process. It uses high frequency electricity to heat electrically conductive materials. Since it is non-contact, the heating process does not contaminate the substrate material. It is also very efficient since the heating is generated inside the workpiece.

6.2 Basic Electromagnetic phenomena in Induction Heating

The basic components of an induction heating system are an induction coil, an alternating current (AC) power supply and the workpiece itself. The coil, which may take different shapes depending on the required heating pattern, is connected to a power supply. The alternating voltage applied to the induction coil will result in an alternating current in the coil circuit. An alternating coil current will produce in its surrounding a time variable magnetic field that has the same frequency as the coil current. This magnetic field induces eddy currents in the workpiece located inside the coil. Eddy currents will also be induced in other electrically conductive objects that are located near the coil. These induced currents have the same frequency as the coil current; however, their direction is opposite to the coil current. These currents produce heat by the Joule effect (I^2R).

Figure 6.1 shows a scheme of a conventional induction apparatus.

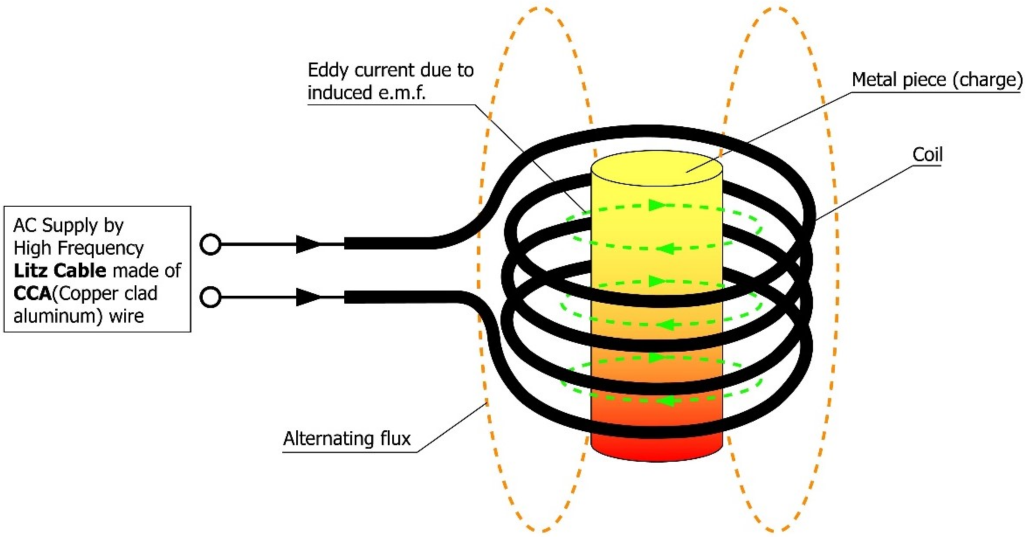

Figure 6.1: Induction system scheme.

Figure 6.2 shows an induction heating system that consists of a cylindrical load surrounded by a multiturn induction coil.

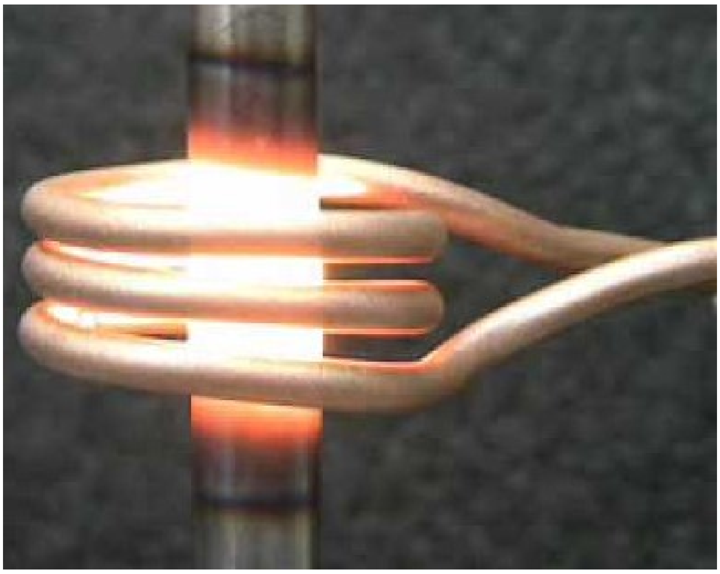

Figure 6.2: Picture of a standard induction coil.

A common analogy used to explain the phenomenon of electromagnetic induction makes use of the transformer effect. A transformer consists of two coils placed in close proximity to each other. When a voltage is impressed across one of the coils, known as the primary winding or simply the "primary," an ac voltage is induced across the other coil, known as the "secondary." In induction heating, the induction coil, which is energized by the ac power supply, serves as the primary, and the workpiece is analogous to the secondary.

Because of several electromagnetic phenomena, the current distribution within an inductor and workpiece is not uniform. This beat source non-uniformity causes a non-uniform temperature profile in the workpiece. Several electromagnetic phenomena, in fact, cause a non-uniform current distribution; these phenomena include:

1) skin effect,
2) proximity effect,
3) ring effect.

These effects play an important role in understanding the induction heating phenomena [67].

6.2.1 Electromagnetic Properties of Metals

Electromagnetic properties of materials is quite a broad expression that refers to a number of electromagnetic characteristics. Below, we will consider the properties with the most pronounced effect on parameters of the induction heating systems.

6.2.1.1 Electrical Resistivity (Electrical Conductivity)

The ability of material to easily conduct electric current is specified by electrical conductivity σ. The reciprocal of the conductivity σ is electrical resistivity ρ. Electrical resistivity of a particular metal varies with temperature, chemical composition, metal microstructure and grain size. For most metals, ρ rises with temperature and can be expressed as a linear function of it:

$$\rho(T) = \rho_0[1 + \alpha(T - T_0)] \tag{6-1}$$

where ρ_o is the resistivity at ambient temperature T_0 ; $\rho(T)$ is the resistivity at temperature T; α is the temperature coefficient of the electrical resistivity.

The value of electrical resistivity is also affected by the grain size (e.g., higher ρ corresponds to finer grains), plastic deformation, heat treatment and some other factors, but to a smaller extent compared to the effect of temperature and chemical composition.

6.2.1.2 Magnetic permeability and relative permittivity (dielectric constant)

Relative magnetic permeability μ_r indicates the ability of a material to conduct the magnetic flux better than vacuum or air. Relative permittivity (or dielectric constant) ε indicates the ability of a material to conduct the electric field better than vacuum or air.

Relative magnetic permeability has a marked effect on all basic induction phenomena, including the skin effect, electromagnetic edge and end effect, as well as proximity and ring effects. Relative permittivity is not as widely used in induction heating, but it plays a major role in dielectric heating applications.

The product of relative magnetic permeability and permeability of the free space is called permeability, μ, and corresponds to the ratio of the magnetic flux density (B) to magnetic field intensity *(H)*.

$$\frac{B}{H} = \mu_0 \mu_r \tag{6-2}$$

Often the relative magnetic permeability is called simply magnetic permeability. The relative magnetic permeability is closely related to magnetic susceptibility by the expression:

$$\mu_r = \chi + 1 \tag{6-3}$$

All materials based on their magnetization ability can be divided into paramagnetic, diamagnetic, and ferromagnetic. Relative magnetic permeability of paramagnetic materials is slightly greater than 1 ($\mu_r > 1$). The value of μ, for diamagnetic materials is slightly less than 1 ($\mu_r < 1$). Due to insignificant differences of μ, for both paramagnetic and diamagnetic materials, in induction heating practice, those materials are simply called nonmagnetic materials. Typical nonmagnetic metals are aluminium, copper, titanium, tungsten, among others. In contrast to paramagnetic and diamagnetic materials, ferromagnetic materials exhibit the high value of relative magnetic permeability ($\mu_r \gg 1$) [68].

6.2.2 Skin Effect

As one may know from the basics of electricity, when a direct current flows through a conductor that stands alone (bus bar or cable), the current distribution within the conductor's cross-section is uniform. The maximum value of the current density will always be located on the surface of the conductor; the current density will decrease from the surface of the conductor toward its centre. This phenomenon of non-uniform current distribution within the conductor cross-section is called the skin effect, which always occurs when there is an alternating current and was widely discussed in chapter 4.2 at page 54.

The skin effect is of great practical importance in electrical applications using alternate current. Because of this effect, approximately 86% of the power will be concentrated in the surface layer of the conductor. This layer is called the penetration depth δ, and it is defined as the distance that the field has to traverse so that its magnitude reduce to $1/e$ of its source value.

$$|E_z| = E_0 e^{-\frac{y}{\delta}} \tag{6-4}$$

The degree of skin effect depends on the frequency and material properties (electrical resistivity ρ and relative magnetic permeability μ_r) of the conductor, as discussed in paragraph 4.2 (page 54):

$$\delta = \sqrt{\frac{2\rho}{\mu\omega}} \tag{6-5}$$

The surface resistance can be expressed as:

$$R_{surf} = \frac{1}{\sigma\delta} = \frac{\rho}{\delta} \tag{6-6}$$

There will be a pronounced skin effect when high frequency is applied or when the radius of the workpiece is relatively large (Figure 6.3).

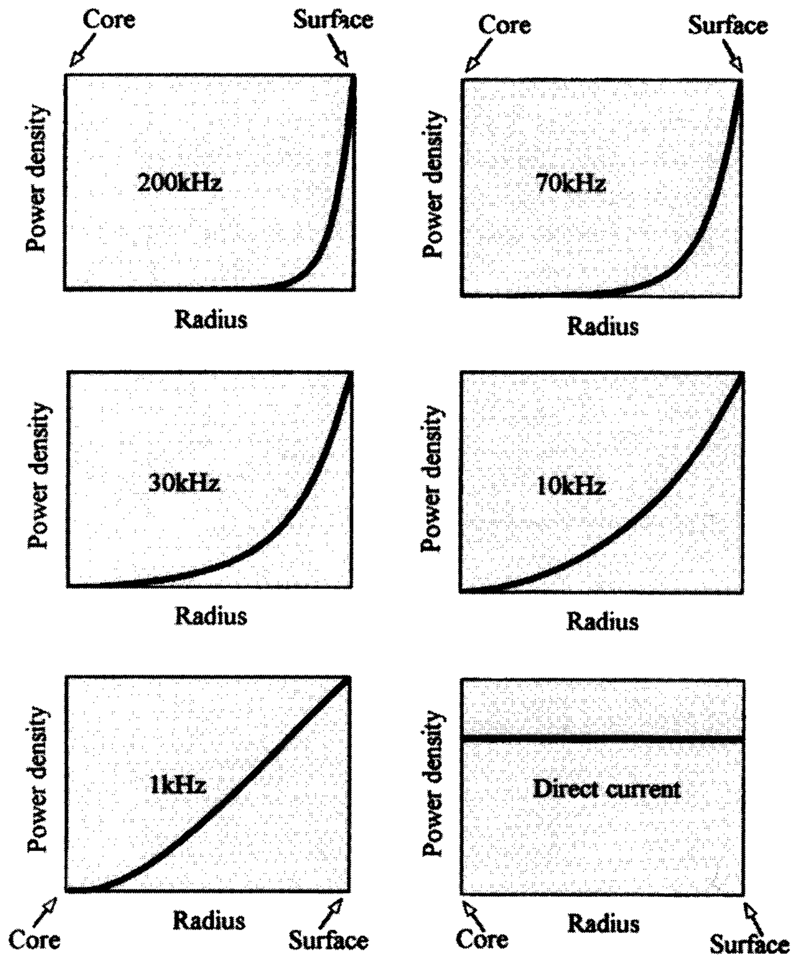

Figure 6.3: Power density distribution along the radius of a stainless steel cylinder [68].

By the following equation, it is possible to calculate also the distribution of the current density along the workpiece thickness (radius):

$$I = I_0 e^{-\frac{y}{\delta}} \tag{6-7}$$

where *I* is current density at distance *y* from the surface.

We can define a power penetration depth D_p at which the power density drops to $1/e$ of its value at the surface. This gives:

$$P = P_0 e^{-\frac{y}{D_p}} \tag{6-8}$$

Where

$$D_p = \frac{1}{2\alpha} = \frac{\delta}{2} \tag{6-9}$$

It is important therefore to differentiate between power penetration depth and electric field or skin depth as shown in Figure 6.4. The penetration depths are generally rather small and the size of the dielectric to be treated could be many times larger than D_p, which may result in unacceptable levels of temperature non-uniformity.

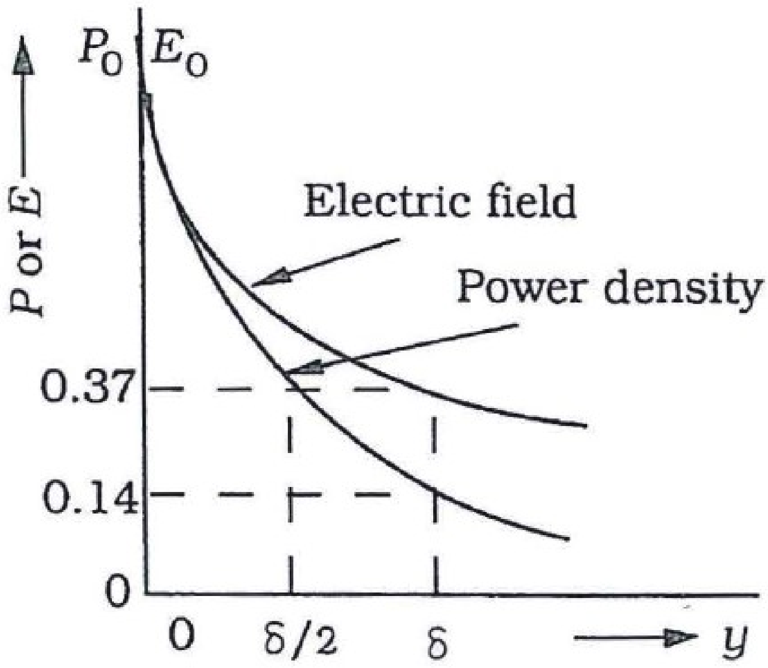

Figure 6.4: Skin and power penetration depths [69].

Analysis of Eq. (4-12) shows that the penetration depth has different values for different materials and is a function of frequency. The electrical resistivity of metals ρ is a function of temperature. During the heating cycle, ρ of most metals can increase to four to five times its initial value, indeed $\rho \propto T$ if $T < \Theta_D$ (with Θ_D Debye Temperature), and as $\rho \propto T^5$ at $T > \Theta_D$. Therefore, even for nonmagnetic metals, during the heating cycle the penetration depth can increase significantly (see Appendix A). In particular, in a copper cavity, the penetration depth almost double from 20 to 500 °C, and triples to 900 °C.

6.2.3 Skin effect in thick and thin body

When discussing the skin effect it is proper to introduce the terms of electromagnetically thick and electromagnetically thin bodies [70], of fundamental importance in our case, because copper cavities has a thin 3 mm wall.

Depending upon the chosen frequency and magnetic field orientation any body can be considered from the electromagnetic point of view as a thick body or thin body. If a current penetration depth is greater compared to the thickness or diameter of the solid body, then it is considered as electromagnetically thin body. There is a distinct current cancellation within the electromagnetically thin bodies and, therefore, only a negligible amount of energy will be absorbed by it. Being transparent to the external electromagnetic field, there will be only small amounts of the Joule effect appearing in electromagnetically thin bodies.

If the thickness or diameter of the solid electrically conductive body is six times the current penetration depth, then it can be considered as an electromagnetically thick body. Since current penetration depth can increase more than 15 times during the heating cycle, the workpiece that initially could be considered as an electromagnetically thick body can become at the end of the heating cycle an electromagnetically thin body.

6.3 Basic Thermal phenomena in induction heating

6.3.1 Thermal Conductivity

Thermal conductivity *k* designates the rate at which heat travels across a thermally conductive workpiece. A material with a high *k* value will conduct heat faster than a material with a low *k*.

If we want to obtain a uniform temperature, a higher thermal conductivity of metal is preferable. In our case, Copper is one of the best material in order to obtain a good temperature uniformity along all the cavity length.

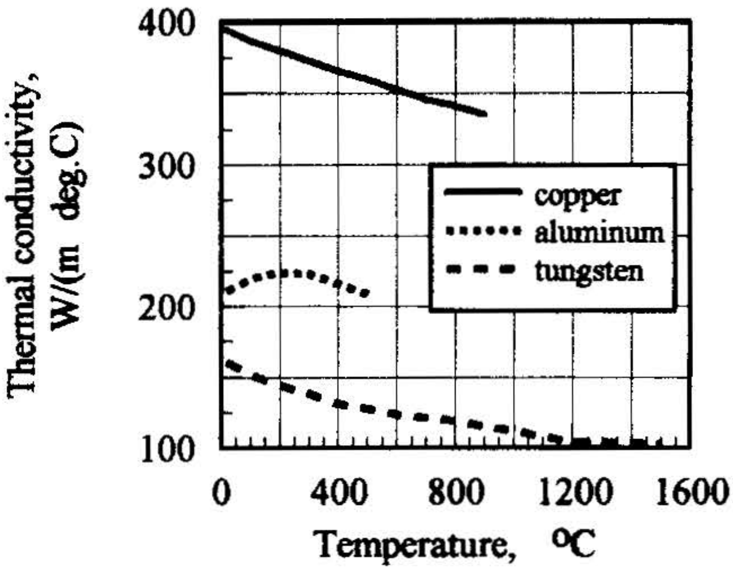

Figure 6.5: Thermal conductivities for some commonly used metals versus temperature [68].

Figure 6.5 shows the values of the thermal conductivity of some commonly used metals. As one may note, the thermal conductivity is a nonlinear function of temperature.

6.3.2 Heat Capacity and Specific Heat

The value of heat capacity *C* indicates the amount of energy that would have to be absorbed by the workpiece to achieve a unit of required temperature change:

$$C = \frac{dQ}{dT} \tag{6-10}$$

where *dQ* is the required energy and *dT* is the required temperature change.

Heat capacity is closely related to a parameter called specific heat *c*, which represents the heat capacity per unit mass meaning the amount of the required heat energy to be absorbed, by a unit mass of the workpiece to achieve a unit temperature increase. A high value of specific heat corresponds to a high-required power to heat a unit mass to a unit temperature. Figure 6.6 shows the values of the specific heat of some commonly used metals [68].

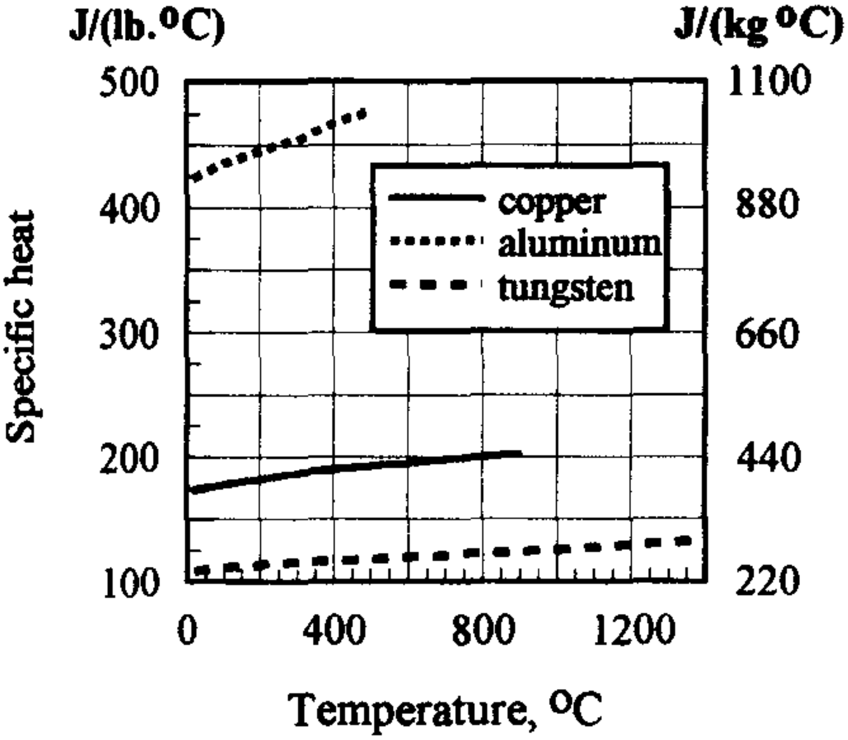

Figure 6.6: Specific heat for some commonly used metals versus temperature [68].

6.4 Three Modes of Heat Transfer

In induction heating, all three modes of heat transfer, conduction, convection, and radiation, are present.

6.4.1 Convection Mode

In contrast to conduction, heat transfer by convection is carried out by fluid, gas, or air (i.e., from the surface of the heated workpiece to the ambient area).

The wellknown Newton's law can describe convection heat transfer. This law states that the heat transfer rate is directly proportional to the temperature difference between the workpiece surface and the ambient area,

$$q_{conv} = \alpha(T_s - T_a) \tag{6-11}$$

where q_{conv} is heat flux density by convection, α is the convection surface heat transfer coefficient, T_s is surface temperature; and T_a is ambient temperature.

α is primarily a function of the thermal properties of the workpiece, the thermal properties of the surrounding fluids, gas or air, and their viscosity or the velocity of the heat-treated workpiece.

In our application, also convection mode is negligible because the treated piece is located in vacuum environment and we do not have exchange gas.

6.4.2 Thermal Conduction

Heat is transferred by conduction from the high-temperature regions of the workpiece toward the low-temperature regions. The basic law that describes heat transfer by conduction is Fourier's law:

$$q_{cond} = -k\nabla \mathrm{T} \tag{6-12}$$

where q_{cond} is heat flux by conduction, k is thermal conductivity, and T is temperature.

This heat transfer mode is negligible in our application because the inductor is larger than the copper cavity and all piece is heated at the same time, furthermore the cavity wall is very thin compared to the penetration depth.

6.4.3 Radiation Mode

In the third mode of heat transfer, irradiation, the heat may be transferred from the hot workpiece into surrounding areas including a nonmaterial region (vacuum). The effect of heat transfer by radiation can be introduced as a phenomenon of electromagnetic energy propagation due to a temperature difference. This phenomenon is governed by the Stefan-Boltzmann law of thermal radiation, which states that the heat transfer rate by radiation is proportional to a radiation loss coefficient C_s and the value of $T_s^4 - T_a^4$. The radiation heat loss coefficient can be determined approximately as $C_s = \sigma_s \varepsilon$, where ε is the emissivity of the metal and σ_s is the Stefan-Boltzmann constant.

Figure 6.7 shows radiation loss density as a function of temperature and ε. Similar to convection losses, there is a formula that provides a rough engineering estimate of the free radiation losses q_{rad}

$$q_{rad} = 5.67 \cdot 10^{-8} \varepsilon (T_s^4 - T_a^4) \tag{6-13}$$

Since radiation losses are proportional to the fourth power of temperature, these losses are a significant part of the total heat losses in high-temperature applications or vacuum application like in our case.

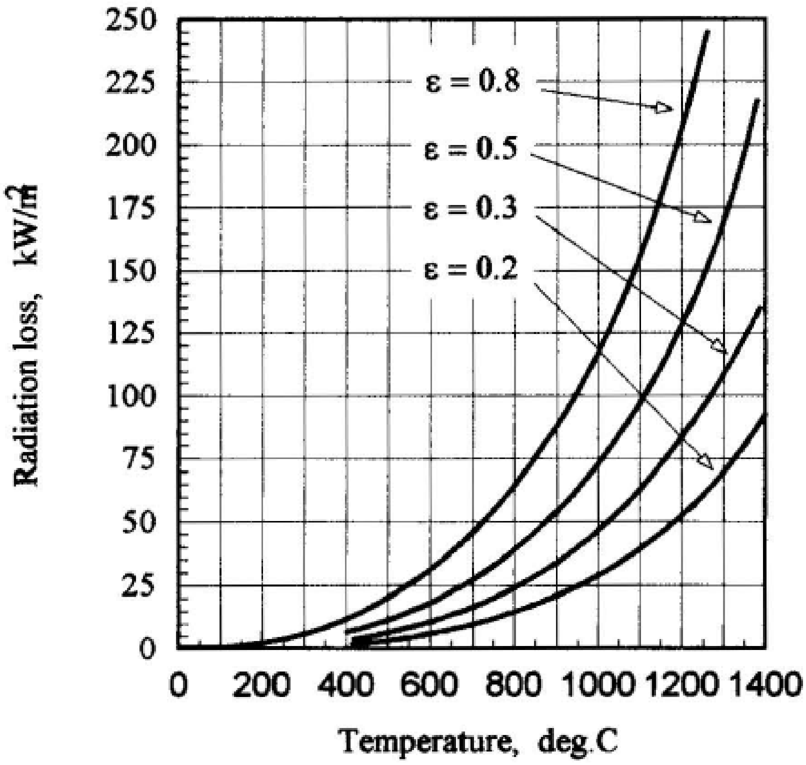

Figure 6.7: Variation of the radiation loss density versus temperature and emissivity [68].

6.5 Estimation of required power for 9-cell Cu heating

Since the value of specific heat *c* represents the amount of the required heat energy to be absorbed by a unit mass of the workpiece, an average value of specific heat *c* can be effectively used for a ballpark estimate of the required workpiece power (P_w) to heat a given shape workpiece to an average temperature. We can use this formula:

$$P_w = \mathrm{mc}\frac{\left(T_f - T_{in}\right)}{t} \tag{6-14}$$

In our case the mass m of the copper cavity is ≈25 kg, *c* is the average value of specific heat ≈420 J/(Kg·K) for Copper, T_f is 780K so we can estimate applying (6-14) for a time of 120 s:

$$P_w = 52.5\ \mathrm{kW} \tag{6-15}$$

If we assume that all the energy is dissipate by radiation mode, because our furnace is in vacuum, so we do not have convection and thermal conduction, we can establish that the power that we need to maintain the cavity at 780 K is proportional to emissivity, see eq. (6-13), and we have in first approximation:

$$\begin{aligned} P_{rad}(\varepsilon, 0.1) &= 2.05\ \ \mathrm{kW}/m^2 \\ P_{rad}(\varepsilon, 0.2) &= 4.11\ \ \mathrm{kW}/m^2 \end{aligned} \tag{6-16}$$

The external surface of 9-cell cavities is approximately 1 square meter (0.95 m^2).

6.6 Inductive Heating facility @ LNL

In order to process Copper and Niobium cavity with vacuum annealing and to coat Copper cavity at high temperature, to promote thin film quality and adhesion as discussed in chapter 5.3 (at page 69), LNL Laboratory commissioned a vertical induction furnace. The company Tecno-Induzione, therefore, developed this furnace in close collaboration with the service of Material Science and Technologies for Nuclear Physics at LNL. The facility is able to treat cavities up to nine cells for a total length of 1300 mm in a vertical solution.

As it will be described in the following chapters, an Ultra High Vacuum system is joined to the furnace to allow the treatments of components in absence of air and oxygen.

The induction heating facility can deliver a power of 120 kW, sufficient to heat a nine cells copper cavity until 800K in less than a minute.

6.6.1 Induction facility description

Figure 6.8 shows the induction facility installed at Legnaro laboratory. On the left, it is possible to see the water-cooled copper inductor; while, on the right, the electronic housing is placed. The coil is surrounded by an Item® frame where a wire mesh will be fixed in order to shield the electromagnetic field generated by the coil.

Figure 6.8: Induction Facility @ LNL. On the left the copper inductor.

Figure 6.9 shows a particular of the copper inductor: 28 spires compose it. The height is approximatively 1500 mm and the diameter is 300 mm. Inside the inductor will it be housed the 9-cell cavity. Between the cavity and the inductor there will be a vacuum chamber; in this region a quartz tube will be used due to it characteristics of transparency at electromagnetic field generated by the inductor.

Figure 6.9: Particular of copper inductor.

The facility needs 400 Vac at 50 Hz and 140 kVA power. For its operation, a specific electric panel has been prepared in order to support the high power requirements necessary for plant operations.

6.6.2 Control Panel

The operation of the inductor heating is quite simple. Turning on the main switch placed on the main panel (Figure 6.10), the operating unit automatically get started. The generator software control consists of different pages, described in this paragraph; in which the operator can set the machine parameters acting through the touch screen panel (Figure 6.11).

Figure 6.10: Main panel of inductor heating system.

After selecting the process parameters, acting on touch screen, pressing the "heating" switch located at the right side of the main panel (Figure 6.10), the heating process starts.

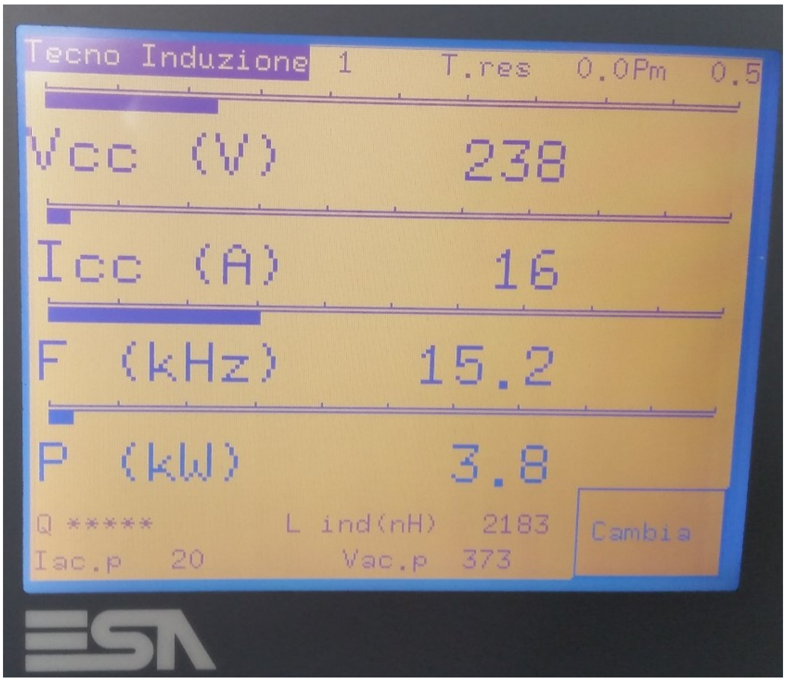

Figure 6.11: Main Page of induction system during operation.

The main page of the touch screen reports generator operation data like:

- V_{cc} indicates DC Voltage,
- I_{cc} indicates direct current,
- *F* indicates operating frequency,
- *P* indicates power output,
- *Q* indicates figure of merit,
- L_{ind} indicates value of the inductance,
- $I_{ac.p}$ and $V_{ac.p}$ indicate peak values of V_{cc} and I_{cc}.

On the upper part of the screen page respectively shows T_{res} and P_m time remaining and the manual set power (Figure 6.12).

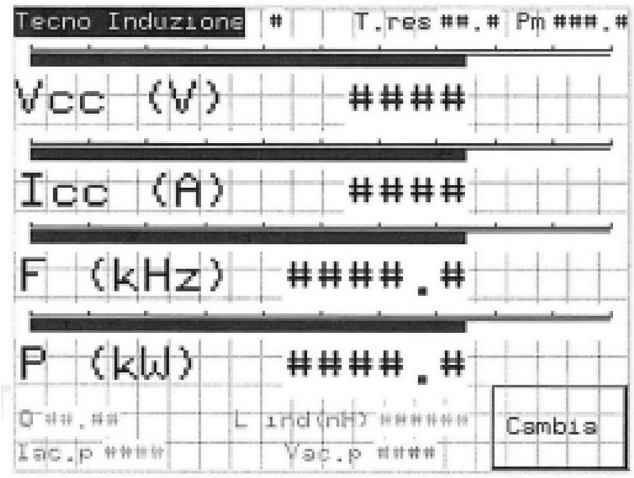

Figure 6.12: Scheme of touch screen main page with operating parameters.

Acting on "change" button it is possible to move on the software page where it is possible to modify the machine setting.

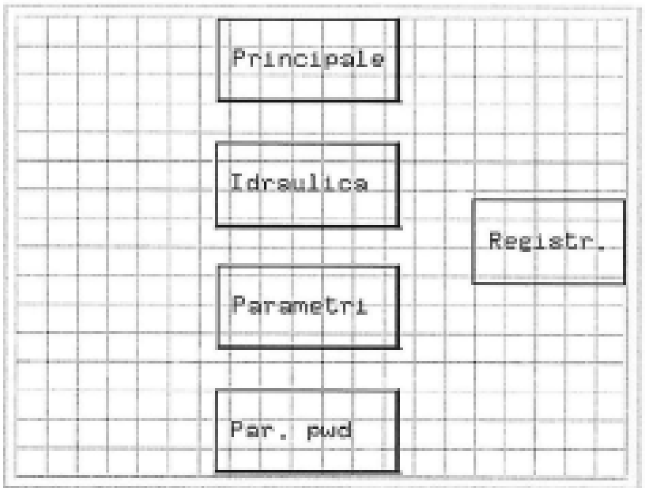

Figure 6.13: Setting main page.

On this page, there are five buttons:

- Main: to return to main page where operation data are shown;
- Hydraulics: to check the control page of water-cooling circuit. It is possible to check if flux meters are OK.
- Parameters: from this page it is possible to set heating parameters.
- Cycle: used to set a heating cycle.
- Par. Pwd is used for maintenance of the system

The windows “Parameters” is used to set different parameters (Figure 6.14).

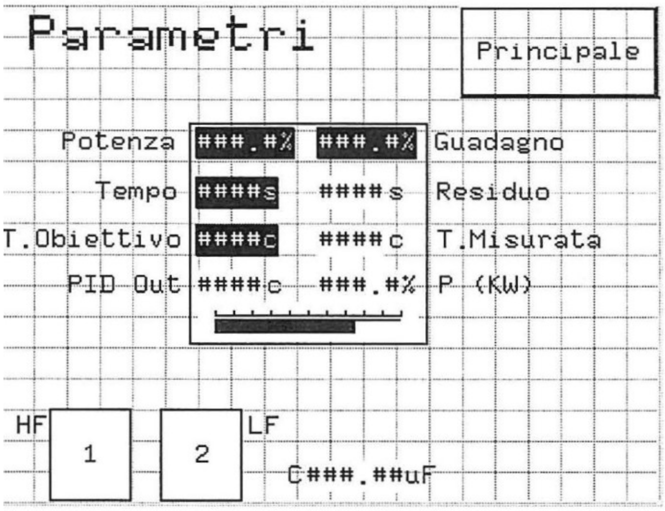

Figure 6.14: Parameters main page.

This page allows to perform the heating in temperature control mode.

Power is used to set the maximum power output of the apparatus, time or temperature are used to set the process time or the temperature of the process. To operate in temperature mode it is mandatory that the pyrometer is connected and set correctly. The tab gain is used to set the reactivity of the apparatus: high gain equals less constant temperature.

6.6.3 Installation and commissioning of inductive furnace

The furnace delivery has required some time. The apparatus, indeed, is not a standard industrial machine, but a prototype able to heat big structures with a complex shape such as elliptical cavities. Our request were mainly focused on: a uniform heating along copper cavity with an error of $\pm 10\ °C$, the possibility to reach 900 °C, the opportunity to make heating cycle and to control the process in time or temperature.

To obtain a facility able to satisfy our requirements we have worked in synergy with the supplier. Being the realization of the system particularly complicated and complex, the delivery of the furnace has had two years of delay.

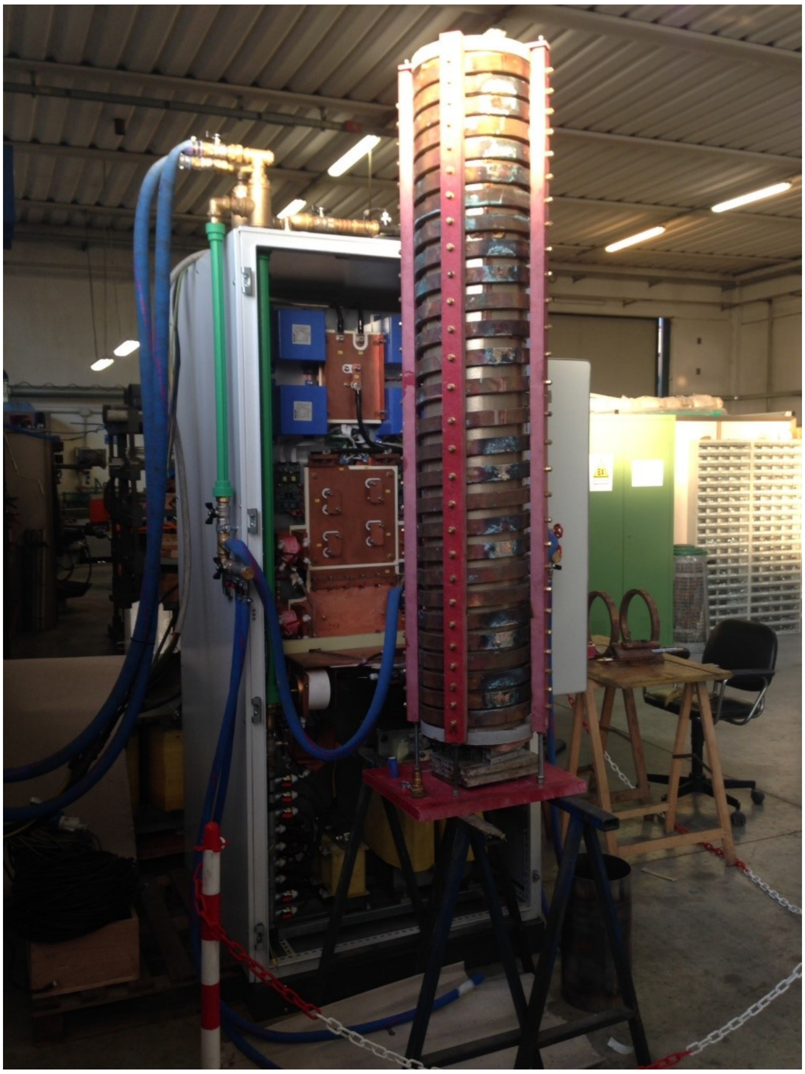

Figure 6.15: Picture of induction system during test at TecnoInduzione. It is possible to see, after the inductor, the deliver power apparatus open during the tuning of the technician.

The request to be able to reach such high temperatures, indeed, has created lots of difficulties on the design; also, the calibration of the inductances and capacitors has required many months of tests because of the particular shape of the cavity. Finally, the delivery was delayed by the supplier of the chiller too; the apparatus, indeed, has required a cooling system greater than that initially established. The final cooling system is of 130 kW.

Unfortunately, some delays occurred even after the delivery of the heating apparatus at LNL laboratory. In fact, the commissioning of the electrical and hydraulic plant necessary for the machine operation have required several month for installation.

Moreover, during commissioning at LNL, made by the supplier, we found different problems on the facility like:

- temperature reading anomaly of the pyrometer due to software problem,
- Different PLC software bugs
- Water leaks on the big external inductor (Figure 6.9).

In particular, this last problem obliged us to dismount the inductor and send it back the supplier, waiting for the fixing.

6.7 Temperature monitor

In order to monitor and control the heating process, a pyrometer was installed. This apparatus is directly connected to the inductor heating PLC; in this way, the heating parameters can be set directly from the PLC display. The pyrometer is a PYROSPOT DG 10N produced by Dias Infra red system. It measures the infrared radiation emitted by the cavity; the measured temperature is displayed on the detector through a small LCD, and also transferred in an electrical signal. This signal is digitally processed and transferred in the standard temperature linear signal of 0-20 mA, which could be easily read by the heater PLC. The Pyrospot DG 10N has a temperature range from 250 to 1300 °C and a spot size from 2.5 mm, at of 250 mm distance, to 40 mm, at 4000 mm distance.

The instrument has also an integrated targeting laser, which enables to focus the measuring object exactly.

Figure 6.16: Picture of induction system during commissioning test at LNL after delivery. On the central part of inductor is visible an Iron tube heated at 700 °C during commissioning.

Chapter 7

Vacuum System

7.1 Ultra High Vacuum system

In order to deposit a good superconductive Niobium thin film, a high vacuum system is required. For this reason, we built a vacuum chamber taking into account the 9-cell elliptical cavity dimension and the inductive furnace dimension, maintaining the highest standards of design. During the designing, the choice of materials, used in construction of the UHV system, was studied with attention, ensuring both high standards of vacuum (lower degassing rates) and the resistance to high temperatures. In this chapter, the main parts of the vacuum system used to carry out the deposition of the thin film will be presented. The vacuum system consist of three main parts: the sputtering cathode, the vacuum apparatus and the process chamber. All these elements will be presented below.

7.2 Vacuum system layout and 3D design

The layout of the vacuum system is given in Figure 7.1. The design was made using Solidworks®, a 3D CAD software. Figure 7.2 shows a rendering of the vacuum system, while Figure 7.5 shows a picture of the system assembled.

The system is described starting from the exit pipe and it is made up of a dry scroll IDP-15 pump produced by Agilent. That pump reaches the maximum vacuum of $1 \cdot 10^{-2}$ mbar with a pumping speed of 12.8 m^3h^{-1}. The scroll pumps are lubricant free pump, an optimal characteristic for the vacuum system designed for Nb coating. The scroll pump is closed by an electropneumatic valve, V1. It opens automatically when the scroll pump is switched-on and closes with the switching off. Electropneumatic V1 valve is designed to prevent backstreaming problem, although, in this case, all the systems are oil free. However, this configuration prevents air reflux from the low vacuum towards the ultra-high vacuum region. Before arriving to the TMP pump, a T connection is placed with a manual VAT angle valve, V2 that could be used to connect a leak detector. A hydroformed flexible bellow connects this low vacuum zone with the TMP. The rotor on the turbomolecular pump, Edwards STP301, makes use of magnetic levitation. Thus, it does not use any oil or grease on the bearing. The pumping speed is 300 ls^{-1} for N_2 at 48000 rpm. The control for the pump system is relatively simple but it does not include an automatic reduction of the pumping speed (Stand-by), mandatory for the sputtering process because it works at 10^{-3} mbar Argon pressure. This inconvenience has been overcome by installing a three-position VAT pendulum valve series 161 (V3). Thus, it permits working in the chamber at pressure of 10^{-3}-10^{-1} mbar during the sputtering stage, keeping the pump at the maximum pumping speed, without damaging it.

Directly after the pendulum valve a cross is installed. The pressure gauges and gas inlet are directly connected on this cross, close to the TMP pump and distant from the vacuum chamber in order to guarantee pressure uniformity and reduce pressure gradient during the process. The pressure gauge installed are the following:

1) Bayart-Alpert PBR 260 (10^{3}-10^{-4} mbar)
2) Pirani (included in BA gauge)
3) Capacitive Gauge CMR 364 Pfeiffer (1.1-10^{-4} mbar)

Two gas lines arrive to the system through the cross: nitrogen for the venting and pure argon for the sputtering. The nitrogen, whose pressure is controlled through a pressure regulator at double stage, enters, through V4 back to the TMP for venting the area behind the gate valve, and through V5 for venting the chamber. The argon N60 (purity 99,9999%) is "stocked" in a 5 liters cylinder fixed close to the system. The connection between the cylinder and the line uses a Cajon fixing system, followed by an all-metal angled valve (V7) and by a leak valve (V8). During pumping and baking, the leak valve always remains opened while the all metal valve that precedes it, is opened only during the sputtering process. To place a precision valve to regulate the flux of argon at the base of the chamber means that the most part of the gas is immediately pumped and only a little fraction of gas lows through the chamber. In this way, the pressure in the chamber is more stable and, moreover, the film contamination, due to the gas impurities, is reduced.

Next, just before the process chamber, it is installed the Polycold trap (for detail see paragraph 7.3.1). After the Polycold system is placed the process chamber which consists of a quartz tube (7.4).

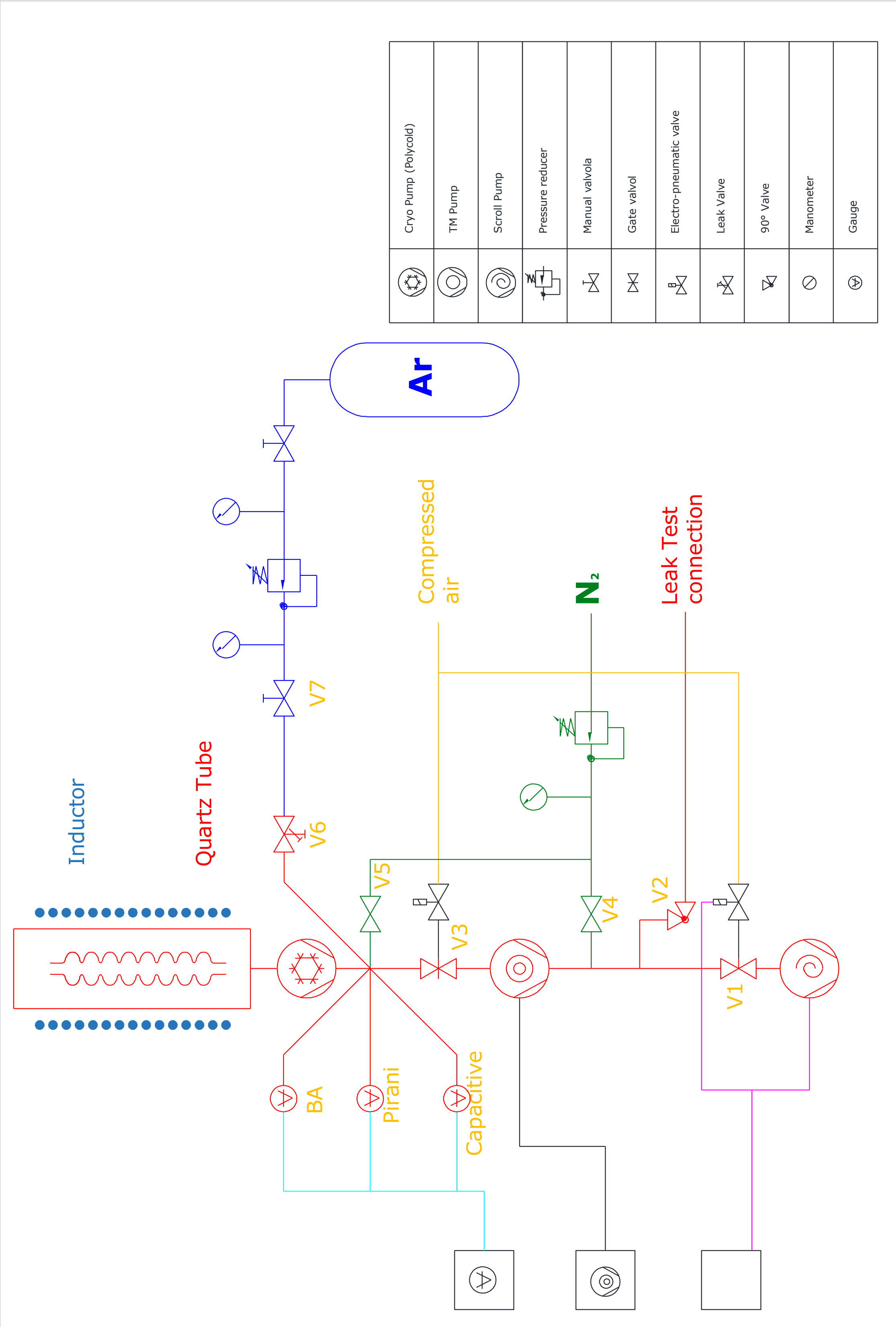

Figure 7.1: Vacuum system layout.

After the layout designm the system was completely drawn and simulated using Solidworks®. Figure 7.2 shows a complete rendering of it. Using a 3D software allowed us to dimension the components and design the whole mechanical and system structure.

Figure 7.2: Rendering of UHV system.

From 3D design, 2D engineering drawing of components were produced and different mechanical workshops machined non-standard components such as flanges and crosses. On some critical component (like quartz tube) FEM simulation were made in order to guarantee mechanical stability and safety for the end users.

After the design of the vacuum system, the support frame was planned in ITEM profiles. It is surrounded by a wire mesh in order to protect the end user by possible damages of quartz tube and, at the same time, for shielding the electromagnetic field generated by the loop.

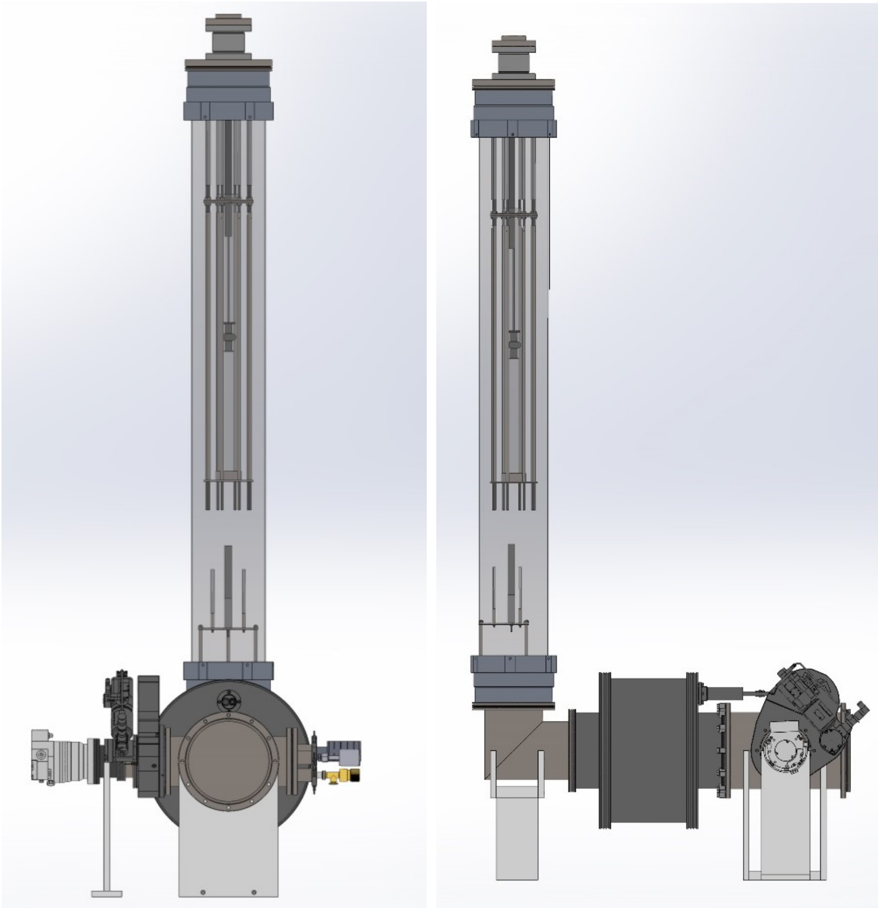

Figure 7.3: On the left front view of the vacuum system, on the right, left view of vacuum system.

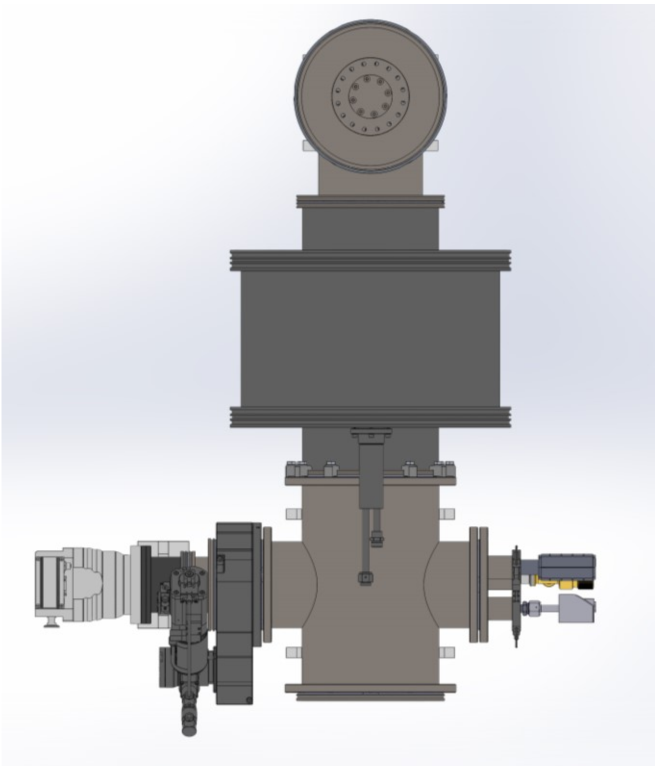

Figure 7.4: Top view of the vacuum system.

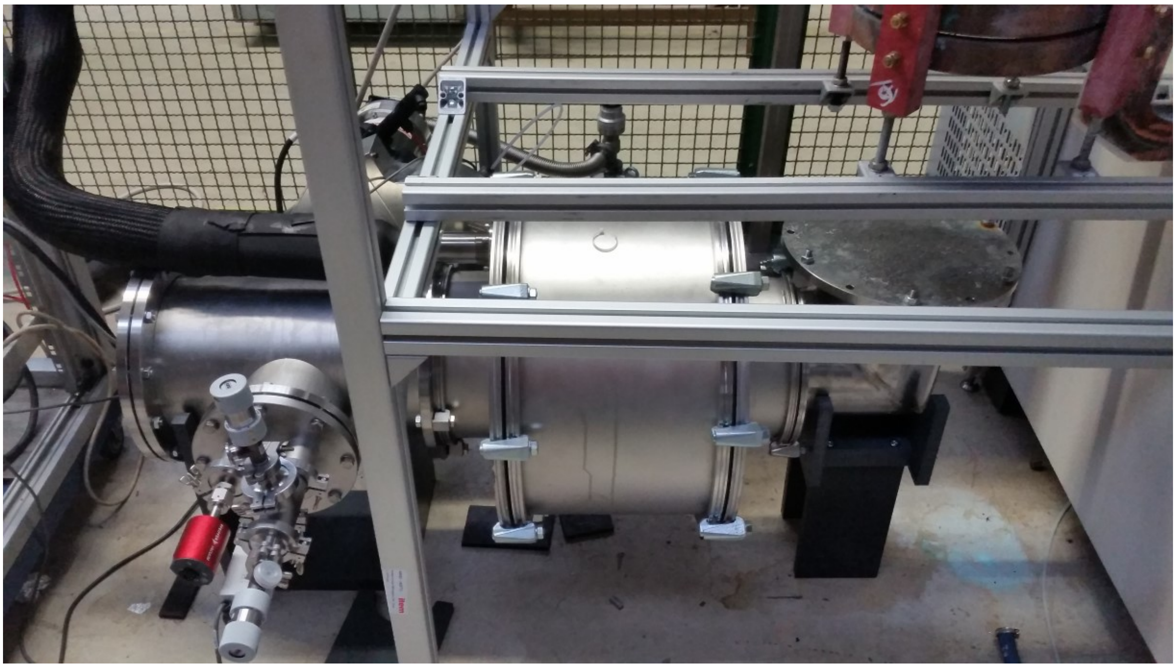

Figure 7.5: Vacuum System assembled.

7.3 Vacuum components

Paragraph 7.2 described the layout and design of vacuum system and of the facility. The choice of components was entirely based on standard and readily available materials.

The vacuum flanges are standard ISO-K/ISO-F for big diameters (up to 100 mm) and ISO KF the small ones. Only the TM Pump is flanged with CF 100. The choice of the seals did not fall on Conflat standard because of the large dimension of the vacuum chamber and connection (200 and 250 mm ID). The material used for the vacuum chamber are all compatible with UHV environment. The chamber is made of Stainless Steel 316 L or Aluminium; the sealing are on copper or Viton® and the process chamber is made of quartz.

Particular attention was made on the design and choice of materials in the region close to the inductor. It has been chosen to produce the cavity and source supports in SS 316L since it is non-magnetic stainless steel and quite resistant to high temperature.

Power feedthrough are ceramic brazed onto SS able to power the magnetron source with high current and to power cavity bias.

The choice of the pumping system has been made with accuracy in order to avoid any contamination with oil, the system is entirely grease and oil free.

7.3.1 Polycold system

In series to the TM pump, close to the quartz vacuum chamber, is installed a Polycold Fast Cycle (PFC) trap, a water vapour Cryopump.

The PFC is a cryogenic refrigeration system that captures volatile molecules by freezing them onto a cold surface. The PFC consists of a refrigeration unit (Figure 7.6 on the left), refrigerant lines (supply and return), and a cryosurface with cryogenic feedthrough (Figure 7.6 on the right). The refrigeration unit can pump cold or hot refrigerant (for defrost) in a continuous loop through the refrigerant lines and cryosurface. The refrigerant is a proprietary mixture of refrigerants made by Brooks Polycold Systems Inc.

Figure 7.6: On the left PFC refrigerator unit and on the right cryo-trap before installation. The cryosurface is a serpentine flowing within the vacuum chamber.

The primary application of PFC is to capture water vapour in the vacuum chamber. Water vapour is usually the most reactive contaminant in a high-vacuum system, and comprises 65% to 95% of the residual gas in such systems. For this application, the cryosurface is a coil. The coil can be quickly cooled and defrosted to correspond with vacuum chamber cycles. In other kinds of vacuum systems this apparatus can also be used to minimize backstreaming. Backstreaming is a phenomenon where oil diffusion pumps are used. Some of the hot oil from the diffusion pump migrates into the vacuum chamber, where it condenses onto surfaces, contaminating the system. For this application, the cryosurface is a baffle.

Figure 7.7: Polycold system after installation and commissioning at LNL. On the left the PFC refrigerator, on the right the vacuum chamber with inside the refrigerating coil. On the flange are visible the cryogenic feedthrough and, with black thermal shielding, the cooling line.

Figure 7.7 shows the vacuum system with assembled the Polycold refrigerator. The installation, commissioning, and first starting of apparatus was carried out by the supplier and required several working days. The installed PFC has a theoretical maximum pumping speed of $7.4 \cdot 10^4$ ls^{-1} and has a conservative pumping speed ad $5 \cdot 10^4$ ls^{-1}. The ultimate operating pressure could be $7 \cdot 10^{-9}$ mbar with an average cryo-surface temperature of 129 K.

Plot of Figure 7.8 shows the pressure in function of time during a standard pumping down without baking of the vacuum system. After approximately 18 h of pumping down using only the turbo pump, the Polycold cold trap was switched on. It is possible to observe how chamber pressure drops about one order of magnitude in few seconds.

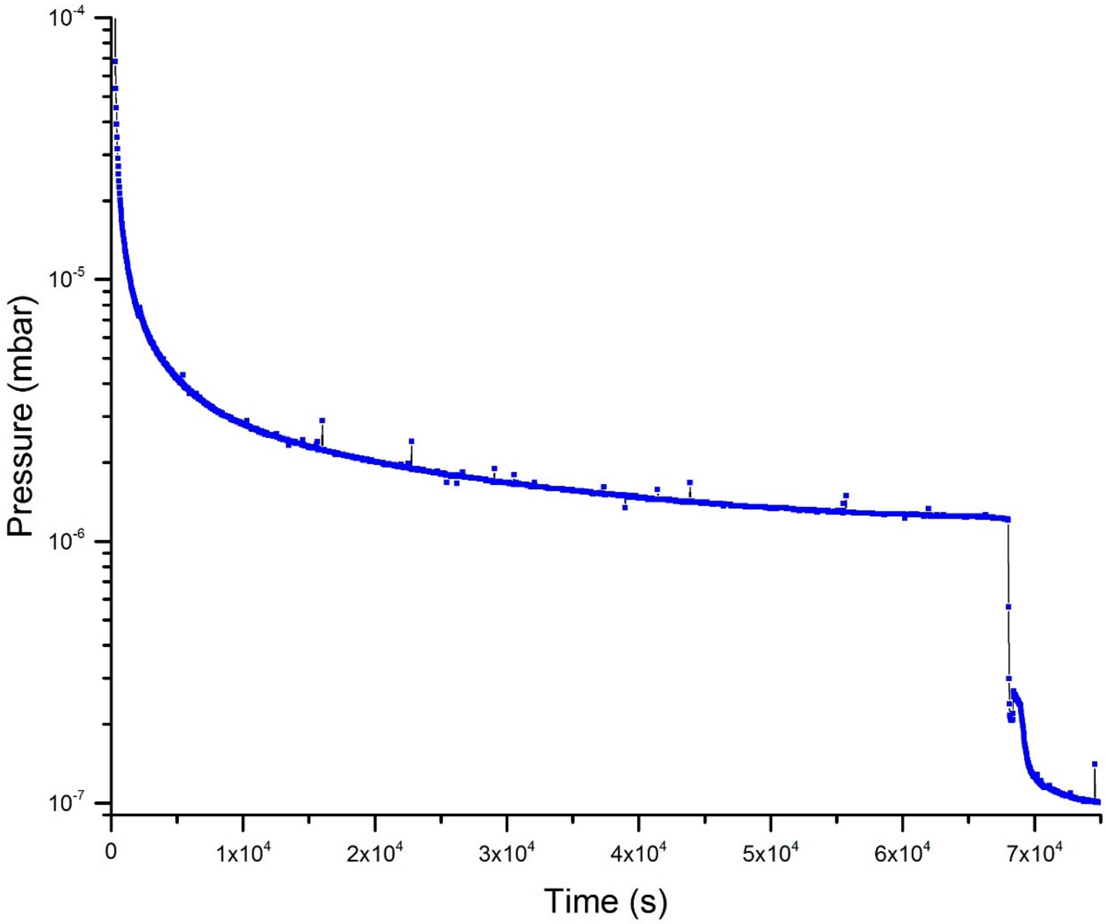

Figure 7.8: Plot of pressure (mbar) in function of time (s) without chamber baking. It visible on the right after 18 h pumping ($\approx 6\cdot 10^4$ s) the switching on of PFC system.

7.4 The Quartz tube

A fundamental component of the vacuum system is the process chamber. In this case, it consists of a quartz tube with internal and external diameters respectively of 240 and 250 mm. The total length is 2000 mm. Quartz is a very particular material due to its mechanical, electrical, thermal, chemical and optical properties. In fact, quartz is a group IV metal oxide, which has good abrasion resistance, electrical insulation and high thermal stability. All these characteristics mean that quartz is the desired material for our application. Helios Quartz supplied the quartz tube used in inductive heating facility; the grade is standard NHI®-1100 and the physical characteristic are summarised in Table 7-1.

The material chosen for manufacturing the vacuum process chamber is quartz principally for these reasons:

- It is insulating with high electrical resistivity, so it is not heated by the electromagnetic field generated by the inductive heating system. In this configuration, we can heat directly the cavity that is in vacuum without introducing any heating system inside the vacuum chamber. The benefit is a very high reduction of impurities due to electrical hoven.

- It has very good mechanical proprieties, so it can be used as vacuum chamber.
- It has a high melting point and softening temperature; it is possible to heat cavity until 800 °C without any problem.
- It has a low degassing rate.
- It is transparent at visible wavelength and also infra red, so it is possible to use a pyrometer for reading processed components in vacuum, less impurities in vacuum.

Table 7-1: NHI®-1100 Quart Proprieties produced by Helios Quartz.

Characteristic	Value
Atomic mass	60.08 [g/mol]
Melting point	1830 °C
Boiling point	2950 °C
Softening Temperature	1630 °C
Density @ 20°C	2.2 [gr/cm^3]
Hardness @ 20 °C	522 [HV10]
Young's modulus @ 20 °C	66.3-74.8 [GPa]
Tensile Strength	47 [MPa]
Poisson's ratio	0.17
Linear coefficient of thermal expansion @ 20 °C	$5.5 \cdot 10^{-7}$ [m/(mK)]
Thermal conductivity @ 20 °C	1.4 [W/mK]
Electrical resistivity @ 20 °C	10^{12} -10^{16} [Ωm]
Specific Heat @ 20°C	660 J/Kg·K
Refractive Index	1.46
Permittivity	3.8-5.4

In order to dimension quartz tube, different mechanical simulation with FEM software were made. In fact, it is mandatory to prevent buckling of vacuum chamber.

Buckling instability is characterized by a sudden sideways failure of a structural member subjected to high compressive stress, where the compressive stress at the point of failure is less than the ultimate compressive stress that the material is capable of withstanding. Particular attention should be given to pressure vessel subject to external overpressure like in the case of vacuum vessel. These vessels risk buckling due to compressive hoop stresses. The hoop stress is the force exerted circumferentially (perpendicular both to the axis and to the radius of the object) in both directions on every particle in the cylinder wall. Hoop stresses can be described as:

$$\sigma_h = \frac{\Delta PD}{2t} \tag{7-1}$$

where *ΔP* is pressure difference, *D* external diameter and *t* wall thickness. Buckling occurs when Force W given by:

$$W = \frac{4\pi^2 \mathrm{EI}}{(\pi D)^2} \tag{7-2}$$

It is equal to the hope force that can be derived by equation (7-1). In equation (7-2), *E* is Young's modulus and *I* is area moment of inertia. Equating equations (7-1) and (7-2) we obtain the pressure difference that originates buckling in a vacuum vessel as first approximation is:

$$\Delta P_{buckle} = \frac{2\mathrm{E}}{3}\left(\frac{t}{D}\right)^3 \tag{7-3}$$

Unlike vessels, which are designed for internal pressure alone, there is no single formula, or unique design, which fits the external pressure condition. The thickness of the cylinder is only one part of the design. Other factors that affect the design are the length of the cylinder, the use, size, etc. Vessel subject to external pressure may fail at a value well below the yield strength of the material. Failure can occur suddenly, by the collapsing of the components.

For this reason, it is of fundamental importance the prediction of possible buckling phenomena onto quartz. Finite element analyses are done to investigate the expected stresses and deformations and are done with Solidworks® Simulation package that include a tools for buckling analysis. This analysis calculates the critical failure loads of the quartz tube. SOLIDWORKS Simulation calculates the buckling load factor which is a scale factor for the applied load to obtain the critical load, that is similar in nature to the stress factor of safety (FoS).

The constraint on the simulations were placed fixing the bottom surface of the cylinder (that in real system is lean on fixing flange). In a preliminary study was simulated only a ΔP of 1 bar between the internal and external part of quartz vessel, room temperature and a force of 5000 N acting on the top that is equal to the pressure acting on the top flange. This first set of simulation give a Buckling Factor of Safety (BFS) equal to 15.9. If BFS Is greater than 1 means that the applied loads are less than the estimated critical loads and buckling is not expected.

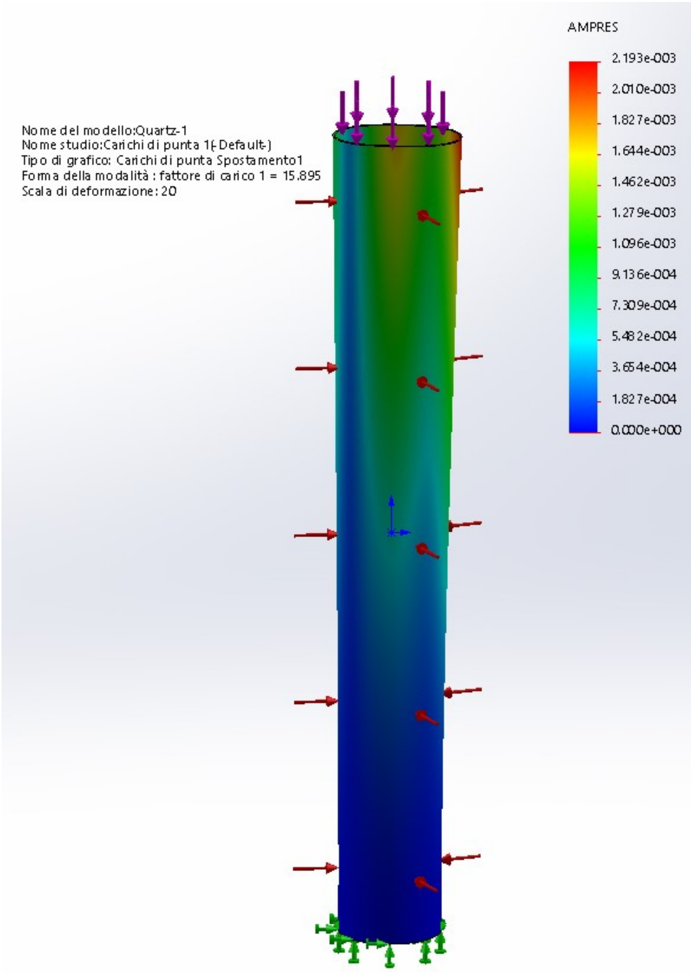

Figure 7.9: Graphics representation of quartz tube deformation (scale factor 20) obtained for buckling simulation. Only pressure in this case is simulated.

Thanks to the promising results, other simulations were carried out. In particular, the first adding on the top annulus of the quartz other 2000 N corresponding to the weight of the magnetron source that can be entirely sustained by the quartz structure. In this case, the structure could support the weight (BSF 15.85) but, anyhow, a stand for the source is designed.

Another set of simulations were run increasing quartz temperature at 473 K an 873 K. The simulated BSF is respectively -63.14 and -5.4. A negative value indicates that buckling is not expected even if you reverse all load, but the temperature of 600 °C starts to be critical for quartz.

All these simulations confirm the quartz thickness of 5 mm. Appendix 2 shows a simulation report, where are listed the various simulation parameters like applied forces, mesh, pressure, temperature and constrains.

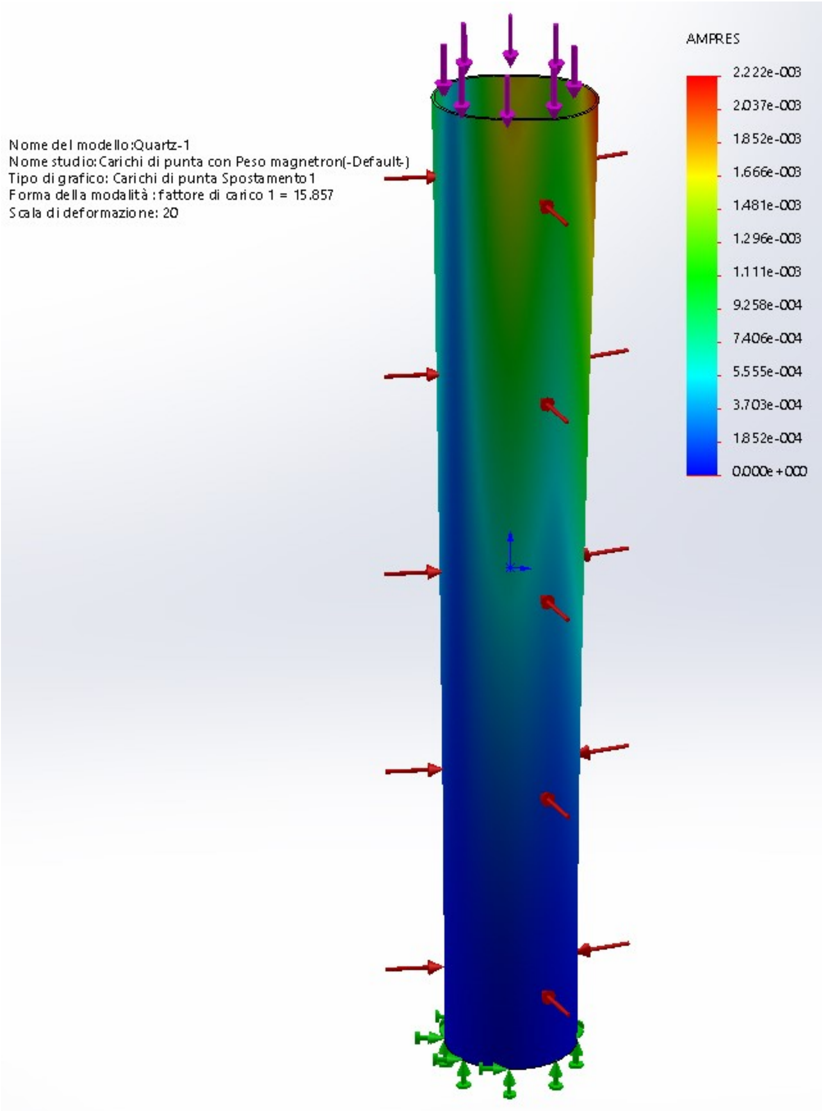

Figure 7.10: Graphics representation of quartz tube deformation (scale factor 20) obtained for buckling simulation. Pressure and force in this case are simulated.

7.4.1 Quartz tube crack

During preliminary test (Chapter 9), unfortunately the quartz tube cracks on one side due to the sealing configuration. This inconvenient has led to further delay in the study of magnetron source. In fact, two month were necessary for the machining of quartz tube. The tube has been shortened by 200 mm in order to remove the cracked side.

In this period, re-design of vacuum tight between quartz and vacuum system has also been carried out. In particular, the aluminium flange fixing quartz tube and guarantee vacuum tight, were machined in order to insert a rubber ring between the aluminium base and the end of the quartz. This configuration avoid the direct contact between metallic flange and SiO_2 tube, so the force exerted by pressure during vacuum production (≈5000 N) is amortised by the o-ring and there is no longer the danger of a crack on the extremity of quartz vacuum chamber. The o-ring is not continuous so it does not generate virtual leaks, the vacuum sealing is always guaranteed by Viton o-ring that presses the quartz externally; Figure 7.11 shows a scheme of this configuration.

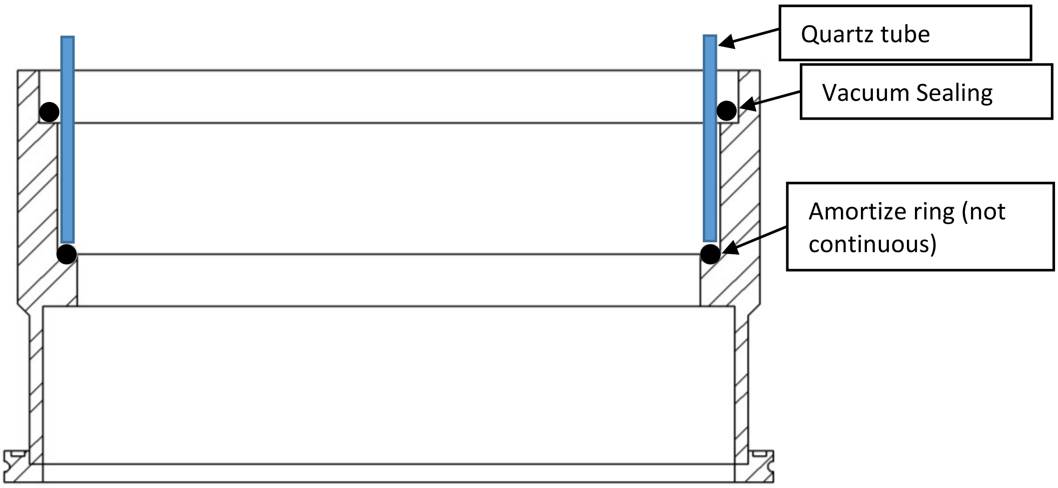

Figure 7.11: New aluminium flange design.

7.4.2 Quartz tube substitute

Due to quartz tube crack, the use of other material as process chamber where taken into account. It must be transparent to RF, able to work at high temperature and it must guarantee ultra high vacuum performance.

The other material suitable for this application could be alumina, which can be produced in tube with high of 2000 mm and diameter of 250 mm. The disadvantage of this material is that is not transparent in the visible wavelength, and it is more porous than SiO_2.

In order to evaluate the possibility of using this material, different simulations using COMSOL® software where made. Heat Transfer module combined with Electromagnetic Module were used in order to simulate the heat produce by the induced currents on a material inside a variable magnetic field produced by the inductor. The current used in the simulation is 3000 A with a frequency of 30 kHz and the real section of the copper coil was used. The results obtained are summarised in Figure 7.12. The temperature, which should be reached outside vacuum chamber by the tubes, is approximately the same.

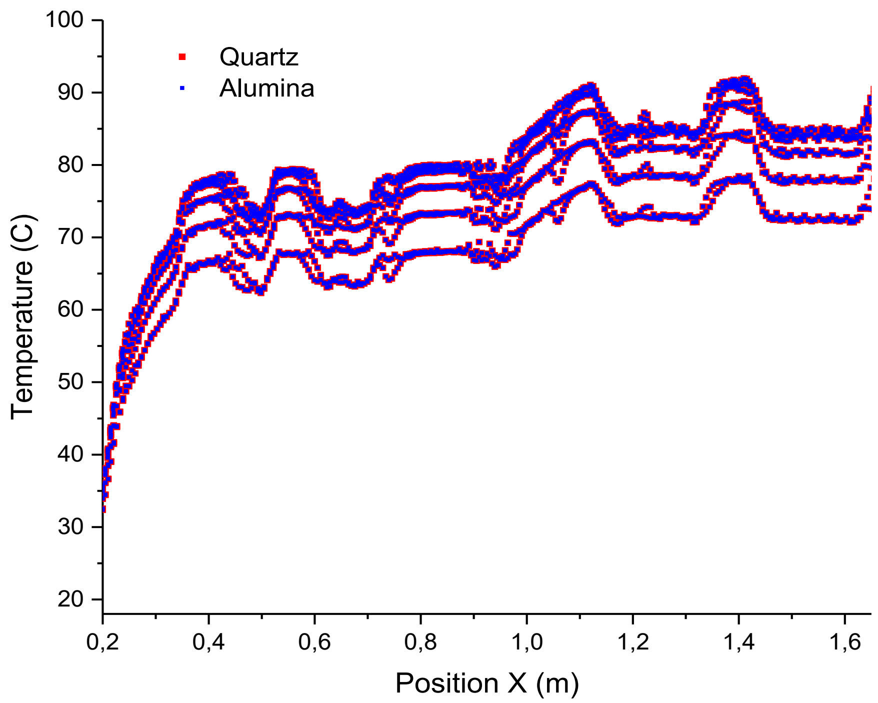

Figure 7.12: Simulate temperature distribution along quartz and alumina tube using COMSOL

7.5 Vacuum performance

After the design and commissioning of the vacuum system, we proceed with the assembly. In order to guarantee ultra-high vacuum performances, all the components were cleaned first in ultrasonic bath using Rodaclean NGL soap (specific for Stainless Steel) for 60 minutes and then rinsed with ultrasonic deionized water. Following, the components were dried with filtered nitrogen and assembled using dust free glows.

To check the tightness of all the vacuum flanges several leak detection tests were performed.

It is important to remember that each surface exposed to the vacuum shows a gas emission essentially due to four reasons:

1) Permeation, that is the passing of gas through the separation wall from an environment at higher pressure to one a lower pressure;
2) Diffusion from the bulk material, that can be from interstitial type or through the vacancies;
3) Desorption of molecules previously adsorbed to the surface;
4) Vapour pressure of the material that composes the surface itself.

The combined effect of these phenomena is labeled "degassing" and represents (together with possible leaks) the main limit to the minimum pressure that can be reached in a Ultra High Vacuum system.

The specific outgassing speed of a system is expressed in terms of quantity of gas per unit time per unit surface, expressed in $(mbar \cdot l)/(s \cdot cm^2)$ and it depends on the kind of material considered and its history. The following procedure has been used to estimate the outgassing rate of the complete system: the pendulum gate valve is closed in order to seal the chamber and the chamber pressure is monitored with time (see Figure 7.13). The basic pressure is $5 \cdot 10^{-8}$ mbar. With an inner calculated surface equal to 1.12 m^2 and a volume of 1126 lt, the degassing rate is calculated using:

$$\mathrm{Q}_{out} = \frac{dP}{dt}\frac{\mathrm{V}}{A} \tag{7-4}$$

The value dP/dt is the pressure speed increasing into the chamber, obtained interpolating linearly the pressure variation with time. Without baking an outgassing rate equal to $1.1 \cdot 10^{-8}\,(mbar \cdot l)/(s \cdot cm^2)$ is obtained. That value was absolutely not deemed sufficient to obtain high quality superconducting Nb films.

An “UHV BAKING CONTROL” heating boxes (Figure 7.14) monitors the heating process. This box controls and regulates the temperature of three zones of the system with three different heating units. A digital timer allows setting the process time. The heating strips are supplied, through the box, with 220V and controlled with Resistance Temperature Detectors (RTDs). The heating unit allows setting the zone temperature and the maximum temperature (Alarm) one zone could reach before the entire heating process is shut down. The electrical connection are all in the heating box rear panel.

The baking is performed at 120 °C in order to preserve the Viton sealing for 48 h.

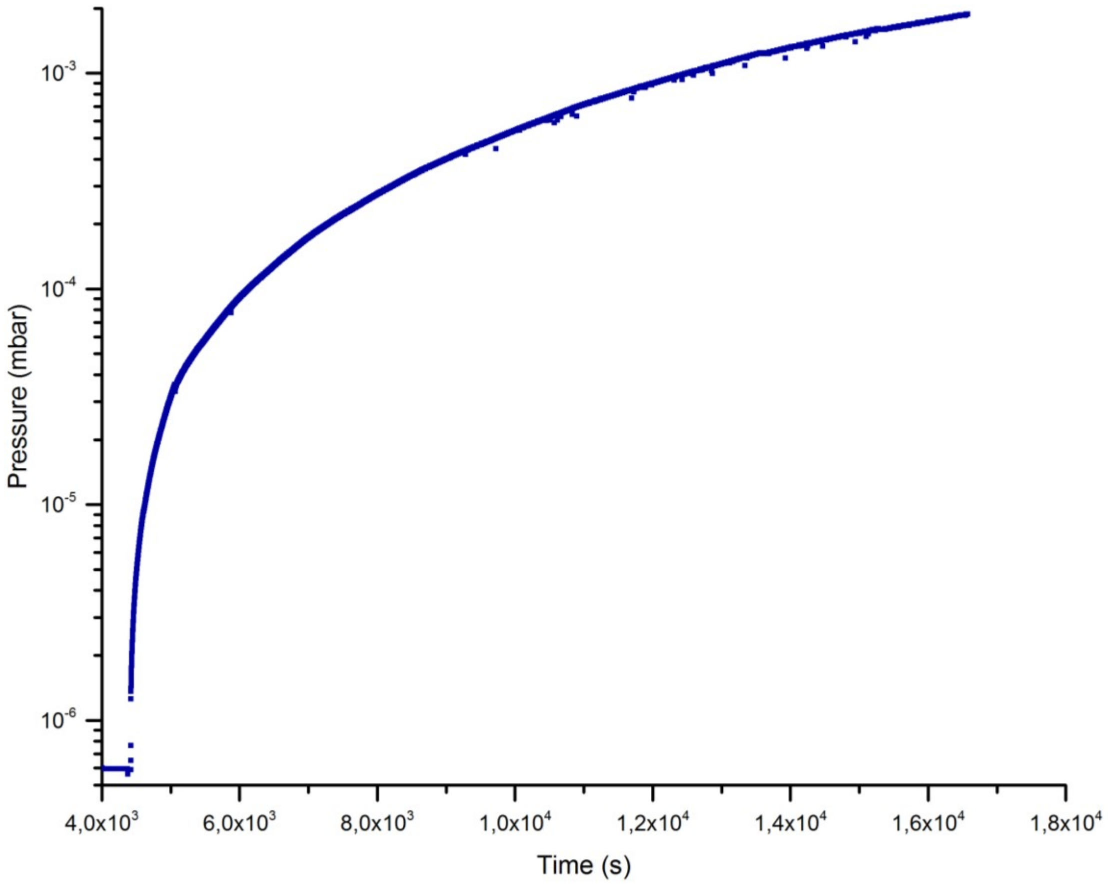

Figure 7.13: Outgassing curve obtained without chamber baking.

Figure 7.14: UHV Baking controller.

Chapter 8

Thin Film Deposition

8.1 Thin films coating

Thin films allow combining the bulk properties of materials with the surface properties of others. Many materials are needed as the demand for high technology products increases. An efficient and most often less expensive way to meet the increased demands is the use of thin films. Thin films are material layers with thickness ranging from a few atomic layers (nm) to a few micrometres. Thin films can be deposited by several techniques: electroplating, chemical vapour deposition, physical vapour deposition, and a number of combinations of these methods.

Physical vapour deposition methods for producing coatings in a vacuum environment can be separated into two main groups:

1) Thermal evaporation techniques, where the material is heated in vacuum until its vapour pressure is greater than the ambient pressure;
2) Ionic sputtering methods, where high-energy ions strike a solid and knock off atoms from the surface. Ionic sputtering techniques include diode sputtering, ion-beam sputtering and magnetron sputtering.

8.2 Fundaments of sputtering

A material-bombarding particle, like a single atom, ion or molecule with a relatively high potential energy can give rise to the ejection of Υ electrons (secondary electrons) or other phenomenon, like breaking or rearranging chemical bonds. If the kinetic energy of the bombarding particles exceeds the binding energy of the atoms, atoms of the lattice are pushed into new position; surface migration of the atoms and surface damage can arise.

At energies exceeding roughly 4H (where H is the sublimation heat of target material that coincide with the binding energy of atoms), ejection of atoms into the gas phase or their dislodging start to play an important role [71]. This process is called physical sputtering. In physical sputtering, ions rather that neutral atoms are used for bombardment, as with ions one can have the desired kinetic energy accelerating them with electrical fields.

The sputtering with high kinetic energy can be considered as three dimensional billiard game with atoms. A bombarding ion is reflected or scattered backward from the collision event with the target atoms and the number of collisions depend on the atomic mass relation between the bombarding ion and the target atom. Embedding of bombarding ions into the lattice appears when the kinetic energy exceeds ≈100eV.

Maximum sputtering yields (atoms emitted per incident ion) occurs at different energies for different ions, being proportional to the ion mass. Measurements of sputtering yield and of the average velocities of sputtered atoms (which are much higher than those of evaporated atoms) show that sputtering is a rather inefficient process. Usually, more than 95% of the ion energy appears as heat in the target [71]. When we will design a new magnetron for coating of 9-cell resonator, we will have to take into account this inefficiency for the dimensioning of possible cooling system.

The energy region of primary interest for the sputter deposition of thin film stretches from threshold (as, for example, during bias sputtering) to about 5keV. During sputtering, the atoms may be ejected as excited atoms or as negative or as positive ions. In plasma sputtering, the ejected positive ions are pulled back to the negatively charged target, while the negative ions and Υ electrons are accelerated away from the target surface. The energy of these negative ions can be so high that can cause resputtering of the material that they reach (substrate).

In a sputtering process, parameters such as kinetic energy of the ions, electronic structure of the collision partners, binding energy of the lattice atoms, lattice structure and orientation are involved and play an important role to the sputtering yield.

Several terms can be used to understand the sputtering process: cathodic sputtering, diode sputtering, RF or DC sputtering, ion-beam sputtering and reactive sputtering, but all of these processes are variants of the same physical principle. Sputtering is the process where atoms or molecules of a material are ejected from a target by the bombardment of high energy particles. Specifically, cathodic sputtering is a process in which the bombardment is produced by positive ions derived from an electrical discharge in a gas and the material is ejected from the target in order to obtain quantities of material that can be coated directly onto substrates (Figure 8.1).

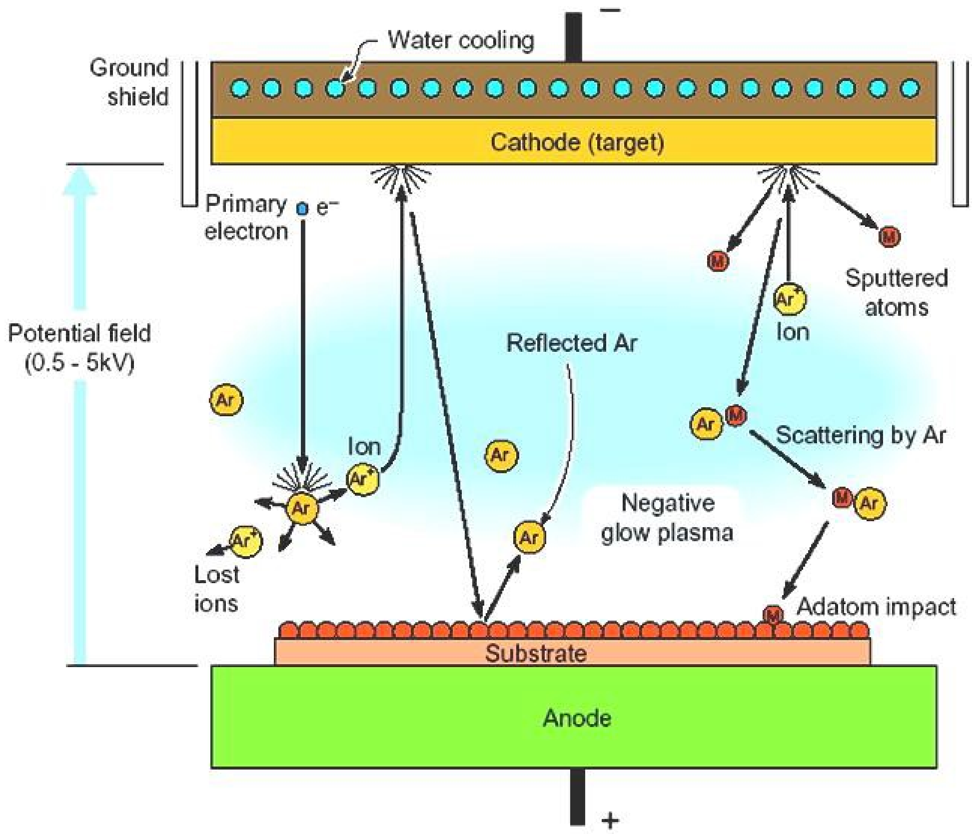

Figure 8.1: Scheme of sputtering deposition process. In DC diode sputtering system, Ar is ionized by a potential difference, and these ions are accelerated to a target. After impact, target atoms are released and travel to the substrate.

8.3 Sputtering mechanism

As sputtering process is a glow discharge or a plasma process, which uses ionized gas atoms or molecules accelerate in an electric field to erode a material from a source, a strong negative field is applied to the target to attract positive ions, hence a sputter deposition is referred to as the cathode. If a thin film with the same chemistry composition as the target is desired, a noble gas (e.g. Argon) ambient is typically used.

In DC plasma sputtering the discharge is fed and maintained by the electrons of the thermionic cathode and not by Υ electrons from the glow discharge cold cathode. The advantage of this is that sputtering can be maintained without a magnetic field even at low gas pressure (low mTorr region). In DC glow discharge pressure is greater then few mbar.

When an ion with energy more than about 30 eV hits a surface, part of this energy and momentum of the incoming ion will through lattice collisions, be reversed and may cause ejection of surface atoms, i.e. sputtering [72]. The sputtered atoms leave the target surface with relatively high energies (~10 eV) respect evaporation atoms (~0.1 eV). The average number of the atoms ejected from the surface per incident ion is called sputtering yield [73]. The ion source is usually a plasma (an electrically neutral mixture of positive ions and electrons) generated by electron impact in a noble gas at sub-atmospheric pressures (2-3 Pa). The ions are accelerated in an electric field obtained by applying a negative potential with respect to the plasma potential to an electrode immersed in that plasma. The ejected or sputtered atoms can be condensed on a substrate to form a thin film.

The sputtering yield *Y*, depends on several factors, such as the mass and the energy of the incident particles, the mass and energy of the sputtering atoms, the crystallinity of the target, etc. This is the most important parameter to characterize the sputtering process and it is measured in atoms per incident ions:

$$Y = \frac{N_{sputtered\ atoms}}{N_{incident\ ions}} \tag{8-1}$$

The Y value can range from 0.1 to 10. Sputtering yield depends on the following parameters [71]:

1) Bombarding ion energy influences the sputtering yield as explained above;
2) The atomic number of colliding atoms: the atomic masses of target element or compound influence the energy transfer as follow:

$$E = \frac{4mM}{(m+M)^2} \tag{8-2}$$

where m is the mass of the target atoms and M is the incident ion mass. It is evident that for high sputtering yield the mass of target atom should be not very different from the mass of the bombarding ion.
3) The experiments clearly show that the noble gas ions give the highest sputtering yield. This happens for the fact that the inert gases are not interested in "stealing" the electrons needed to make ionization collision near the cathode.
4) Angle of incidence of the ions: The sputtering yield increases when less directional change of the momentum is required for ejecting atoms. This happens at more oblique incidence. The sputtering yield follows the $\cos^{-1}$ law and arrive a maximum for angles 45°-50° from the surface, but for values near 90° (perpendicular to the surface) the effect of ion reflection becomes dominant and sputtering yield decreases.

The deposition rate is a function of the sputter yield, the flux of ions impinging on the target, transport of the deposited flux to the substrate, and sticking of that material to the substrate.

8.4 Sputtering configuration

Sputtering is a technique by which atoms and ions of argon or other gases from plasma bombard a target thereby knocking atoms off the target. These material atoms travel to a substrate where they are deposited and form a thin film. The simplest configuration of a sputtering source is shown in Figure 8.1.

8.4.1 Diode sputtering

Diode sputtering configurations consist of two electrodes placed in a vacuum chamber.

The substrate where the film is deposited is placed on the anode, while the target that will be sputtered represents the cathode (the negative electrode). High or ultrahigh vacuum is necessary to achieve thin film purity. After evacuation to high vacuum or ultra high vacuum (UHV), the chamber is filled with the sputtering gas, usually Argon, at the pressure of 10^{-2}-10^{-1} mbar. Applying a DC voltage of ≈500V between electrodes will create a glow discharge that will ionize the argon gas. Positive ions of argon will be accelerated towards the cathode and due to their kinetic energy will eject atoms from the target surface. The ejected atoms have energies of the range of several eV. They will diffuse in chamber, following the $\cos^{-1}$ law till they condense on the surface of the substrate. The high kinetic energy of the sputtered atoms leads to a better adhesion and higher density of the sputtered thin film. Figure 8.1 shows a typical diode sputtering configuration.

8.4.2 Magnetron sputtering

In order to get high sputtering rates and good film performance, DC magnetron sputtering is widely used. To improve the efficiency of diode source, primary electrons must be used effectively to make sufficient ionization collisions close to the cathode. The efficiency of the available electrons can be increased if the plasma is confined by a magnetic field parallel to the cathode surface. A general rule for the shape of the magnetic field is: Magnetic field must born from the cathode and die onto the target. That means that a plasma confinement is achieved, while magnetic and/or electrostatic mirrors trap the electrons. Magnetic field traps and forces electrons to describe helical paths around the lines of magnetic force

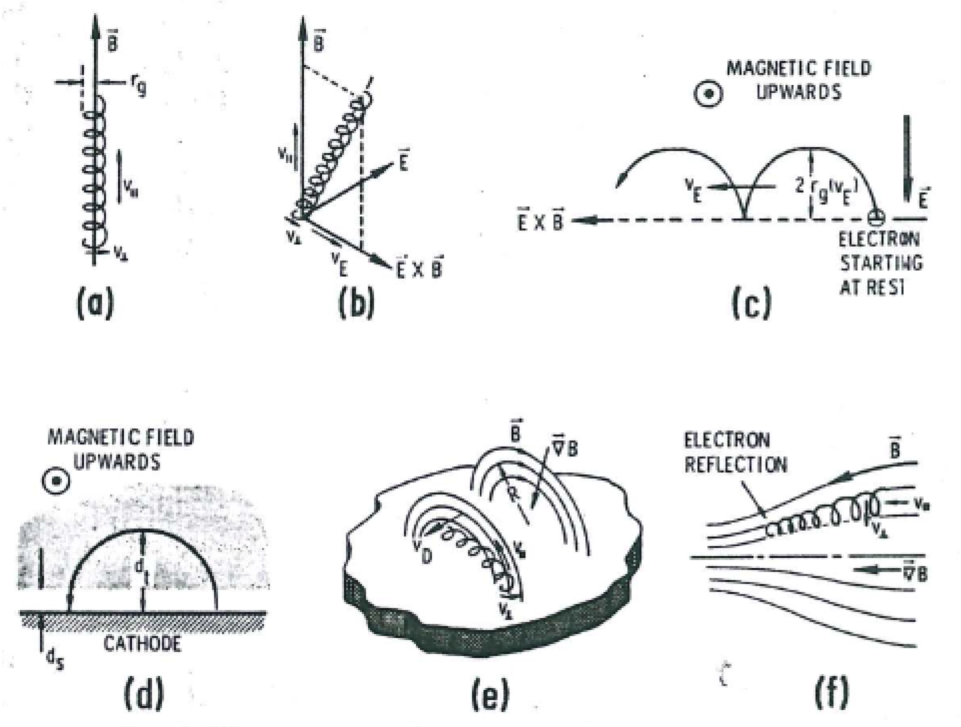

Figure 8.2: Electron motion in static electric fields [74]. a) electron drift along the magnetic field lines. b-f) movement of the electron in an electromagnetic field when there is electric field component $E_\perp$ (Volts/cm) perpendicular to B.

When **B** and **E** are uniform and **E** is parallel to **B**, the particles are freely accelerated and the helix pitch increases continuously. When there is an electric field component $E_\perp$ perpendicular to **B**, a drift of speed:

$$v_E = 10^8 \frac{E_\perp}{B} = \frac{\vec{E} \times \vec{B}}{B^2} \qquad (8\text{-}3)$$

develops in a direction perpendicular to both $E_\perp$ and **B** and combines with the orbiting motion as shown in Figure 8.2-b.

When **B** is uniform and **E** is zero, the electrons drift along the field lines with a speed $v_\parallel$ which is unaffected by the magnetic field, and orbit the field lines gyro or cyclotron frequency.

$$\omega_c = \frac{eB}{m_e} = 1.76 \times 10^7 \cdot B \left[\frac{rad}{sec}\right] \tag{8-4}$$

For a particle created at rest in uniform and perpendicular **E** and **B** fields, the trajectory becomes the cycloid generated by a circle of radius r_g:

$$r_g = \frac{v_E}{\omega_c} = \frac{m_e}{e}\left(\frac{v_\perp}{B}\right) = 3.37\frac{\sqrt{W_\perp}}{B}\,[cm] \tag{8-5}$$

Where B is in Gauss and $W_\perp$ is the energy associated with the electron motion perpendicular to the field in eV. The motion is an helix has shown in Figure 8.2-a.

If the charge is immersed in both electric field **E** and magnetic field **B**, its equation of motion is:

$$\frac{d\mathbf{v}}{dt} = \frac{e}{m}(\boldsymbol{E} + \boldsymbol{v} \times \boldsymbol{B}) \tag{8-6}$$

or rather:

$$\boldsymbol{F} = e(\boldsymbol{E} + \boldsymbol{v} \times \boldsymbol{B}) \tag{8-7}$$

only the electron motion (not the ions) is influenced by the magnetic fields of the strengths used in sputtering source operating in the magnetron mode.

The drift speed of the charged particles is perpendicular to the electric and the magnetic field, and it reaches its maximum intensity when both fields are orthogonal:

$$v_d \propto \frac{\boldsymbol{E} \times \boldsymbol{B}}{B^2} = \frac{\left(v_\parallel^2 + \frac{1}{2}v_\perp^2\right)}{\omega_c R} \tag{8-8}$$

where *R* is the field radius.

With the introduction of a magnetic field the electrons run along longer path, thus increasing the probability of collision. The same effect can be achieved increasing the gas pressure. With a magnetic field, sputtering at lower pressure (10^{-3} mbar) is possible; on the other way, if the pressure in not reduced, it is possible to obtain greater current for a given applied voltage.

In order to confine electrons on the target it is possible to act on three situations:

1) making electrons deflecting into closed paths;
2) by magnetostatic bottle;
3) by electrostatic mirror.

In the design of the source for coating 9-cell cavities we will take into into account all these principles.

8.4.3 Cylindrical magnetron sputtering

Coaxial cylindrical magnetron sputtering sources in which post or hollow cathodes are operated in axial magnetic fields have been reported for a number of years. However, their performance is limited by end losses. A remarkable performance is achieved when the end losses are eliminated by proper shaping of the magnetic field or by using suitably placed electron-reflecting surfaces. Figure 8.3 shows different configuration of cylindrical magnetron.

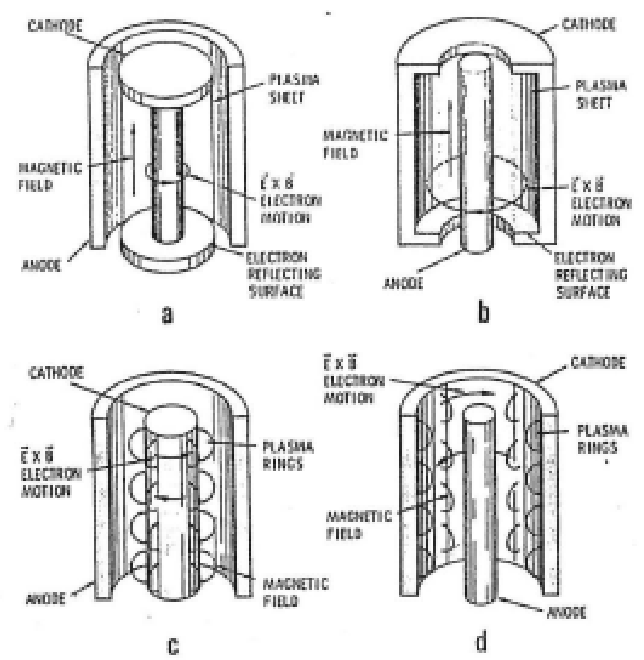

Figure 8.3: The configuration of various magnetron sputtering sources: (a)-(d) are cylindrical magnetrons; (b) and (d) are often called inverted magnetrons and sometimes hollow cathodes; (a) is referred to here as a cylindrical-post magnetron and (b) as a cylindrical-hollow magnetron [74].

In the post magnetron case, the cylinder is the cathode and the outer cylinder is the anode (substrate), while in the hollow cathode case it is vice versa. In both cases, cathode wings (mirrors) are necessary to achieve plasma confinement.

The advantage of using magnetic field is that in a field of about 300 Gauss a current of several amperes at 500V could be obtained. This is a great improvement as compared with a current of only a few tenths of an ampere at 1500V without a magnetic field. The magnetic field used in sputtering sources is of the range of 10^{-2}T (100 Gauss) and does not influence the ions but only the electrons.

In a relatively uniform magnetic field, a uniform intense plasma will form along the barrel and will extend outward a distance W. The smallest wing size W should be at least three times larger than the gyro radius of the primary electrons emitted from the cathode.

With this criterion the field strength, wing size, and operating voltage are related to each other in the following way:

$$BW = 10\sqrt{V} \tag{8-9}$$

Fields from 30 to 200 G are usually employed.

8.5 Thin film growth

During sputtering process deposition of the film material is done atom by atom on the substrate. One of the advantages of the sputtering versus thermal evaporation is that sputtering yield of different materials do not vary that much. Thus refractory materials, which require high temperature and low vapour pressure, sputter almost as readily as any other materials. The microstructure and properties of coating deposited is, however, influenced a lot from the plasma sputtering environment, which can be manipulated [75].

The deposition of thermally evaporated metals in the form of tapered grains was determined by Movchan and Demchishin [76] to occur at temperatures below about 1/3 of the respective melting temperature. Thornton adapted their zone diagram for metal coating deposited by plasma sputtering just adding a second axis for sputtering gas pressure (Figure 8.4). The diagram adapted by Thornton indicates that the microstructure properties of the sputtered film depend not only on the substrate temperature, but also on the gas pressure. The Zone 2 that appears at ⅓ of melting temperature in thermal evaporation occurs first at $\frac{1}{2}T_m$ (melting temperature) at the deposition by plasma sputtering.

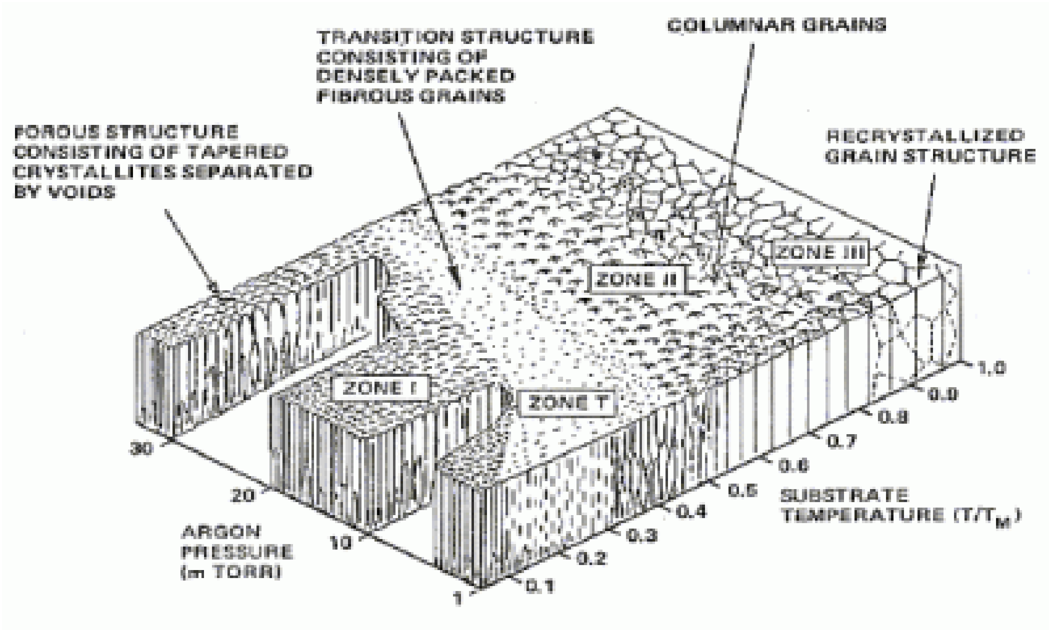

Figure 8.4: Structural zone model proposed by Thornton for metal coatings grown by sputtering

8.6 Thin film growth in sputtering regime

A positive bias applied between target and substrates promotes ion bombardment of the growing film. If the film is given a negative potential with respect to the plasma, the resulting technique is referred to as bias sputtering. In this way films are subjected to a certain amount of resputtering that causes the desorption and breakup by ion bombardment of the surface adsorbed species; whether or not this will occur depends on the relative strengths of the metal-to-impurity and the metal-to-metal bonds. The fraction fi of impurities of species i trapped in a film is given by:

$$f_i = \frac{\alpha_i N_i}{\alpha_i N_i + R} \tag{8-10}$$

where N_i is the number of atoms of species *i* bombarding unit area of film in unit time during deposition, α_i is the effective sticking coefficient of the species *i* during deposition and *R* is the deposition rate of the film [71]. It is clear from equation (8-10) that f_i can be reduced by increasing *R*.

Considering the bias process equation (8-10) is modified as

$$f_i = \frac{\alpha_i N_i - \beta}{\alpha_i N_i - \beta + R} \tag{8-11}$$

where β is a function of the bias current due to impurities ions.

The main advantages of the insertion of a biased electrode are:

- the removal of most impurities during resputtering;
- the rearrangement of atoms during film growing;
- the densification of the crystal structure;
- the higher sputtering rate;
- lattice rearrangement;
- films quality improvement;
- increasing of the coating hardness;
- similar defect annealing as does an elevated substrate temperature;
- the electrons bombardment reduction;
- adhesion improvement.

On the contrary applying the wrong bias voltage can cause noble gas atoms embedding, lattice defects, thickness reduction and still the hydrogen removal rate is low, due to the high sticking coefficient of this molecule [77].

All these problematics and rules were considered during the design of vacuum system and sputtering cathode source. Given the benefits of bias, indeed, the design of cavity holder was made in order to permit to apply a bias tension to the same.

8.7 Characterization technique

Different methods are used to analyse the microstructural, surface mechanical properties and the functional properties (RRR and T_c) of the niobium thin films sputtered before coating the final 9-cell cavity.

8.7.1 Thickness measurements

The thickness was measured by using the profilometer. The profilometer is a tool that drag a stylus across a surface and records the topological profile.

Moreover, a profilometer is a device used to measure relative surface roughness, peak to valley, in order to quantify its roughness. They may operate in either contact or non-contact modes and may use optical or stylus techniques to make the actual measurements [78].

The profilometer used is a Dektak 8 has the followings features:

1) Combines high repeatability, low-force sensor technology, and advanced 3D data analysis.
2) 7.5 angstrom, 1 sigma step height repeatability and a vertical range of up to 1mm.
3) Scan lengths to 200 mm.
4) Low force sensor option offers stylus forces down to 0.03 mg.
5) High aspect ratio tips ideal for measuring Shallow Trench Isolation (STI) etch depth and deep structures.

Figure 8.5 shows the profilometer used to measure the thickness of quartz samples.

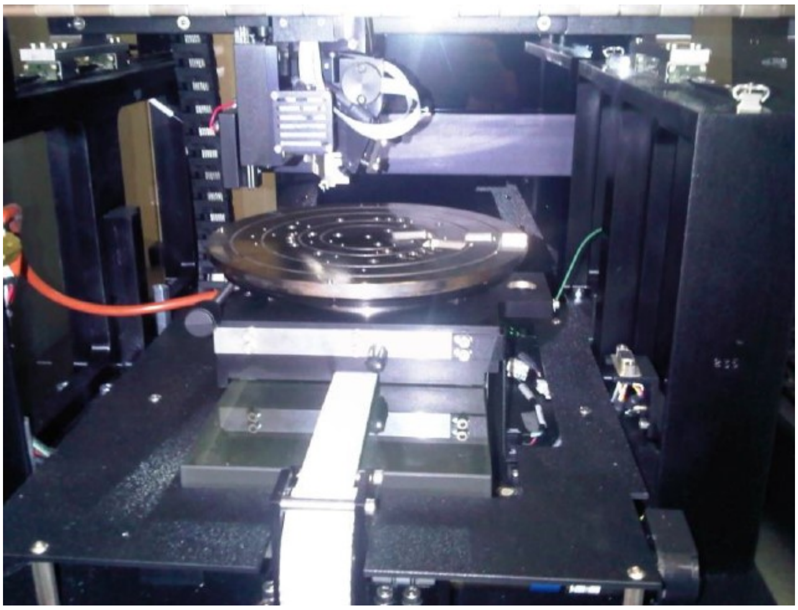

Figure 8.5: Dektak 8 Profilometer used to measure the thickness of quartz samples.

8.7.2 RRR and T_C

After the thickness measurements, superconducting properties were also valuated. Residual Resistance Ratio (RRR) and critical temperature (T_c) were measured by using the four-terminal sensing.

The four-terminal sensing is a DC technique in which the average size of the samples often is around 1-15 mm^2 and 30-300 mm length. The measurement starts cooling down slowly the sample by immersion into liquid helium and temperature sensors control the temperature. With the four-point method one set of conductors drives the current through the sample and the second set picks up the voltage as is shown in Figure 8.6 [79].

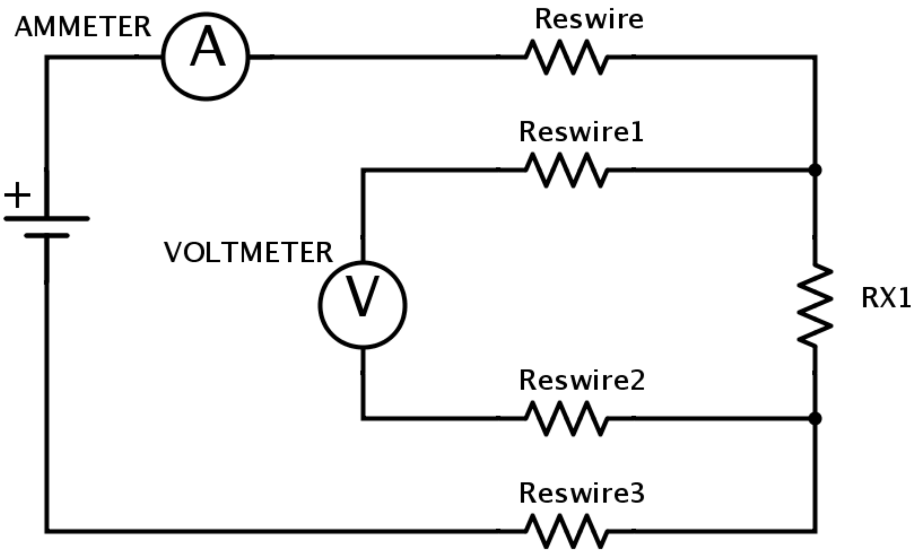

Figure 8.6: Scheme of four-terminal sensing.

The resistance is determined using the Ohm's law and in this case the resistance is measured between the two points on the sample where the voltage contacts are located. A DC current of 2,5 mA is applied to the sample and the resulting voltage is measured to determine the resistance, while a specific software is used to acquire data from 300 to 4,2 K and plot the curve of resistance versus temperature.

The low temperature resistance of the sample is determined at 10K and the RRR calculated with the following formula:

$$RRR = \frac{R_{300K}}{R_{10K}} \tag{8-12}$$

RRR is an immediate estimate of the film quality: as RRR increases as the purity of the material increases.

The transition temperature $T_C \pm \Delta T_C$ is measured from the resistances vs temperature curve, applying the following equation:

$$T_C = \frac{T_{(90\%)} + T_{(10\%)}}{2} \tag{8-13}$$

$$\Delta T_C = T_{(90\%)} + T_{(10\%)} \tag{8-14}$$

where $T_{(90\%)}$ is the temperature corresponding to the 90% of the resistance before the transition, $T_{(10\%)}$ is the temperature corresponding to the 10% of the resistance before the transition. ΔT_c is the error on the critical temperature estimation.

8.7.3 SEM

SEM is a characterization technique that can provide information on surface topography, crystalline structure, chemical composition and electrical behaviour on the top of a specimen. In a SEM the incident electrons from an electron gun have energies of 2-40 keV. The most common electron gun is a tungsten filament that is heated to 2500°C to produce thermal emission electrons from its tip. The interaction of the electron beam with the specimen produces secondary, backscattered and Auger electrons, X-rays and perhaps light collected by various detectors in the specimen vacuum chamber. The signal from each detector can be fed to a monitor. The magnification of the image is determinate by the ratio of the side length of the monitor display to the side length of the raster on the specimen.

8.7.4 X-Ray Diffraction

The diffraction data were collected using a Philips Xpert Pro diffractometer. This is a rapid analytical technique primarily used for phase identification of a crystalline material and can provide information on unit cell dimensions.

X-ray diffraction is based on constructive interference of monochromatic X-rays and a crystalline sample. These X-rays are generated by a cathode ray tube (in our case Cu K_α), filtered to produce monochromatic radiation, collimated to concentrate, and directed toward the sample. The interaction of the incident rays with the sample produces constructive interference (and a diffracted ray) when conditions satisfy Bragg's Law. This low, indeed, permit to calculate interplanar distance:

$$2d_{hkl}\sin\theta = n\lambda \tag{8-15}$$

and the lattice parameter for Nb case that as a cubic structure so ($a = b = c = a_0$):

$$a = \frac{\sqrt{h^2 + k^2 + l^2}}{d_{hkl}} \tag{8-16}$$

Using Debye-Scherrer equation that correlate diffraction peak width ($\Delta 2\theta$) with crystallite size, it is possible also to estimate this quantity:

$$D_{hkl} = \frac{0.9\lambda}{\cos\theta \cdot \Delta(2\theta)} \tag{8-17}$$

where D_{hkl} is the mean crystal dimension measured along the normal to the surface and it is expressed in Angstroms.

In order to understand the morphology and the grain size of the niobium deposited on the quartz, samples placed along the cavity walls are planned to be analyzed.

Chapter 9

Design of an Innovative Magnetron Source

9.1 R&D onto sputtering cathode

The main of the R&D was the study of the cathode configuration, evaluating different shapes and magnetic confinements in order to deposit a Niobium thin film over the internal walls of a 9-cell elliptical cavity. The aim is to obtain a uniform coating, with high adhesion onto the substrate and with excellent superconductive proprieties along the entire cavity. Different configurations were evaluated; the following paragraphs report the solutions considered with the corresponding benefits and problems.

9.2 Mobile magnetron assembled on a feedthrough

The configuration consists in a cylindrical magnetron source with a mobile magnet pack inside, able to move axially along the tube. Historically it is the most studied configuration and have been used by different laboratories to coat SC cavities like at CERN for LEP or LHC.

G. Lanza studied in detail this configuration for one cell cavity, analysing different cathode configurations and magnetic field confinements [80].

The cathode is located on the axis of the system (figure 6.5). It consists of a vacuum tight stainless steel tube (liner) surrounded by a niobium tube. The niobium tube is a rolled niobium sheet, welded by using the electron beam technique.

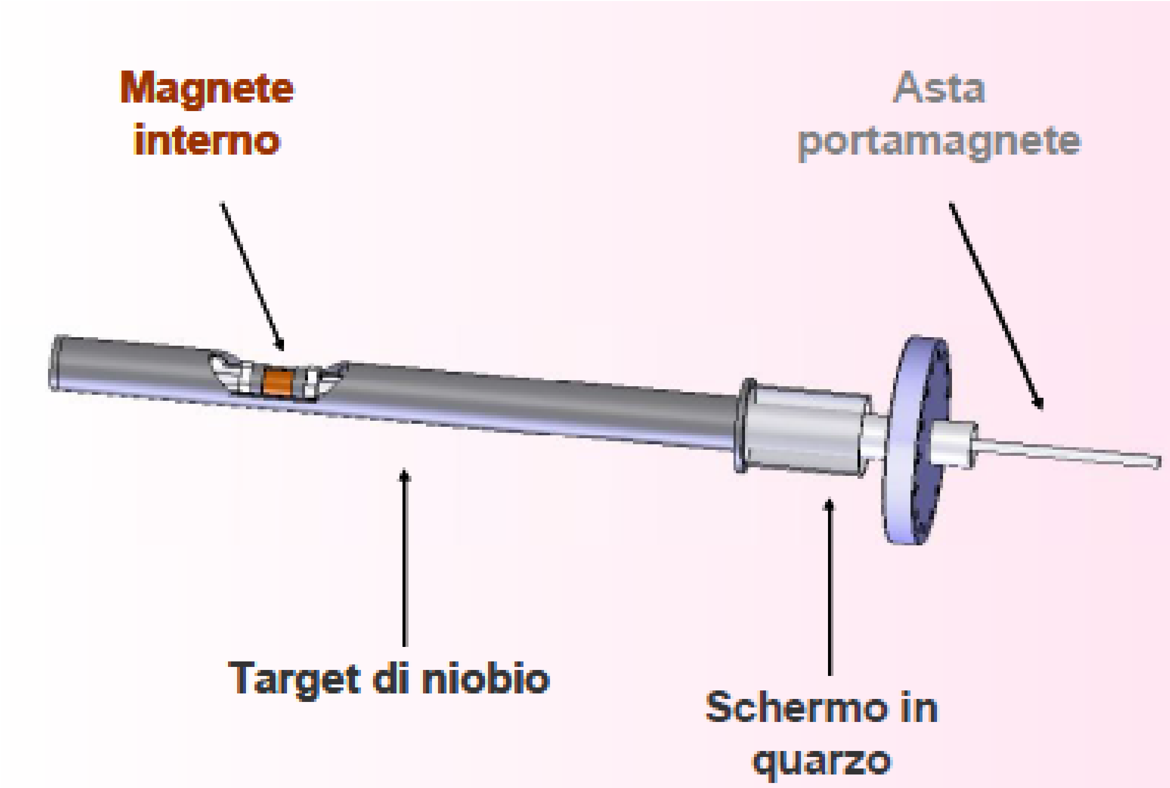

Figure 9.1: Cylindrical standard one cell cathode [80].

The liner is welded to a flange CF100 and closed at the base with a TIG welded plate. It supports the Niobium cathode and the quartz screen; a Niobium disc, fixed to the steel tube by a screw, prevent the falling of the cathode, while the quartz screen avoids the insulator metallization. Inside the stainless steel tube two cylindrical magnets are normally placed, split by an iron yoke.

Experiments carried out by D. Tonini at al. [81] at LNL laboratory also highlight the strong dependence of superconductive properties with the angle between the cathode and the substrate. According to the study, there is a decreasing of T_c and RRR vs. coating angle, moreover increasing the incidence angle of the atoms with the perpendicular to the substrate:

1) the superficial roughness rises, showing a maximum at 75°;
2) the superconducting critical temperature decreases;
3) the RRR value decreases;
4) the film shows preferential growing directions that differ from the normal one.

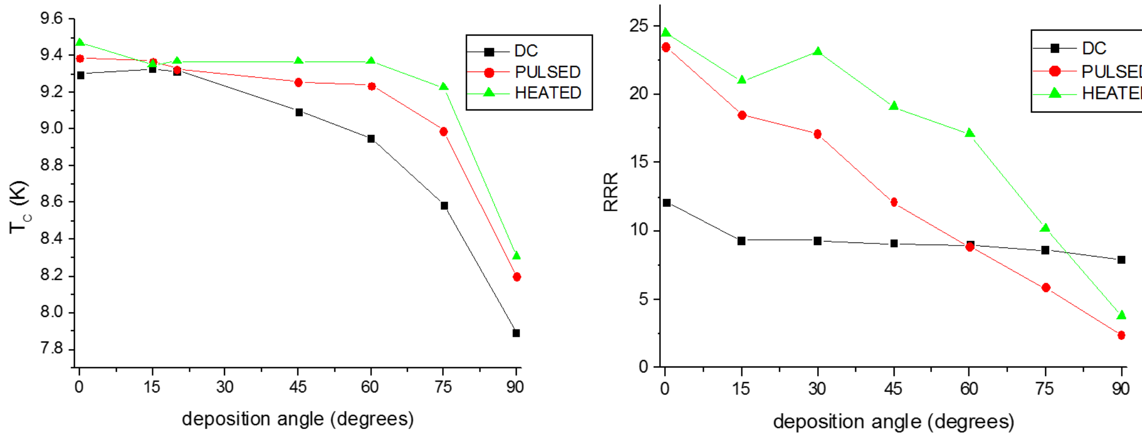

Figure 9.2: T_c and RRR trends with angles of films sputtered at different target-substrate angles during three distinct sputtering configurations [81].

Considering mobile magnetron assembled on a feedthrough configuration, although it is default used, present different kinds of problems. Moreover, carrying it to 9-cell cavity would surely highlight additional issues.

The simplest solution would be to insert 9 small magnetrons inside the 9-cell cavity and simultaneously sputter the cavity itself. This solution will be economic and already tested, but our laboratory experience underlines that decoupled plasmas on the same target, produce plasmas with different intensities, which are reflected in a thickness unevenness and, consequently, non-uniformity of superconductive properties.

Another solution could be the use of only one magnetron source and coat one cell at time. In this case, the coating time would be much longer; would also be needed a vacuum motion feedthrough longer around 2 meters for a total height of the coating system of about 5 meters. Further, there is also the possibility that the sputtering of a cell goes to pollute the adjacent cells with a coating, made not in optimal conditions.

9.3 Static magnetron source

The configuration taken into account consists in an innovative cathode without magnets inside. In order to guarantee the best coating uniformity, a cathode cavity-like shape was chosen; in particular, the cathode is designed as 6 GHz Niobium cavity. The inductor heater generates the magnetic field necessary for sustaining the magnetron source. Indeed, taking into account the penetration depth δ at the working frequency of inductor, around 1 kHz (as described in paragraph 6.2.2) it is approximately 2.16 mm at room temperature for copper cavity that is comparable with the cavity thickness wall that is approximatively of 3 mm.

Penetration depth is directly related to the resistivity that over Debye temperature, for copper is 315 K [82] (see Table 3-2 at page 45), has not a linear dependence, instead is proportional to T^5 as discussed in paragraph 6.2.2.

In order to increase the adhesion between substrate and coating it is fundamental to coat the cavity at a temperature around 600 °C. At this temperature, δ (appendix 1) is around 4 mm, so a relevant fraction of magnetic field passes through the copper cavity and could be used to confine electron close to the cathode surface.

In order to test this promising and innovative configuration, two different setups were designed and will be discussed in paragraphs 9.3.1 and 9.3.2.

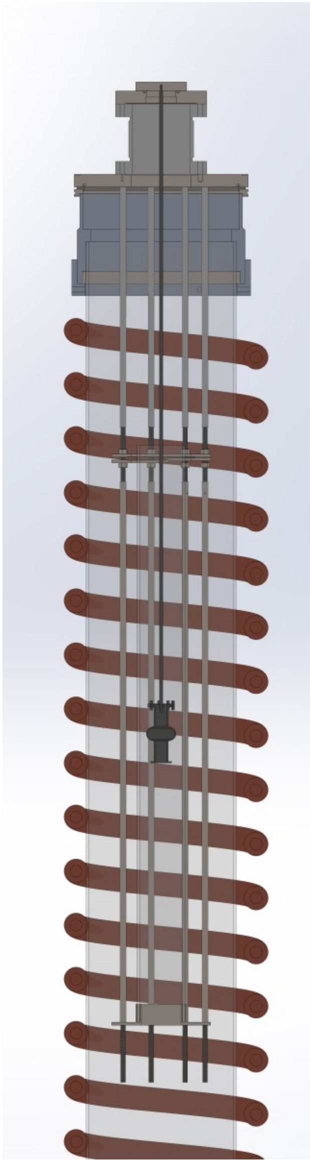

Figure 9.3: Section of 6 GHz test magnetron with quartz inner tube.

Figure 9.3 shows the first test configuration. On the centre the inductor, it is placed the 6 GHz Niobium cavity, used as magnetron cathode.

The structure to sustain this source was designed and assembled.

9.3.1 Static magnetron source: first test with quartz shield

Around the cathode 6 GHz cavity, for the first test, a quartz tube is integrated internally to the chamber quartz tube to allow the visual observation of the plasma, avoiding the metallization of the outer quartz tube (see Figure 9.4). The whole cathode structure is designed in Niobium. Indeed, the rod supporting the cathode, the support plates, the screws and the 6 GHz cavity is machined using bulk Niobium.

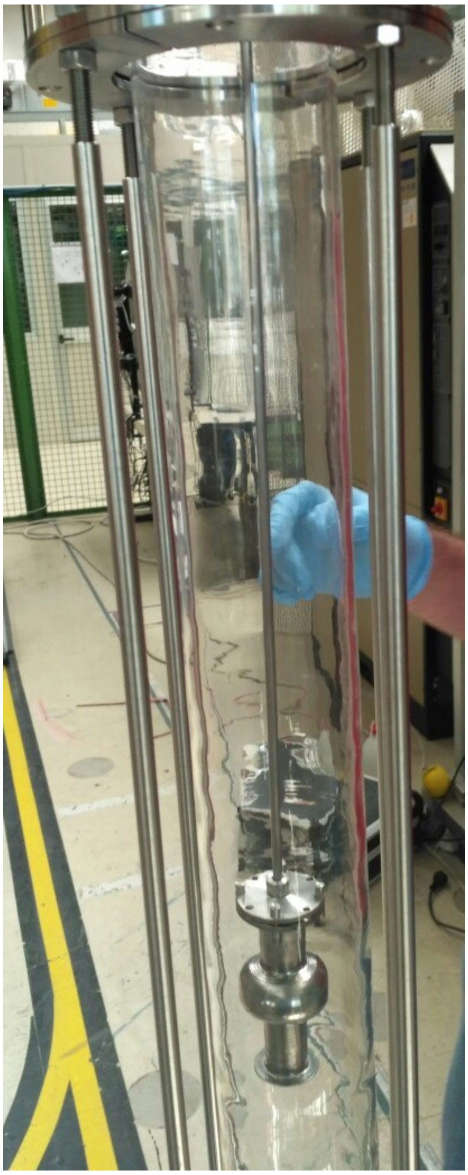

Figure 9.4: 6 GHz cathode Niobium cavity assembly with quartz shielding.

This first test has yielded positive results, in Figure 9.5 is visible the sputtering plasma close to the 6 GHz cavity used as cathode.

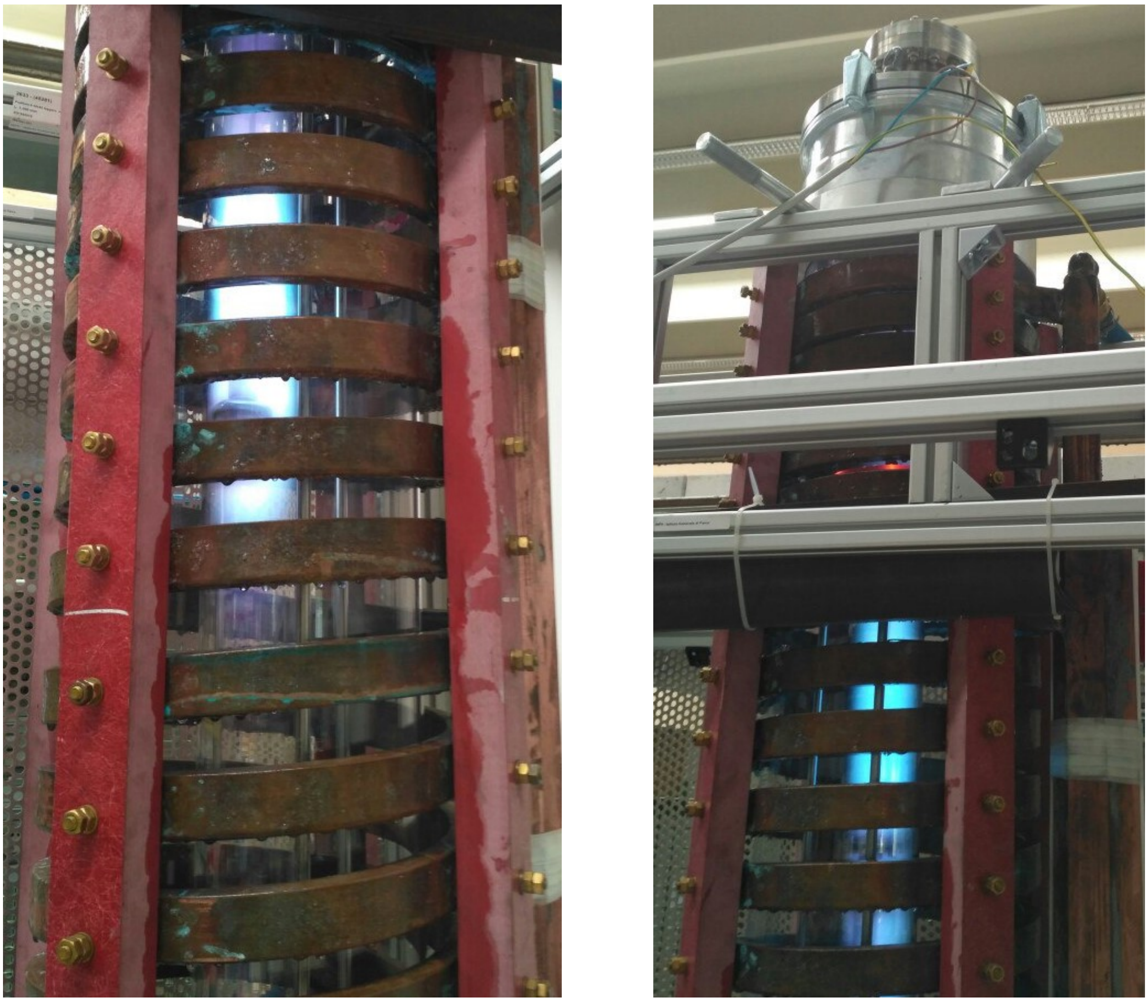

Figure 9.5: Two pictures of plasma during first test sputtering test using 6 GHz cavity as cathode.

The vacuum base pressure before sputtering was $< 4 \cdot 10^{-6}\, mbar$, during the process the Argon pressure was $5 \cdot 10^{-2}\, mbar$. The parameter used during this first test are summarised in the Table 9-1.

Since the number of coils of the inductor is 28 for a total length of 1.6 m, it is possible to calculate the magnetic field starting from Faraday's low induction that, in a first approximation, the magnetic field axial and internal to the spiral is given by:

$$B = \mu \cdot \frac{N}{\ell} \cdot I \approx 11\, G \qquad (9\text{-}1)$$

where N is number of spires for the length ℓ and I the current passing through the solenoid. This magnetic field is sufficient to ignite the plasma and to sputter the Nb cathode but is not so intense in order to promote a good plasma confinement.

Table 9-1: Sputtering parameters during first test.

Parameter	Value
Sputtering Tension	418 V
Sputtering Current	0.51 A
Sputtering Power	210 W
Inductor Tension	401 V
Inductor Current	48 A
Inductor Frequency	15.6 kHz
Inductor Power	19.2 kW
Sputtering Ar pressure	$5 \cdot 10^{-2}$ mbar

Figure 9.6: Sputtered quartz tube.

Figure 9.6 quartz tube with the Niobium coating inside.

9.3.2 Static magnetron source: second test with Cu shield

Figure 9.9 shows the second setup. A copper tube substitutes the inner quartz tube in order to simulate the cavity design. On the copper tube, some special holes were made in order to accommodate test samples (Figure 9.7). In this way, we can test and measure the magnetron performance coating quartz samples with a dimension of 10x10 mm^2 fixed on the copper tube (see Figure 9.8).

Figure 9.7: Particular of copper tube with holes for holding quartz samples.

Figure 9.8: Quartz samples fixed onto the Cu tube.

Analysing the penetration length at the tuning frequency measured on previous setups (see paragraph 9.3.1), we observe that δ at 15.6 kHz, is approximately 0.52 mm it means that for this length, the magnetic field falls to $1/e$, (about 37 %) of its original value.

The wall thickness of the tube is 2 mm, so the magnetic field inside the tube is only ≈0.23 G, not enough sufficient to ignite and sustain a sputtering discharge. The introduction of the copper tube will change the inductor parameters (frequency and current) and also the magnetic field strength. Figure 9.9 shows a rendering section of the system assembled. On the center is visible the Niobium cathode 6 GHz cavity, all around it the copper tube used to simulate the cavity that must be coated.

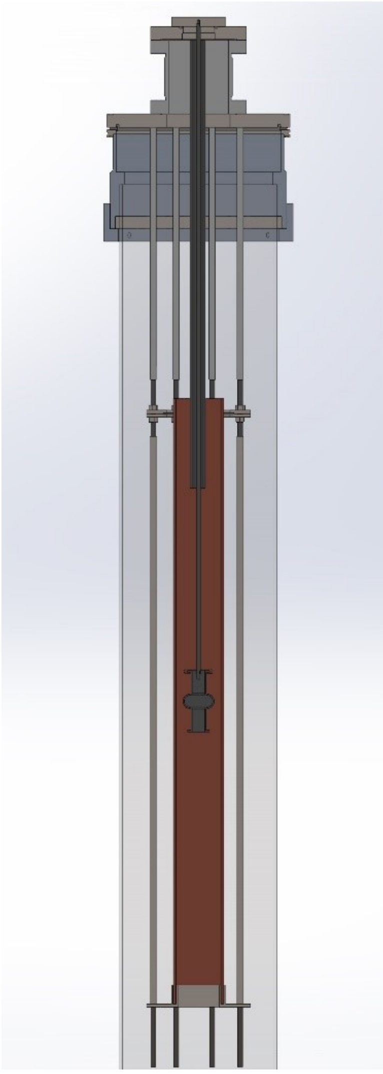

Figure 9.9: Section of 6 GHz test magnetron simulating the copper cavity.

Figure 9.10 shows the assembly ready to be inserted inside the vacuum system, on the left the whole system with visible the quartz samples, on the right a particular of the centring system of the upper side of the copper tube. The rod visible in the center of the copper tube is the Nb support of the 6 GHz cavity. The test has 2 objectives: first to establish whether the plasma lights up inside the cavity and second, to analyse the deposition uniformity of the source.

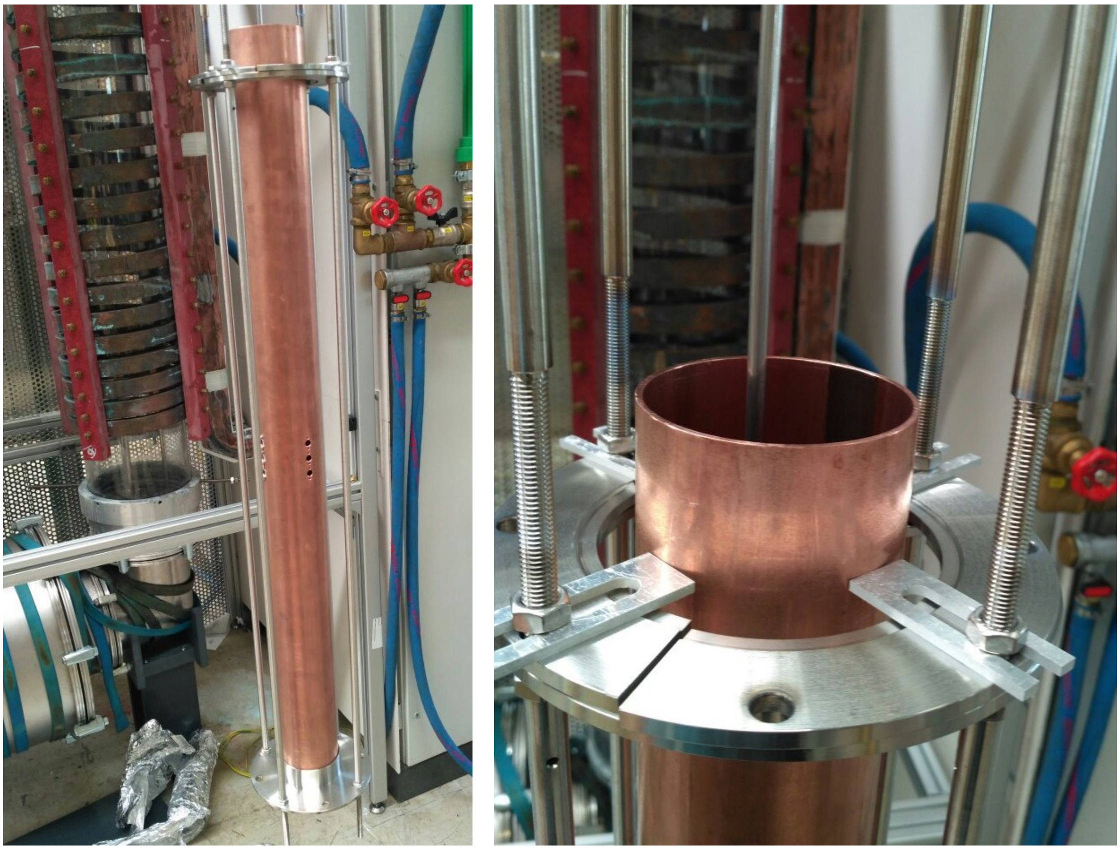

Figure 9.10: Left: picture of the copper shield assemble on the system, on the centre 6 quartz samples are visible. Right: a detail of the upper centring system of the Cu tube.

The vacuum base pressure before sputtering in this test was $< 4 \cdot 10^{-7}\ mbar$, during the process the Argon pressure was from $5 \cdot 10^{-2}$ to $2.5 \cdot 10^{-1}\ mbar$ The parameters used during this first test are summarised in Table 9-2.

Table 9-2: Sputtering parameters during second test.

Parameter	Value
Sputtering Tension	760 V
Sputtering Current	0.31 A
Sputtering Power	236 W
Inductor Tension	380 V
Inductor Current	82 A
Inductor Frequency	8 kHz
Inductor Power	31.1 kW
Sputtering Ar pressure	0.5-2.5·10^{-1} mbar

Figure 9.11 shows the sputtering process. It is visible the plasma inside the copper chamber from the hole used to fix the samples.

Figure 9.11: Argon plasma inside the copper tube during sputtering process.

As could be observed from Table 9-2, the inductor current during process is around 82 A and it generates a 18 G magnetic field inside the coil. In this case, with 2 mm Cu tackiness the magnetic field close to the magnetron is only 1.16 G, not enough to ignite the plasma.

in fact, the plasma is ignited at high Ar pressure (≈10^{-1} mbar) in diode mode, in this test, and the magnetic field is insufficient to confine electrons close to the cathode surface. Figure 9.11 shows the plasma inside the cavity.

Evaluating the results, the plasma starts in diode mode and the intensity was not sufficient for coating the test samples.

9.3.3 9-cell cavity coating magnetron design

Figure 9.12 shows the final sputtering choice, capable to coat a 9-cell cavity simultaneously in each cell. The magnetron structure is composed by nine Nb 6 GHz cavities connected between them by a Niobium tube.

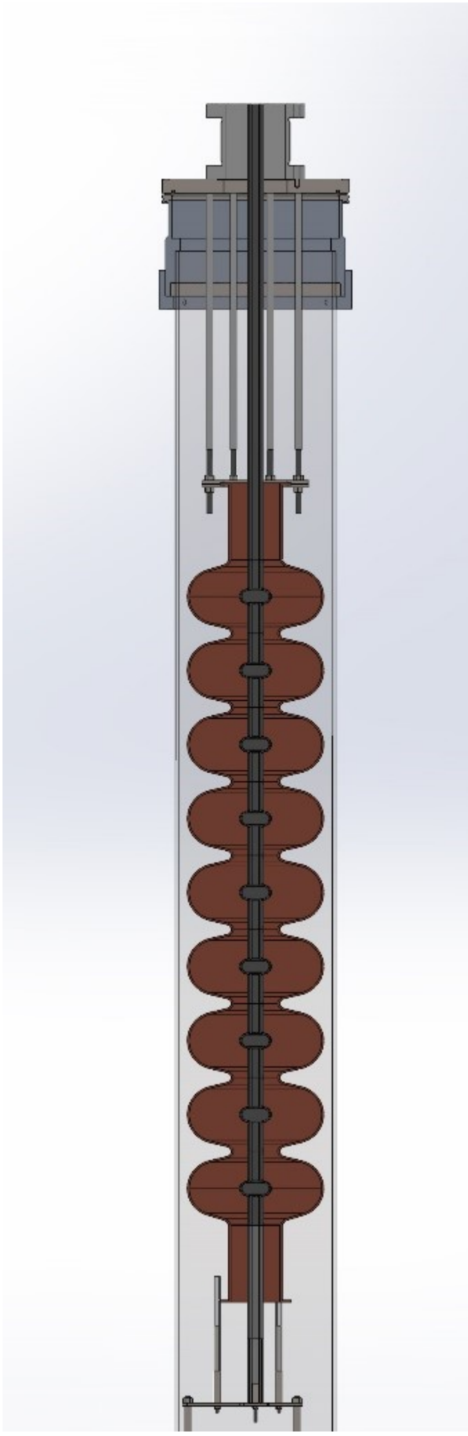

Figure 9.12: Magnetron optimized for coating 9-cell cavity. The cathode is composed by nine 6 GHz cavities connected by Nb Tube. Eight SS rods support the copper cavity. On the bottom is visible the cavity centring system.

The inductive heating coil generates the magnetic field necessary for sustain the plasma (Figure 9.12). Eight Stainless Steel rods support the copper cavity. The rods have also the possibility to bias the cavity during the sputtering process. There is no cooling system inside the cathode, in this configuration, due to permanent magnets are not present and Niobium melting temperature is 2468 °C.

Figure 9.12: shows a detailed section of the apparatus. The external inductor coil is visible. It provides the electromagnetic field for heating the copper cavity and the magnet field necessary to sustain the plasma. The inductor is in air, external to the quartz vacuum chamber. On the other side, in vacuum, it is visible the 9-cell copper cavity and the Niobium cathode composed by nine 6 GHz cavities fixed by a Niobium tube. The cathode works at a tension of -800 V and the plasma generated on its surface erodes the niobium for coating the internal surface of the copper cavity.

Due to the preliminary results discussed in previous paragraph (9.3.2) this configuration probably won’t work in LNL facility, unless there is any hardware implementation on the inductor heating system.

For example will be fundamental the possibility to modify:

- **coil current** in order to increase the magnetic field generate by the induction heating coil;
- **coil current frequency**, in order to increase the penetration depth and so increase the magnetic field penetrating through the cavity such magnetic field could be used to confine electrons close to the cathode and generate plasma discharge.

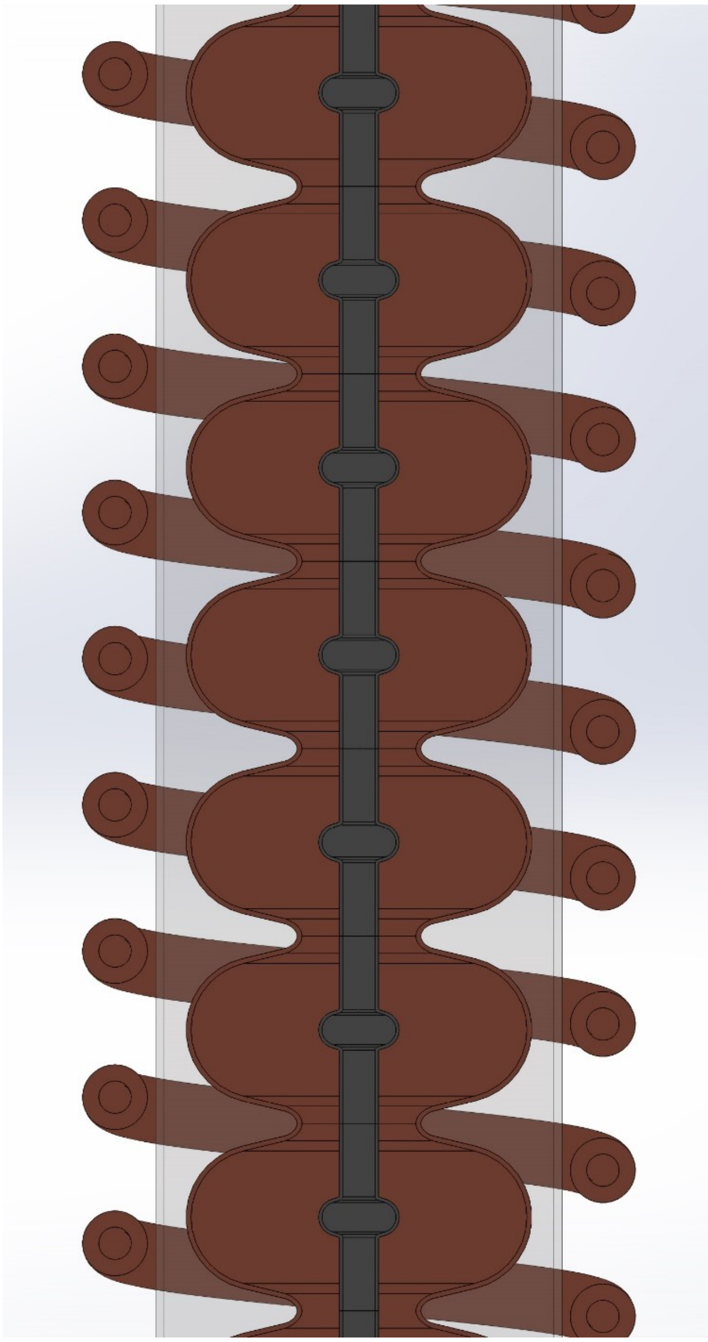

Figure 9.13: Detail of the magnetron. The spiral of external inductors are visible. Inside the quartz tube is visible the 9-cell copper cavity and the 6 GHz niobium cathode.

9.4 Fixed magnetron with rotary magnets

Another possible solution evaluated, consists in a magnetron source composed by rotating magnets. Adapting the work performed by Dr. Franco for ISOLDE QWR [83] (also enhanced by a patent [84]), it is possible to design a rotary magnetron with a magnetic configuration capable to generate a plasma along the entire cavity and to coat all the 9-cell uniformly.

For this application, it was decided to work on two different cases. The first one consists in generating a “spiral” along the cathode using North-South magnets. The plasma is horizontal on the cavity equator and it is vertical along the cavity cut off (Figure 9.17). In this way, also the deposition rate is higher on the cavity equator (where there is a higher surface) and lower along the cut off. It is possible to obtain a uniform coating along the cavity and there is only one plasma pattern for all the cells. The magnetic configuration could be produced using permanent NdFeB magnets or a permanent magnetic rubber (Plastimag®) which could be adapted to follow the desired pattern. The advantage of magnetic rubber is the easiness in the source assembly; on the other hand, however, NdFeB magnets have stronger magnetic proprieties and have a higher Curie temperature. Table 9-3 summarizes the proprieties of the two magnetic materials chosen for the magnetron assembly.

Table 9-3: Magnetic proprieties of used magnets.

Type	Remanence B_r [mT]	Coercivity H_cB [Oe]	Intrinscic Coercitivity H_cJ [Oe]	Max Temperature [°C]
MPN35EH	1210	11300	30000	200
Neorub 8	670	5500	11000	120

The selected NdFeB permanent magnet is MPN35EH; it was chosen for its high Curie temperature, indeed, it can work until 200 °C, and it has a strong magnetization, up to 1 T. However, ease of assembly given by Plastimag, has an effect on magnetization and Curie temperature, which are almost half, compared to the NdFeB.

At the same time, the material used as magnet support is Nylon 6, which has a working temperature between 40 and 100 °C (so compatible with water-cooling), has an excellent mechanical stability and it easy to machine. The Nylon 6 is used a substitute of PVC (used in previous magnetron design) for its higher T_g and for safety reasons, considering case of degradation (i.e. during water cooling fault) in Nylon 6 there is not chlorine inside that could produce dangerous gasses like HCl. In order to allow water-cooling of cathode and at the same time rotation, a particular top cathode support was designed. Figure 9.14 shows a rendering of the magnetron top flange. All these components were machine at LNL mechanical workshop. Figure 9.15 shows a picture of the final assembly. From the top is visible the rotating gear, the rotating feedthrough for rotation of the magnets and for water insulation, after that, the special aluminium components designed in order to water cool the magnetron with, visible water tubes already connected.

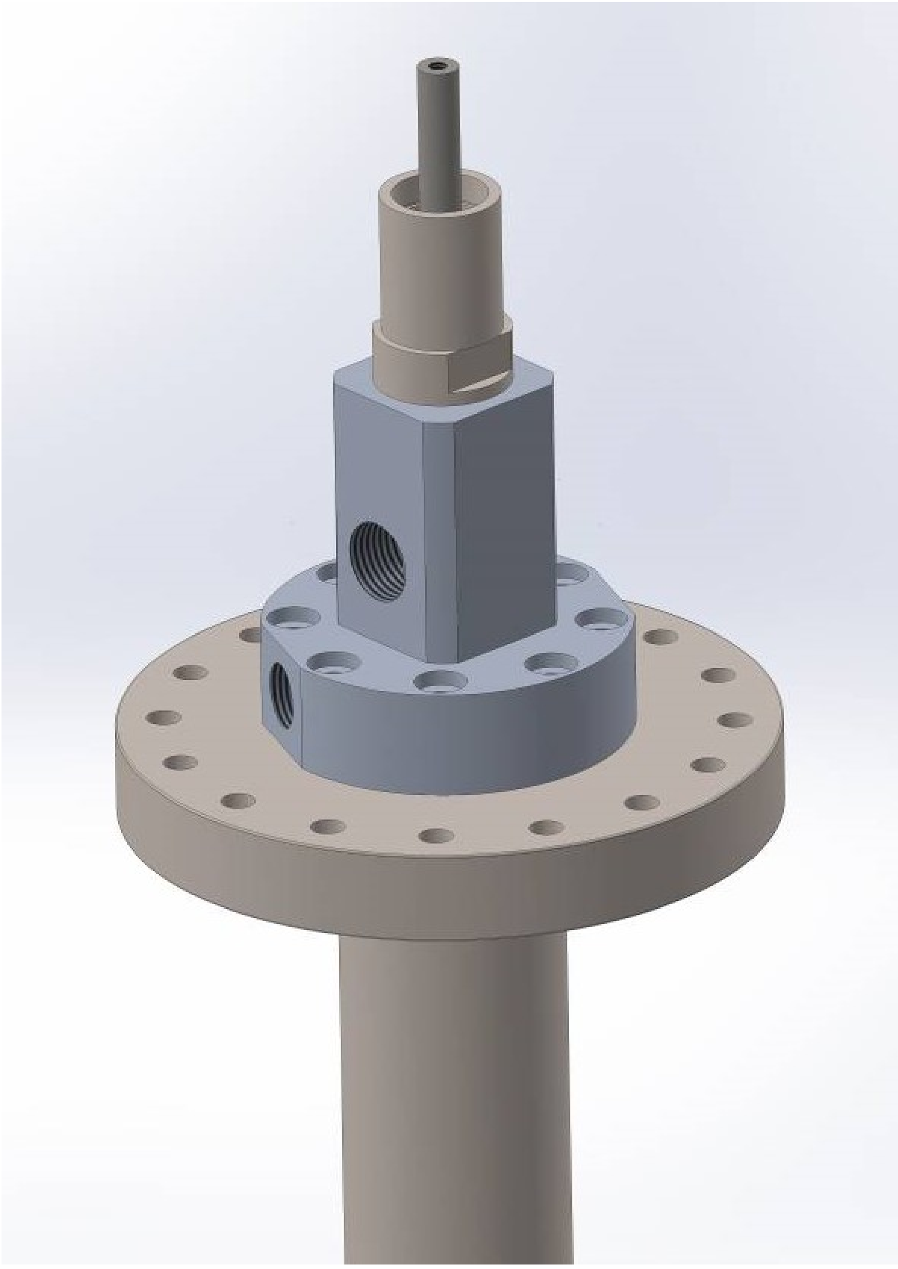

Figure 9.14: Rendering of the top magnetron flange. From the top is visible the rotating feedthrough that permits rotation of the magnets and at the same time water insulation, after the special aluminium components designed in order to water cool the magnetron.

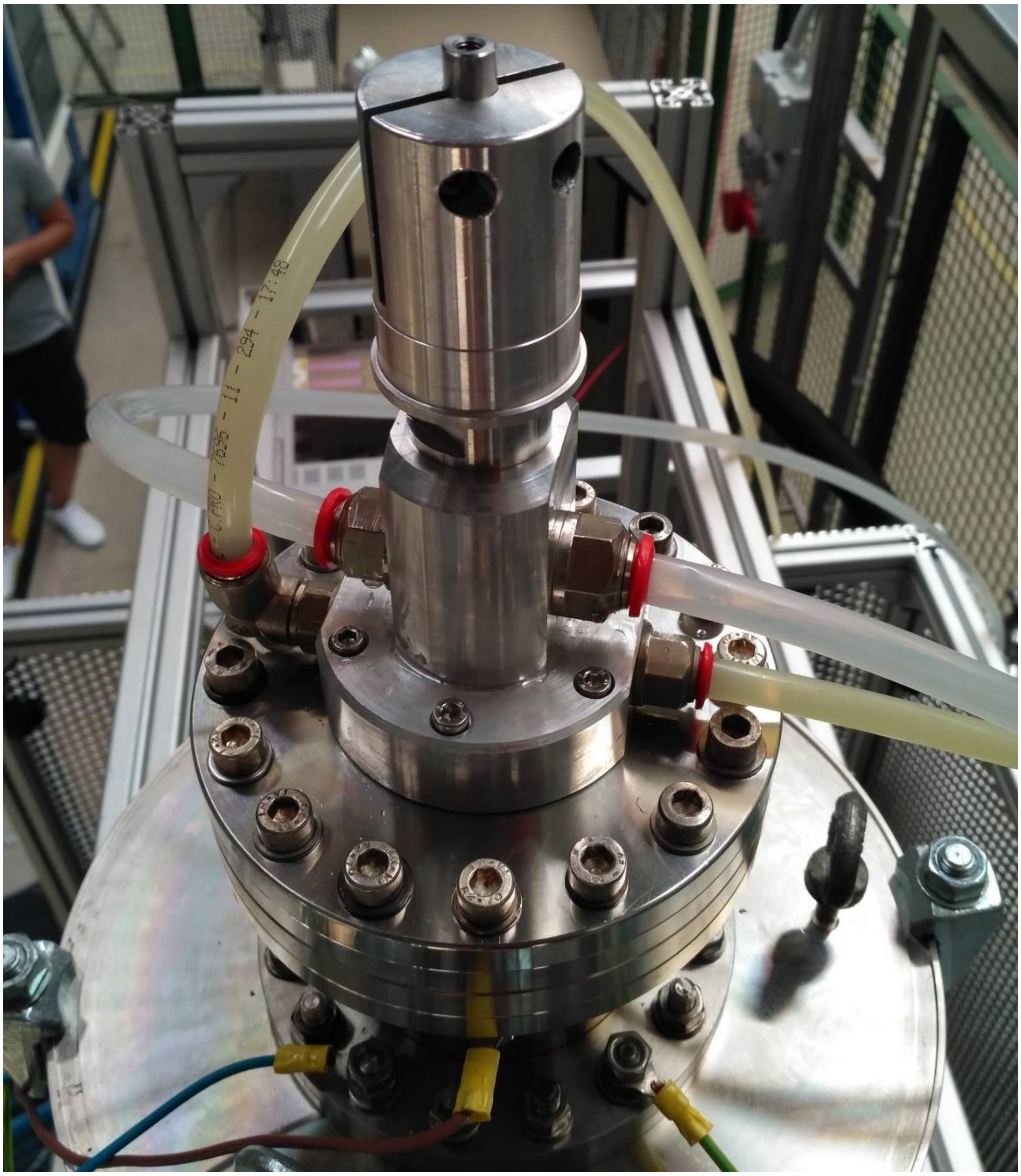

Figure 9.15: Picture of the top magnetron flange. From the top is visible the rotating gear, the rotating feedthrough that permits rotation of the magnets and at the same time water insulation, after the special aluminium components designed in order to water cool the magnetron with the water tubes connected.

This structure is assembled on a CF100 flange fixed on a standard CF100 ceramic feedthrough used to insulate the cathode (negative potential) from the ground.

Figure 9.16 shows a section of the whole sputtering configuration with the rotating magnet. Inside the cavity it is visible the Niobium cathode and inside it, the rotating magnet pack. The top ISO 250 flange is used for supporting the cavity through eight Stainless Steel rods with the possibility to bias it. The cavity is fixed to the rods by a circular centring ring that presses and supports it. The CF100 ceramic insulator that support the magnetron is also fixed to the top ISO 250 flange.

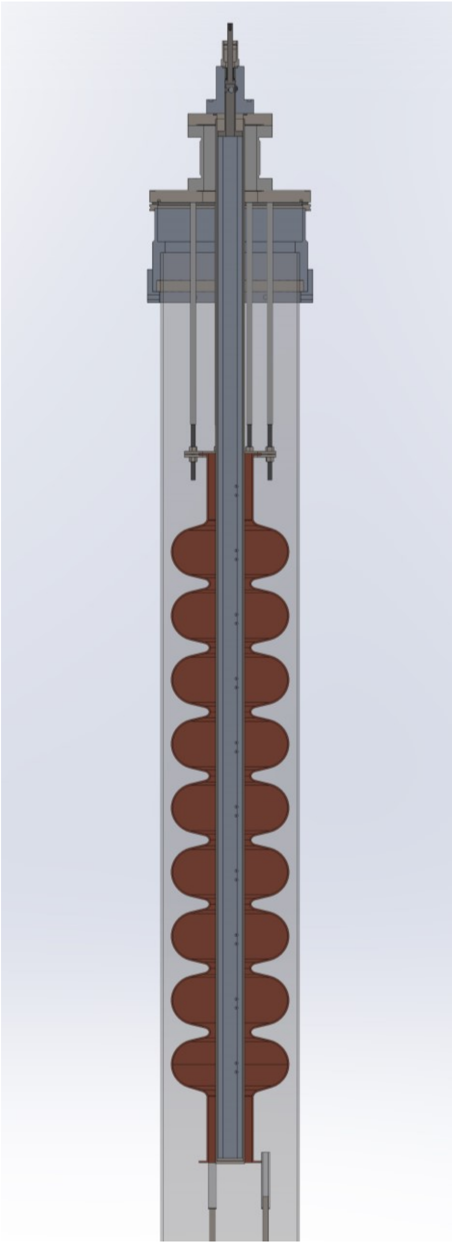

Figure 9.16: Rotating magnetron for 9-cell cavity. In the centre of the cavity is visible the Nb cathode with inside the water-cooled rotating magnet.

Figure 9.17 shows a rendering of the magnetic configuration. As anticipated before, it consists in a “spiral” made of cylindrical NdFeB magnets with 5 mm diameters and 8 mm high, fitted onto a Nylon 6 holed cathode holder. One side of the spiral is composed by north oriented magnets (red face), the other side by south oriented magnets (blue face). The magnetic field closes between the north and the south pole. The region between two cylindrical magnets, where magnetic field is parallel to the cathode surface, as discussed in paragraph 8.4, is the zone where plasma is more intense. Logically the rotation of the magnet pack guarantees a good target erosion and coating uniformity. There are 10 plasma horizontal regions (9 for the 9 cells of the cavity plus one for closing the magnetic confinements) visible on the central and right view of Figure 9.17. The regions are connected between them in order to guarantee continuity of plasma, by vertical plasma region (left and right views) and used also for sputtering cavity cut off. The top and bottom horizontal plasma region are connect between them to guarantee continuity of plasma region and not to lose electrons, through a vertical plasma region generated by the magnets visible on the rear parts of the magnet pack (right view onto Figure 9.17).

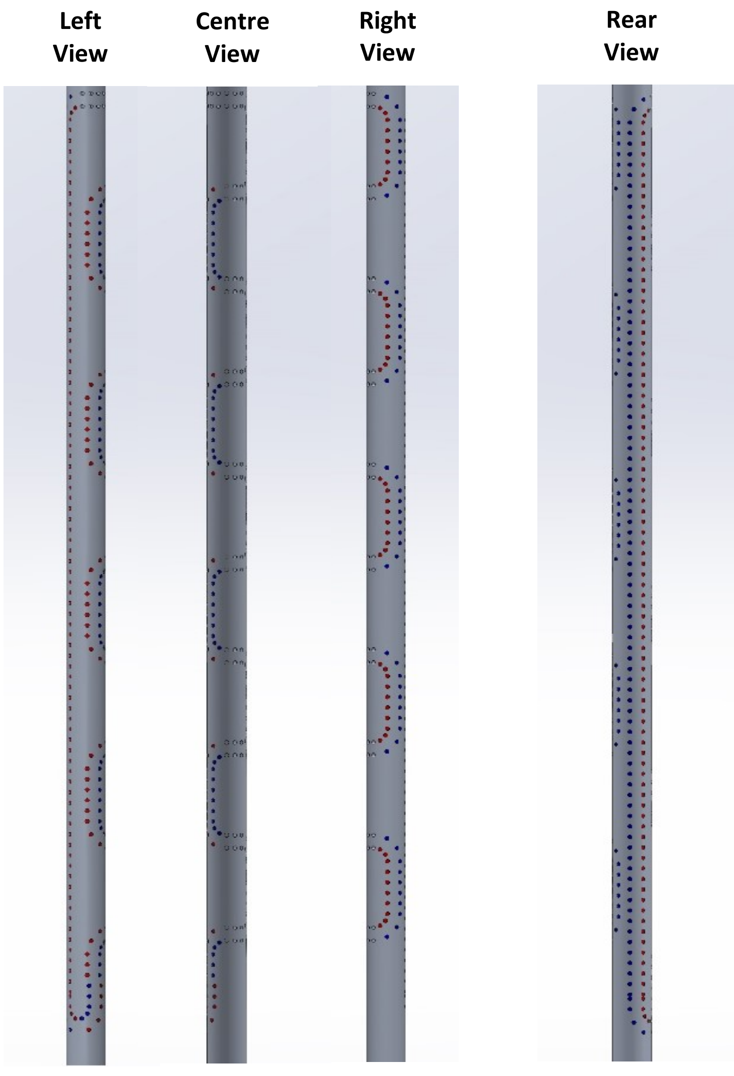

Figure 9.17: Rendering of Nylon magnets holder rotated. In red the north pole of magnet, in blue south pole.

The described “spiral” configuration permits to have a constant deposition rate along the whole cavity. There is in fact a higher cathode erosion rate in the cavity cell regions (horizontal region confinements) that corresponds to a high cavity/cathode surface ratio to be coated and low cathode erosion rate along cavity cut-off (vertical region confinements).

Machining (Figure 9.18) and assembly of the magnet pack was complex due to the need of drilling more than 500 holes and assembly 500 NdFeB magnets that compose it (Figure 9.19 shows the magnet pack assembled with all the magnets and ready to be inserted into the cathode).

The configuration that should be obtained using plastimag could be similar: there are no holes onto Nylon for magnets fixing, but an incision for housing the flexible magnet.

Figure 9.18: Machining of Nylon 6 magnets support.

After machining and assembly, the magnet pack was inserted into the cathode and fixed to the rotary mechanism already discussed in this chapter and visible in Figure 9.15.

For this set of tests, the cathode used is in Stainless Steel. This choice allows reducing costs respect to using Niobium and it permits to evaluate the plasma confinements and the deposition rate of the source. In Figure 9.20 is visible the source completely assembled and ready for insertion inside vacuum chamber.

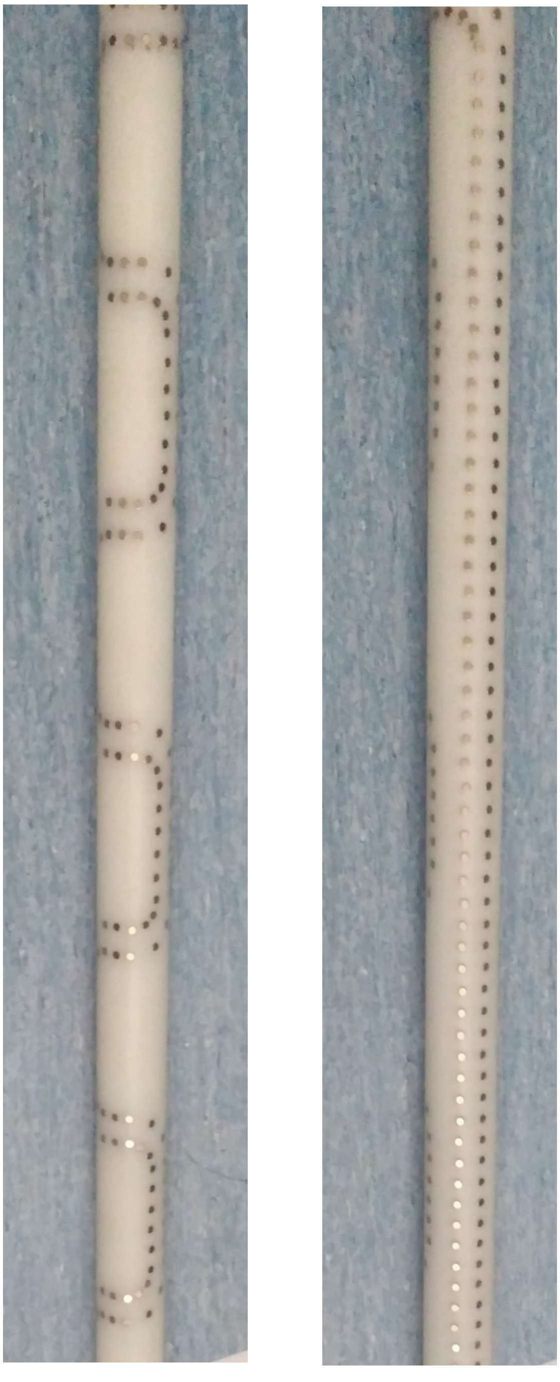

Figure 9.19: Nylon 6 magnet pack assembled. On left front view, on right rear view.

Figure 9.21 shows the plasma ignited inside the vacuum chamber. It is visible the “spiral” pattern generated by this innovative configuration. The sputtering parameters are summarised in

Table 9-4. In this test, the inductor is switched off because the magnetic field is generated by the permanent magnets and the induction will be used only for heating the cavity. The plasma is uniform along the 1.2 meter of the cathode and it makes a close path, fundamental aspect in order to produce a dense and confine plasma without electrons losses.

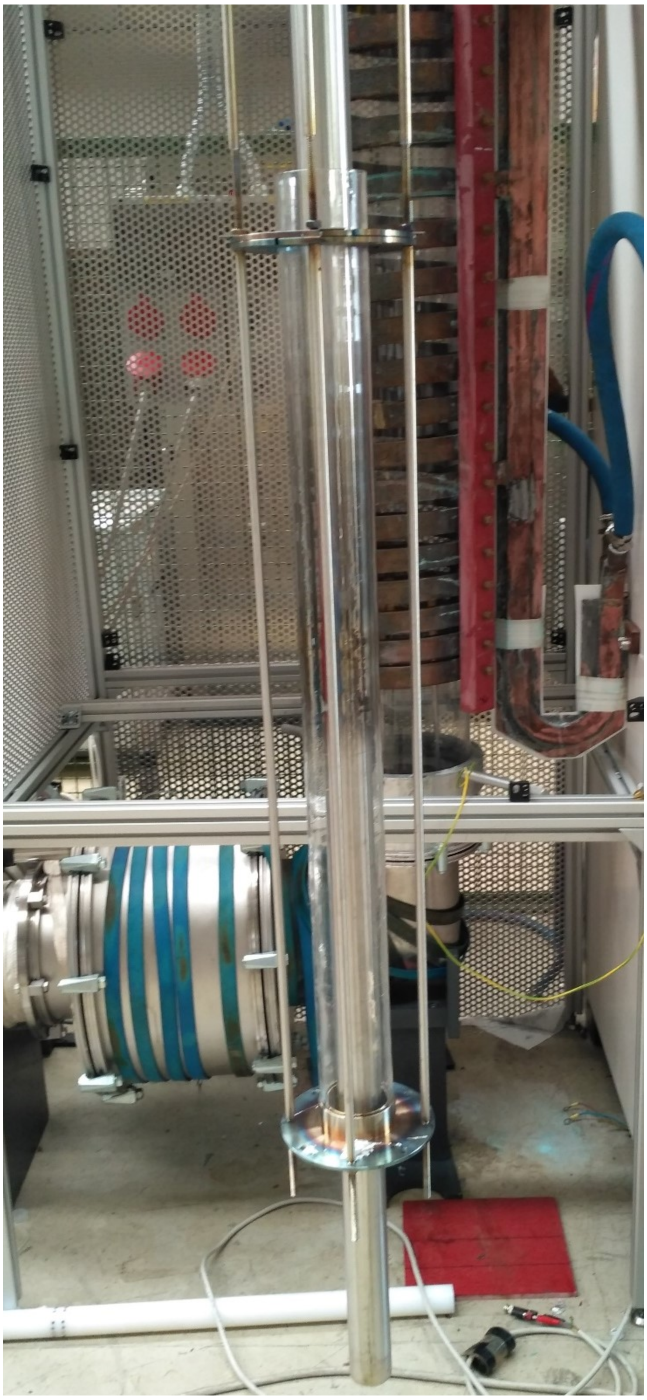

Figure 9.20: Cathode assembled and ready for insertion inside the quartz vacuum chamber. The four SS roods are used to support a quartz tube in order to protect the quartz chamber tube from deposition and, at the same time, to observe the plasma along the cathode.

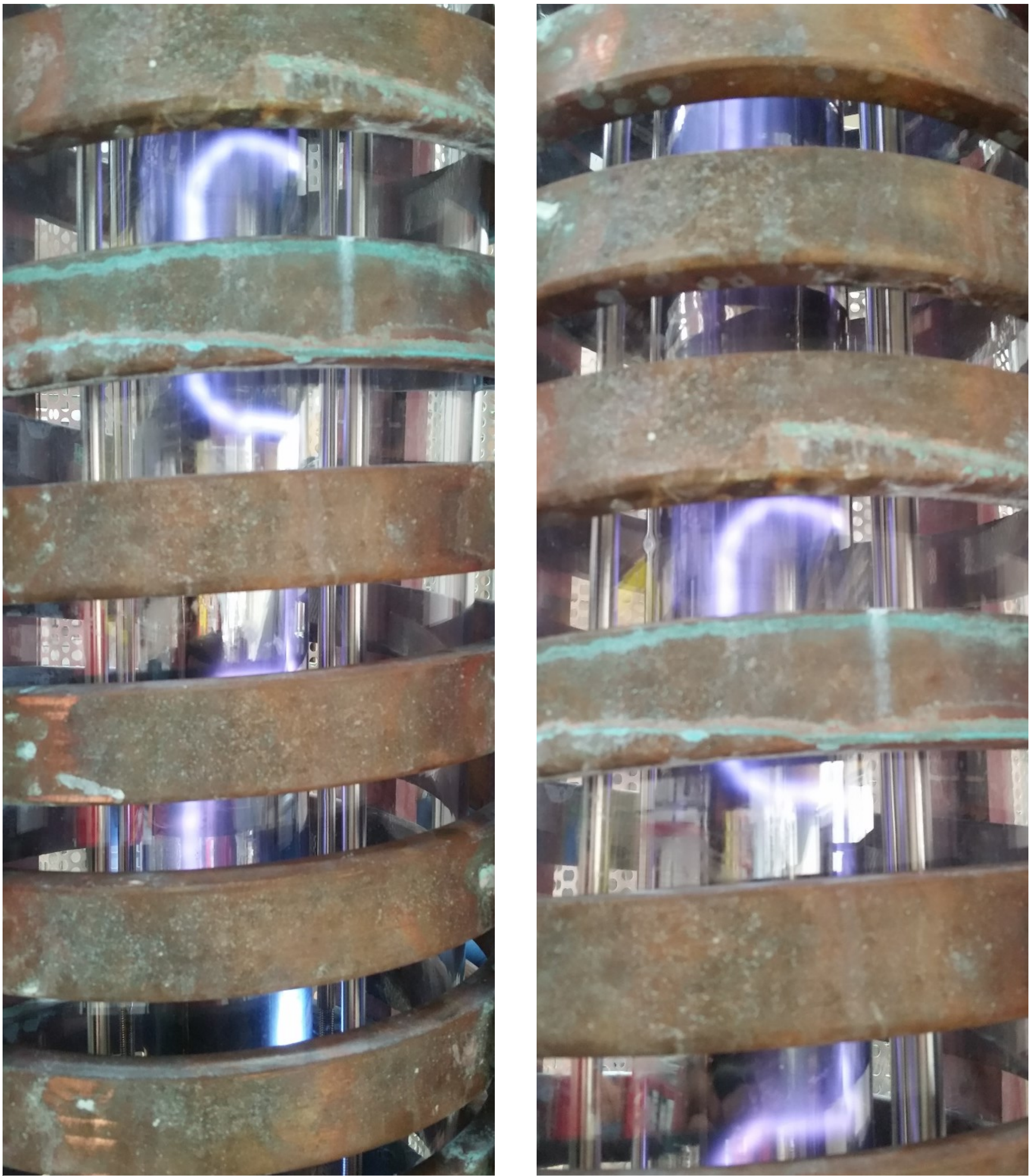

Figure 9.21: Two different views of the plasma inside the vacuum chamber during preliminary test.

Table 9-4: Sputtering parameters during test with rotating magnets.

Parameter	Value
Sputtering Tension	540 V
Sputtering Current	1.6 A
Sputtering Power	864 W
Inductor Tension	OFF
Inductor Current	OFF
Inductor Frequency	OFF
Inductor Power	OFF
Sputtering Ar pressure	$5\cdot10^{-2}$ mbar

9.5 Magnetron choice

In the precedent paragraphs, we consider different magnetron configurations suitable for 9-cell cavities. All the configurations are new and innovative, except for the *Mobile magnetron assembled onto feedthrough,* corresponding to the first configuration analysed (paragraph 9.2). Until now, there are no reports about induction heating and neither in a magnetron sputtering configuration that uses the magnetic field generated by the induction heating, to confine the plasma on the Niobium cathode surface. Undoubtedly, a configuration that, allows to heat and to generate the plasma simultaneously is certainly innovative. Unfortunately our induction system has not the possibility to change working frequency, so with our configuration (Copper cavity with 2 mm thickness and heating frequency of 8 kHz) the penetration depth is 0.73 mm, so the magnetic field calculated inside the cavity that could generate the plasma is only 1.2 G, insufficient to sustain the discharge. Using inductor facility at its maximum power (500 A), the magnetic field generated by the inductance will be 110 G that, with the copper cavity shielding, is 7.1 G @8 kHz in the magnetron region. With this assumption it is easy to understand that, if we want to follow this path, we must to modify inductor working frequency and we must to introduce a system capable to modify the frequency in function of the process (now the frequency is automatically tuned in function of heating load). Such modification is suggested as a further work in this research field; it is no longer possible to evaluate it for the purposes of this research taking into account the cost, testing and time needed to develop it. Moreover, it is important to note the limits of the custom purchase and experimental variables i.e. the remarkable delays on the delivery of the inductor and the quartz tube crack that constrain the scope of this study.

Considering the results of the tests performed on the system in the last moths, the “Fixed magnetron with rotary magnets” (Paragraph 9.4) is the most promising and reliable configuration that allows to coat simultaneously a 9 cells cavity with a high temperature of the substrate, heating generated by induction oven.

Chapter 10

Conclusions & Further Works

10.1 Conclusions

The main purpose of this work was the design, construction and implementation of an innovative sputtering apparatus assisted by an induction system for the coating of Tesla type 1.5 GHz elliptical 9-cell cavities.

Several approaches were studied in order to improve the sputtered niobium film properties:

- Heating the cavity during sputtering, in order to increase the adhesion between coating and substrate, using an innovative induction system capable to heat the cavity from outside the vacuum chamber without reducing vacuum performance nor introducing contaminants.
- Study different cathode design for promoting Niobium atoms impinging perpendicularly the substrate surface for enhancing the superconductive properties of the film.
- Promoting the effect of plasma bombardment of the growing film in order to remove impurities weakly bonded to the surface by implementing, during the system design, the possibility to bias the cavity during coating.

Mechanical and thermal simulations were performed for designing the sputtering system, using both: 3D design software and finite element software. Such approach allows verifying the performance of the various components and the proper design for sustaining the mechanical and thermal stress. The mechanical machining and the production of vacuum components was monitored at the different workshops. The corresponding vacuum tests were done.

Based on the results of the design study, the commissioning and acceptance test of the Polycold system was carried out. This step guarantee the proper performance of the vacuum system, for production of Niobium cavity by sputtering.

In the other hand, the production and commissioning of the induction heating system were carried out, including also solving the problems emerged during tests by the manufacturer. The details of the process are summarized in paragraph 6.6.3.

A fundamental part of this research work, was the design of the different sputtering sources. For this purpose, different magnetron sputtering configurations were designed and built. Chapter 9 analyse in details all the configurations studied, designed, assembled and tested.

At the end of the tests, the most promising configuration is a “Fixed magnetron with rotary magnets” (9.4). The setup consists in a fixed cylindrical cathode with inside a rotating magnet pack. The innovation is introduced in the production of the new magnet pack that has more than 1000 magnets fixed onto a Nylon 6 support. The magnets position produce the plasma with a “spiral” shape. The configuration has 10 plasma horizontal region, used for coating the 9-cavity cells (plus one for closing magnetic confinement). The horizontal regions are connected between them by vertical plasma region for cut-off coating and to guarantee plasma continuity. A long vertical region (1.2 m) connects the top and bottom plasma region for guarantee plasma continuity. The tests on this source are promising; the plasma is uniform along the whole cavity length.

10.2 Further work

Several steps can be consider for continuing this research line. First, continuing the test on the built magnetron sources. A more in-depth study for defining the final configuration. The study of deposition rate, relation of coating performance and magnet pack rotation frequency, Ar pressure during coating and cavity temperature is mandatory.

After such studies, a characterization of the sputtering source will allow to define the best sputtering parameters, such as pressure and power, as well as the optimal cavity heating temperature. For this purposes, samples deposited onto quartz substrates can be evaluated with the corresponding technical analyses such as thickness measurements, X-Ray diffraction analysis, SEM imaging and superconductive proprieties measurements of samples.

This programmed steps lead to obtain the setting of the magnetron sputtering parameters and configuration, necessary to deposit a uniform thin film with good superconductive properties onto TESLA type 9-cell elliptical cavity.

Appendix A

Penetration Depth of Nonmagnetic Metals (mm)

	T		ρ		Frequency (kHz)										
Metal	°C	°F	μΩ · m	μΩ · in.	0.06	0.50	1	2.5	4	8	10	30	70	200	500
Aluminum	20	68	0.027	1.06	10.7	3.70	2.61	1.65	1.30	0.92	0.83	0.48	0.31	0.18	0.12
	250	482	0.053	2.09	15.0	5.18	3.66	2.32	1.83	1.29	1.16	0.67	0.44	0.26	0.16
	500	932	0.087	3.43	19.2	6.64	4.69	2.97	2.35	1.66	1.48	0.86	0.56	0.33	0.21
Copper	20	68	0.018	0.71	8.81	3.05	2.16	1.36	1.08	0.76	0.68	0.39	0.26	0.15	0.10
	500	932	0.050	1.97	14.5	5.03	3.56	2.25	1.78	1.26	1.12	0.65	0.43	0.25	0.16
	900	1,652	0.085	3.35	19.3	6.67	4.72	2.98	2.36	1.67	1.49	0.86	0.56	0.33	0.21
Brass	20	68	0.065	2.56	16.6	5.74	4.06	2.56	2.03	1.43	1.28	0.74	0.48	0.29	0.18
	400	752	0.114	4.49	21.9	7.60	5.37	3.40	2.69	1.90	1.70	0.98	0.64	0.38	0.24
	900	1,632	0.203	7.99	29.3	10.1	7.17	4.53	3.58	2.53	2.27	1.31	0.86	0.51	0.32
Stainless steel	20	68	0.690	27.2	53.9	18.7	13.2	8.36	6.61	4.67	4.18	2.41	1.58	0.93	0.59
	800	1,472	1.150	45.3	69.6	24.1	17.1	10.8	8.53	6.03	5.39	3.11	2.04	1.21	0.76
	1,200	2,192	1.240	48.8	72.3	25.1	17.7	11.2	8.86	6.26	5.60	3.23	2.12	1.25	0.79
Silver	20	68	0.017	0.67	8.34	2.89	2.04	1.29	1.02	0.72	0.65	0.37	0.24	0.14	0.09
	300	572	0.038	1.50	12.7	4.39	3.10	1.96	1.55	1.10	0.98	0.57	0.37	0.22	0.14
	800	1,472	0.070	2.76	17.2	5.95	4.21	2.66	2.10	1.49	1.33	0.77	0.50	0.30	0.19
Tungsten	20	68	0.050	1.97	14.5	5.03	3.56	2.25	1.78	1.26	1.12	0.65	0.43	0.83	0.53
	1,500	5,072	1.550	21.7	48.2	16.7	11.8	7.46	5.90	4.17	3.73	2.15	1.41	0.83	0.53
	2,800	5,072	1.040	40.9	66.2	22.9	16.2	10.3	8.11	5.74	5.13	2.96	1.94	1.15	0.73
Titanium	20	68	0.500	19.7	45.9	15.9	11.3	7.11	5.62	3.98	3.56	2.05	1.34	0.80	0.50
	600	1,112	1.400	55.1	76.8	26.6	18.8	11.9	9.41	6.65	5.95	3.44	2.25	1.33	0.84
	1,200	2,192	1.800	70.9	87.1	30.2	21.3	13.5	10.7	7.54	6.75	3.90	2.55	1.51	0.95

Appendix B

Buckling simulation report

INFN
Viale Università 2 35020 Legnaro
Phone: 049-8068664

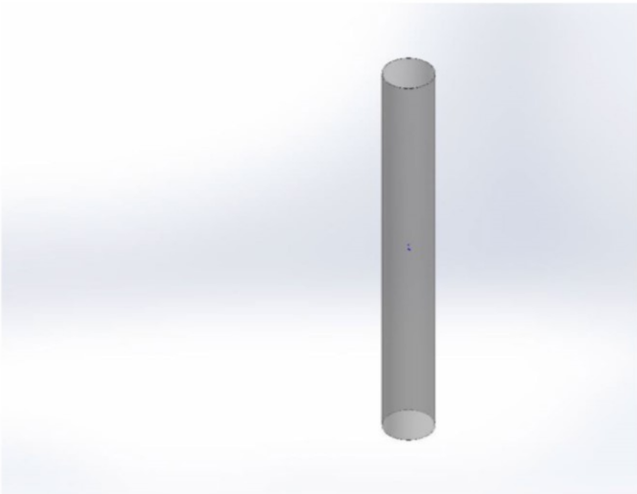

Simulation of Quartz

Date: venerdì 20 gennaio 2017
Designer: G. Keppel
Study name: Carichi di punta
Analysis type: Buckling

Table of Contents

Description

No Data

INFN
Viale Università 2 35020 Legnaro

G. Keppel
20/01/2017

Presupposti

Informazioni sul modello

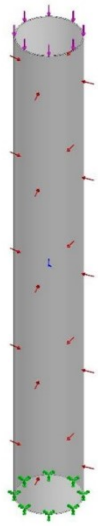

Model name: Quartz-1
Current Configuration: Default

Solid Bodies			
Document Name and Reference	**Treated As**	**Volumetric Properties**	**Document Path/Date Modified**

INFN
Viale Università 2 35020 Legnaro

G. Keppe
20/01/201

Rivoluzione1 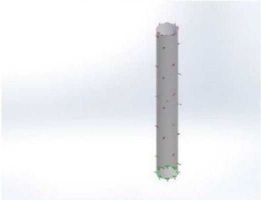	Solid Body	**Mass:16.9332 kg Volume:0.0076969 m^3 Density:2200 kg/m^3 Weight:165.945 N**	**D:\Utenti\Giorgio\Progetti \Induttore Ricottura tubi Nb\Solidworks\Quartz-1.sldprt** Jan 19 11:43:59 2017

Proprietà studio

Study name	Carichi di punta
Analysis type	Buckling
Mesh type	Solid Mesh
Number of modes	1
Solver type	FFEPlus
Incompatible bonding options	Automatic
Thermal Effect:	On
Thermal option	Include temperature loads
Zero strain temperature	298 Kelvin
Include fluid pressure effects from SOLIDWORKS Flow Simulation	Off
Soft Spring:	Off
Result folder	SOLIDWORKS document (D:\Utenti\Giorgio\Progetti\Induttore Ricottura tubi Nb\Solidworks)

Unità

Unit system:	SI (MKS)
Length/Displacement	mm
Temperature	Kelvin
Angular velocity	Rad/sec
Pressure/Stress	N/mm^2 (MPa)

INFN
Viale Università 2 35020 Legnaro

G. Keppel
20/01/2017

Proprietà materiale

Model Reference	Properties	Components
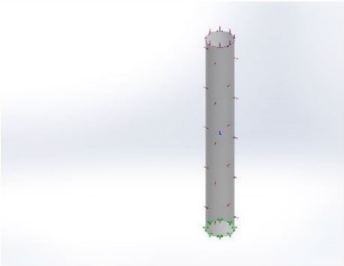	**Name:** Quarzo **Model type:** Linear Elastic Isotropic **Default failure criterion:** Mohr-Coulomb Stress **Tensile strength:** 47 N/mm^2 **Mass density:** 2200 g/cm^3 **Elastic modulus:** 70000 N/mm^2 **Poisson's ratio:** 0.17 **Thermal expansion coefficient:** 5.5e-007 /Kelvin	CorpoSolido 1(Rivoluzione1)(Quartz-1)
Curve Data:N/A		

INFN
Viale Università 2 35020 Legnaro

G. Keppel
20/01/2017

Informazioni relative al mesh

Mesh type	Solid Mesh
Mesher Used:	Standard mesh
Automatic Transition:	Off
Include Mesh Auto Loops:	Off
Jacobian points	4 Points
Element Size	17.5683 mm
Tolerance	0.878416 mm
Mesh Quality	High

Mesh information - Details

Total Nodes	60032
Total Elements	29937
Maximum Aspect Ratio	12.188
% of elements with Aspect Ratio < 3	7.98
% of elements with Aspect Ratio > 10	0.0234
% of distorted elements(Jacobian)	0
Time to complete mesh(hh;mm;ss):	00:00:09
Computer name:	LSC99

INFN
Viale Università 2 35020 Legnaro

G. Keppel
20/01/2017

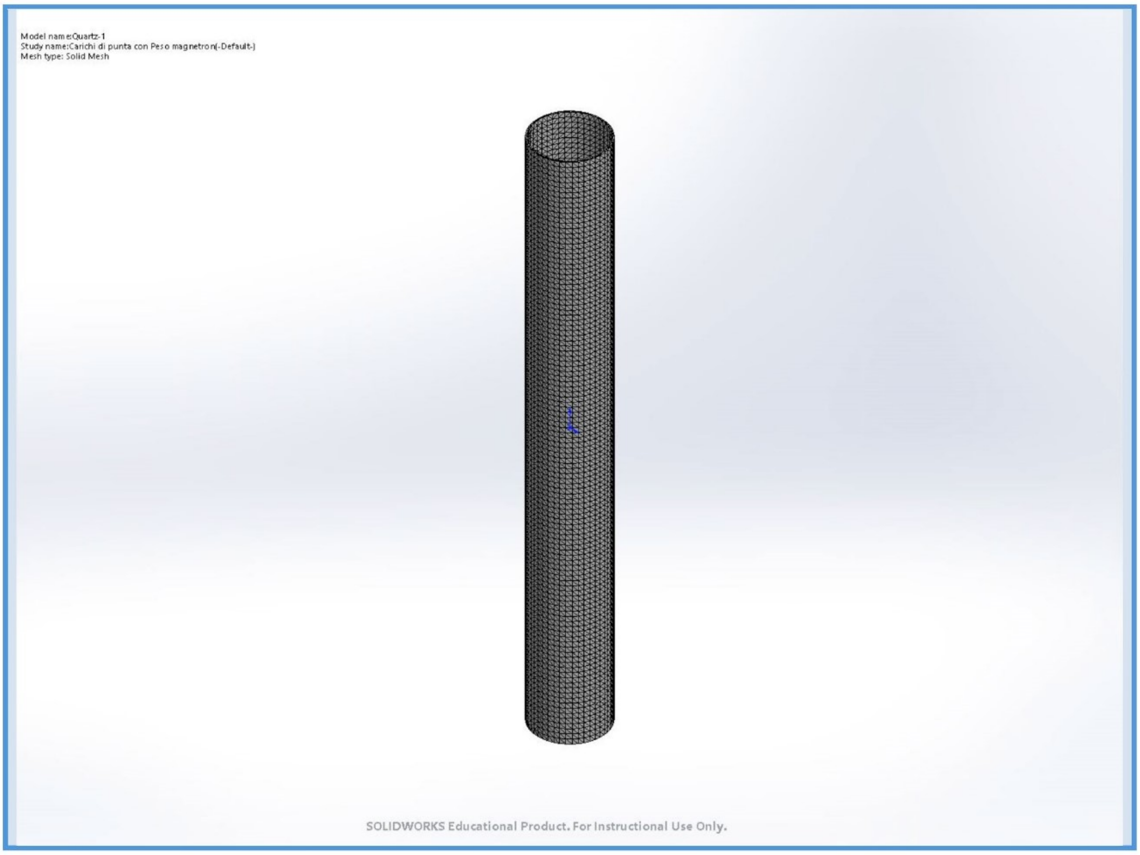

Dettagli sensore

No Data

INFN
Viale Università 2 35020 Legnaro

G. Keppel
20/01/2017

Risultati studio

Name	Type	Min	Max
Ampiezza1	AMPRES: Resultant Amplitude Plot for Mode Shape: 1(Load Factor = 15.8574)	0 Node: 1	0.00222192 Node: 1859

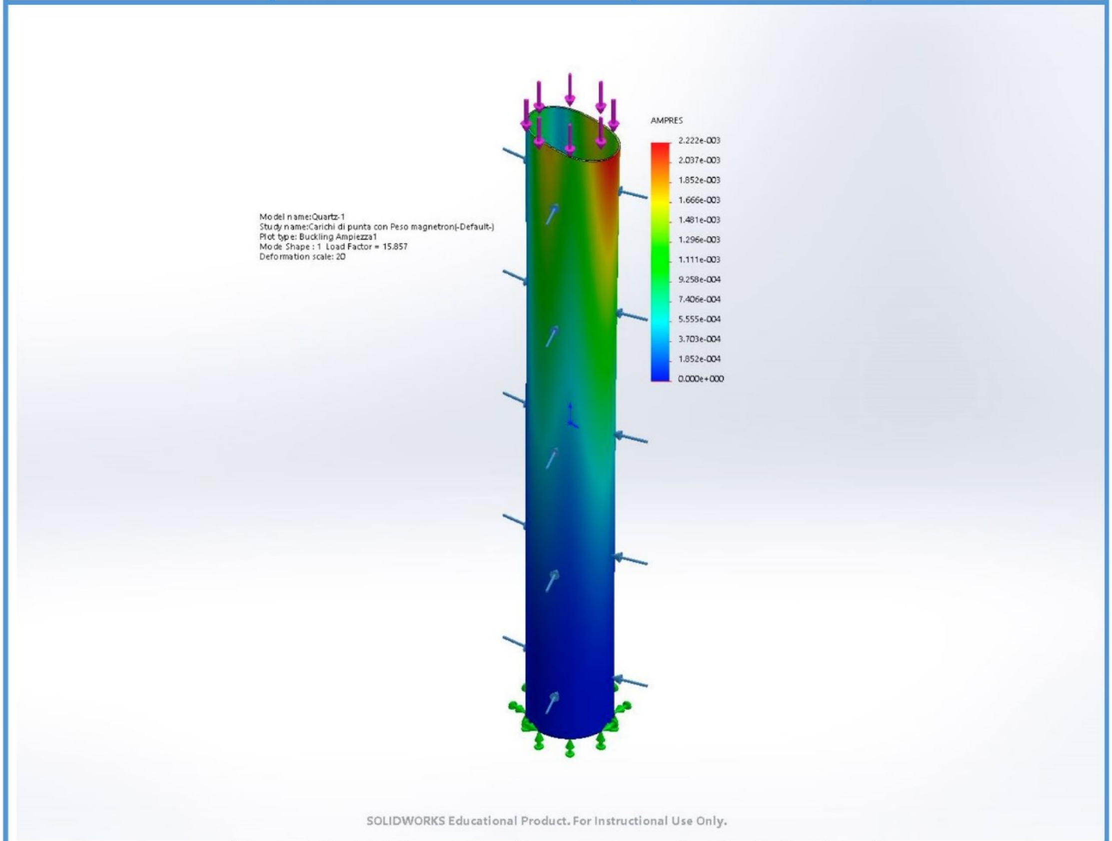

Quartz-1-Carichi di punta con Peso magnetron-Amplitude-Ampiezza1

Name	Type
Spostamento1	AMPRES: Resultant Amplitude

INFN
Viale Università 2 35020 Legnaro

G. Keppel
20/01/2017

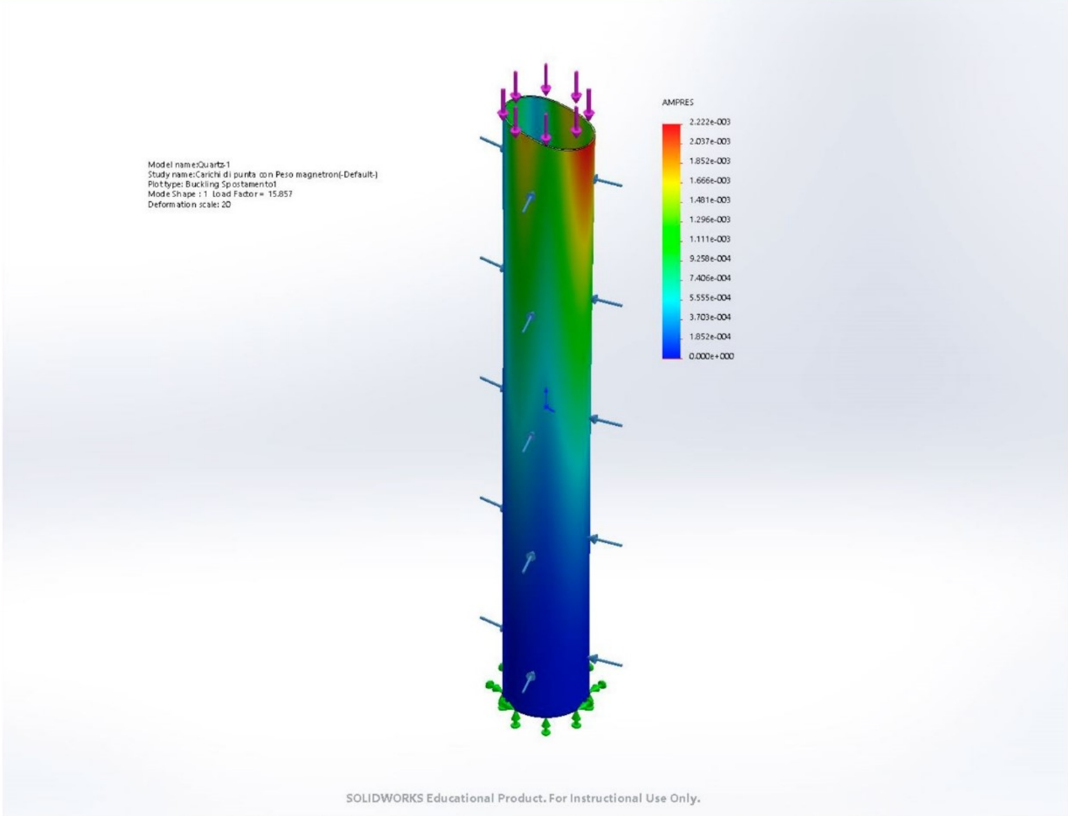

Quartz-1-Carichi di punta con Peso magnetron-Displacement-Spostamento1

Mode List

Mode Number	Load Factor
1	15.857

Bibliography

[1] H. Padamsee, RF Superconductivity for Accelerators, New York: John Wiley & Sons, 1998.

[2] CERN, “How acellerator works,” [Online]. Available: http://home.web.cern.ch/about/how-accelerator- works. [Accessed 06 12 2016].

[3] L. Suelzle, “Progress on RF electron superconducting accelerators,” in *Proceeding Accelerator Conference 1973*, Standford, California, 1973.

[4] R. e. a. Brinkmann, “TESLA Technical Design Report – Part II: The Accelerator,” 03 2001. [Online]. Available: http://tesla.desy.de/new_pages/TDR_CD/PartII/accel.html. [Accessed 30 01 2017].

[5] Y. S. Derbenev, A. M. Kondratenko and E. L. Saldin, “On the possibility of using a free electron laser for polarization of electrons in storage rings,” *Nucl. Instr. Meth. Phys. Res.,* vol. 193, no. 3, pp. 415-421, 1982.

[6] R. Brinkmann, “Accelerator Layout Of The X-FEL,” in *Proceedings of LINAC*, Lübeck,, 2004.

[7] “ITRP Report,” 09 2004. [Online]. Available: http://icfa.fnal.gov/wp-content/uploads/ITRP_Report_Final.pdf. [Accessed 30 01 2017].

[8] T. Behnke and et al., “ILC Technical Design Report: Volume 1 - Executive Summary,” 2013. [Online]. Available: http://www.linearcollider.org/ILC/Publications/Technical-Design-Report. [Accessed 07 12 2013].

[9] N. A. Tahir and et al., “Beam Induced Hydrodynamic Tunneling in the Future Circular Collider Components,” *Physical Review Accelerators and Beams,* vol. 19, no. 081002, 2016.

[10] L. M. Bollinger, “Low β SC Linacs: Past, Present and Future,” in *Proceeding of the XIX LINAC Conference*, Chicago, IL, USA, 1998.

[11] I. Ben-Zvi and J. M. Brennan, “The quarter wave resonator as a superconducting linac element,” *Nuclear Instruments and Methods in Physics Research,* vol. 212, no. 1-3, pp. 73-79, 1983.

[12] L. M. Bollinger and et al., “First operational experience with the positive-ion injector of ATLAS,” *Nucl. Instr. Meth. Phys. Res. A,* vol. 328, no. 1-2, pp. 221-230, 1993.

[13] S. Takeuchi and et al., “Status of the JAERY Tandem Accelerator and Its Booster,” in *Proc. of the 8th HIAT Conference*, Argonne, USA, 1998.

[14] A. M. Porcellato and et al., “Niobium Sputterd QWRs,” in *Proceedings of 12th International Workshop on RF Superconductivity*, Ithaca, New York, USA, 2005.

[15] M. J. G. Borge, “Highlights of the ISOLDE facility and the HIE-ISOLDE project,” *Nucl. Instr. Meth. Phys. Res. B,* vol. 376, pp. 408-412, 2016.

[16] CERN, “REX-ISOLDE SC Linac,” [Online]. Available: http://rex-isolde.web.cern.ch/sc-linac. [Accessed 13 12 2016].

[17] M. Leitner and et al., “The FRIB project at MSU,” in *Proceedings of the 16th International Workshop on RF Superconductivity*, Paris, France, 2013.

[18] A. Facco and et al., “Superconducting resonators development for the FRIB and REA LINACs at MSU: Recent achievements and future goals,” in *Proceedings of 3rd International Particle Accelerator Conference*, New Orleans, LA, United States, 2012.

[19] H. J. Kim, “Progress on superconducting LINAC for the raon heavy Ion accelerator,” in *Proceedings of the 7th International Particle Accelerator Conference*, Busan, Korea, 2016.

[20] D.-O. Jeon and et al., “Status Of The RAON Accelerator Systems,” in *Proceedings of the 4th International Particle Accelerator Conference*, Shanghai, China, 2013.

[21] R. Edinger and et al., “Technology Readiness Levels Applied To Current Srf Accelerator Technology For ADS,” in *Proceedings of SRF2015*, Whistler, BC, Canada, 2015.

[22] J. L. Biarrotte and et al., “Accelerator reference design for the MYRRHA European ADS demonstrator,” in *Proceedings of 25th International Linear Accelerator Conference,*, Tsukuba, Japan, 2010.

[23] F. Shinian, F. Shouxian and W. Jiuqing, “Proton Linac For Ads Application In China,” in *Proceedings of 25th Linear Accelerator Conference*, Tsukuba, Japan, 2010.

[24] A. W. Chao and W. Chou, Reviews of Accelerator Science and Technology: Volume 5: Applications of Superconducting Technology to Accelerators, World Scientific Pub Co Inc, 2012.

[25] S. Henderson, “Commisioning and Intial operating experience with the SNC 1 GeV LINAC,” in *Proceedings of the 23th International Linear Accelerator Conference*, Knoxville, USA, 2006.

[26] H. Padamsee, J. Knobloch and T. Hays, RF Superconductivity for Accelerators, San Diego: John Wiley & Sons, 1998.

[27] H. Padamsee, “The science and technology of superconducting cavities for accelerators,” *Superconductor Science and Technology,* vol. 14, no. 4, pp. 28-51, 2001.

[28] P. Kneisel, R. Vincon and J. Halbritter, “First results on elliptically shaped cavities,” *Nucl. Instr. Meth. Phys. Res.,* vol. 188, no. 3, pp. 669-670, 1981.

[29] U. Klein and D. Proch, “Multipacting in superconducting RF structures,” in *Proc. Conf. Future, possibilities for Electron Accelerators*, Charlottesville, VA, 1979.

[30] C. C. Compton and et al., “Prototyping of a multicell superconducting cavity for acceleration of medium-velocity beams,” *Phys. Rev. ST Accel. Beams,* vol. 8, no. 042003, 2005.

[31] K. W. Shepard and et al., “Prototype 350 MHz, niobium spoke-loaded cavities,” in *Proceeding Particle Accelerator Conference*, New York, NY, 1999.

[32] R. Bailey, Superconductivity for Accelerators, CERN, Geneva: Proceedings of the CAS–CERN Accelerator School, 2014.

[33] A. Facco, “Tutorial on low beta cavity design,” in *Proceeding of 12th Workshop on RF Superconductivity*, Ithaca, NY, 2005.

[34] G. Devanz, “SPIRAL 2 resonators,” in *Proceeding of 12th Workshop on RF Superconductivity*, Ithaca, NY, 2005.

[35] P. N. Ostroumov and K. W. Shepard, “Correction of beam-steering effects in low-velocity superconducting quarter-wave cavities,” *Phys. Rev. ST Accel. Beams,* vol. 4, no. 110101, 2001.

[36] G. Barbato, “Electrodeposition of tantalum and niobium using ionic liquid,” University of Toronto, Toronto, 2009.

[37] H. Padamsee, RF Superconductivity: Science, Technology and Applications, New York: John Wiley & Sons, 2009.

[38] L. Catani, “Deposition and Characterisation of Niobium Films for SRF Cavity Application,” in *EUROCON 2007 - The International Conference on "Computer as a Tool"*, Warsaw, Poland, 2007.

[39] W. T. Singer and et al., “Hydroforming of elliptical cavities,” *Phys. Rev. ST Accel. Beams,* vol. 18, no. 022001, 2015.

[40] V. Palmieri, “Fundamentals of electrochemistry-the electrolytic polishing of metals: application to copper and niobium,” in *Proceedings of 11th Workshop on RF Superconductivity*, Lübeck, Germany, 2003.

[41] V. Palmieri, “Advancements on Spinning of Seamless Multicell Reentrant Cavities,” in *Proceedings of 11th Workshop on RF Superconductivity*, Lübeck, Germany, 2003.

[42] V. Palmieri, “Progress on Spun Seamless Cavities,” in *Proceedings of 12th Workshop on RF Superconductivity,*, Ithaca, NY, USA, 2005.

[43] W. Singer and et al., “Hydroforming of superconducting tesla cavities,” in *Proceedings of 10th Workshop on RF Superconductivity*, Tsukuba, Japan, 2001.

[44] K. Saito and et al., “R&D of Nb/Cu clad seamless cavities at KEK,” in *Proceedings of 10th Workshop on RF Superconductivity*, Tsukuba, Japan, 2001.

[45] T. Fujino, “Promising Performance of the Nb/Cu Clad Seamless Superconducting RF Cavities,” in *Proceeding of the 9th Workshop on RF Superconductivity*, Santa Fe, New Mexico, USA, 1999.

[46] K. Hübner, “The LEP Superconducting RF System,” in *Proceedings of Snowmass*, Snowmass Village, Colorado, 2001.

[47] E. Chiaveri, “The CERN Nb/Cu Programme for the LHC and Reduced-β Superconducting Cavities,” in *Proceedings of the 9th Workshop on RF Superconductivity*, Santa Fe, New Mexico USA, 1999.

[48] G. Bisoffi and et al., “ALPI QWR and S-RFQ operating experience,” in *Proceedings of the 13th Workshop on RF Superconductivity*, Beijin, China, 2007.

[49] G. Fortuna and et al., “Completion of the First Phase and Studies for the Upgrading of the ALPI Project at LNL,” in *Proceeding of 3rd European Particle Accelerator Conference*, Berlin, Germany, 1992.

[50] R. McHenry, The New Encyclopedia Britannica 3, 15 ed., Chicago: Encyclopaedia Britannica, Incorporated, 2005.

[51] Y. Wang, Fundamental Elements Of Applied Superconductivity In Electrical Engineering, Hoboken, New Jersey, USA: John Wiley & Sons, 2013.

[52] J. Bardeen, L. Cooper and J. R. Schrieffer, “Theory of superconductivity,” *Physical Review,* vol. 108, no. 5, p. 1175, 1957.

[53] A. B. Pippard, “Field Variation of the Superconducting Penetration Depth,” in *Proceeding of the Royal Society A*, London, 1950.

[54] J. Waldram, “Surface Impedance of Superconductors,” *Advances in Physics,* vol. 13, no. 49, pp. 1-88, 1964.

[55] A. Barone, European Training on Technologies and Industrial Applications of Superconductivity, 1992, pp. 224-255.

[56] B. Aune and et al., “Superconducting TESLA cavities,” *Phys. Rev. ST Accel. Beams,* vol. 3, no. 092001, 2000.

[57] J. J. Hanak and et al., “Preparation and properties of vapor-deposited niobium stannide,” *RCA Review,* vol. 25, no. 3, pp. 342-365, 1964.

[58] B. Bonin, “Materials For Superconducting Cavities,” CERN, Geneve, 1995.

[59] V. Palmieri, “The Problem Of Q-Drop In Superconducting Resonators Revised By The Analysis Of Fundamental Concepts From Rf-Superconductivity Theory,” in *Proceedings of the 12th International Workshop on RF Superconductivity*, Ithaca, New York, USA, 2005.

[60] P. Bosland and et al., “Preparation and RF tests of L-band superconducting niobium-coated copper cavities,” *IEEE Transactions on Applied Superconductivity,* vol. 9, no. 2, pp. 896-899, 1999.

[61] P. Bauer and et al., “A Collection of Selected High Field Q-Slope Studies, Models and Comments,” 2006.

[62] B. Bonin and H. Safa, “Power dissipation at high fields in granular RF superconductivity,” *Superconductor Science and Technology,* vol. 4, no. 6, 1991.

[63] A. Gurevich and G. Ciovati, “Effect of vortex hotspots on the radio-frequency surface resistance of superconductors,” *Physical Review B,* vol. 87, no. 054502, 2013.

[64] V. Palmieri and R. Vaglio, “Thermal contact resistance at the Nb/Cu interface as a limiting factor for sputtered thin film RF superconducting cavities,” *Supercond. Sci. Technol.,* vol. 29, no. 015004, 2016.

[65] J. Halbritter, “RF residual losses, high electric and magnetic rf fields in superconducting cavities,” in *38th Eloisatron Project Workshop*, Erice, Italy, 1999.

[66] R. W. Smith and D. J. Srolovitz, “Void formation during film growth: A molecular dynamics simulation study,” *J. Appl. Phys,* vol. 79, no. 3, pp. 1448-1457, 1996.

[67] V. Nemkov and V. Demidovich, Theory of Induction heating, St. Petersburg, Russia: Energoatomizdat, 1988.

[68] V. Rudnev and et al., Handbook of Induction Heating, New York: Marcek Dekker, 2003.

[69] A. C. Metaxas, Foundation and Electroheat: A Unified Approach, New York, USA: John Willey and sons, 1996.

[70] C. R. Brooks, Principles of the Heat Treatment of Plain Carbon and Low Alloy SteelsC., Almere, Netherlands: ASM International, 1996.

[71] L. Maissel and R. Glang, Handbook of Thin Film Technology, New York, USA: McGraw-Hill, 1970.

[72] R. Behrisch and K. Wittmaack, Sputtering by Particle Bombardment III, Berlin, Germany: Springer-Verlag , 1991.

[73] R. Behrish, Sputtering by Particle Bombardment II, Berlin, Germany: Springer-Verlag, 1983.

[74] J. L. Vossen, Thin Film Processes, Academic Press, 1978.

[75] S. M. Rossnagel and et al., Handbook of plasma processing technology, Noyes publications, 1990, p. 483.

[76] B. A. Movchan and A. V. Demchishin, “Structure and Properties Of Thick Condensates Of Nickel, Titanium, Tungsten, Aluminum Oxides, And Zirconium Dioxide In Vacuum,” *Fiz. Metal. Metalloved.,* vol. 28, p. 653, 1969.

[77] E. Kay and G. Heim, “Model of bias sputtering applied to the control of Nb film properties,” *Journal of Applied Physics,* vol. 49, no. 9, p. 4862, 1978.

[78] Bruker, “Dektak 8 Surface Profiler - Decktak 8 user manual,” 2014. [Online]. Available: http://www.tstvn.com/en/nanotechnology-a-semiconductor/metrology-tools/opticalprofiler/bruker/bruker-.html. [Accessed 12 12 2016].

[79] W. Singer, "RRR-Measurement Techniques on High Purity Niobium," 02 2010. [Online]. Available: https://bib-pubdb1.desy.de/record/91801/files/TTC-Report%202010-02.pdf. [Accessed 21 01 1017].

[80] G. Lanza, *New Magnetron Configurations For Sputtering Niobium Thin Films,* Padua, Italy: PHD thesis University of Padua, 2008.

[81] D. Tonini, C. Greggio, G. Keppel, M. Musian, G. Torzo and V. Palmieri, "Morphology of niobium films sputtered at different target – substrate angle," in *Proceeding of the 11th Workshop on RF superconductivity*, Lubeck, Germany, 2003.

[82] N. Aschroft, Solid State Physics, Harcourt College Publishers, 1976.

[83] D. Franco, *An innovative cylindrical magnetron sputtering source for the deposition of hie-isolde superconducting Nb/Cu QWRs,* Ferrara: PHD Thesis, University of Ferrara, 2015.

[84] V. Palmieri, G. Keppel and D. Franco, "System for magnetron sputtering deposition of a film of a base material on the interior surface of a substrate". Patent WO2016135693 A1, 01 09 2016.